TECHNICAL REPORT STANDARD PAGE

1. Report No.	2. Government Accession No.	3. Recipient's Catalog No.
FHWA/LA.14/526		

4. Title and Subtitle	5. Report Date
Data Collection and Evaluation of Continuity Detail for John James Audubon Bridge No. 61390613004101	October 2014
	6. Performing Organization Code
7. Author(s)	8. Performing Organization Report No.
Ayman M. Okeil, Ph.D., P.E.	
9. Performing Organization Name and Address	10. Work Unit No.
Department of Civil and Environmental Engineering Louisiana State University Baton Rouge, LA 70803	11. Contract or Grant No. LTRC Project Number: 12-1ST SIO Number: 30000546
12. Sponsoring Agency Name and Address	13. Type of Report and Period Covered
Louisiana Department of Transportation and Development P.O. Box 94245 Baton Rouge, LA 70804-9245	Final Report January 2012 – December 2013
	14. Sponsoring Agency Code

15. Supplementary Notes

Conducted in Cooperation with the U.S. Department of Transportation, Federal Highway Administration

16. Abstract

This report summarizes findings from monitoring data that was collected over a two-year period from Bridge No. 61390613004101 in the John James Audubon Project, which was formerly designated as Bridge #2 prior to construction completion. The bridge was instrumented as part of an earlier project (LTRC Project No. 08-1ST). Results from the first monitoring project warranted resuming data collection to monitor the performance of Bridge No. 61390613004101 over a longer period of time. The focus of the monitoring effort for both projects is on the employed continuity detail, which is based on the recommendation of the National Cooperative Highway Research Program (NCHRP) Final Report 519. Continuity details are typically used to eliminate the needs for high-maintenance joints that often lead to the acceleration of element deterioration near the joints. The employed positive moment continuity detail transfers forces between adjacent girders via positive moment reinforcement that extends out of the bottom flanges of the prestressed concrete (PSC) girders into a continuity diaphragm.

The 96-channel monitoring system that was installed as part of Project 08-1ST was reactivated in February 2012. Data from the embedded and surface-mounted sensors that measure strains, temperatures, rotations, and gap openings in critical locations in the monitored segment were collected for a period of two years. The collected data from both projects (12-1ST and 08-1ST) was analyzed and interpreted. Furthermore, four field visits were conducted to document the condition of the girder ends in the monitored segment.

Recommendations based on the project findings are drawn. Data shows that 5 years after the construction of the bridge, some long-term effects such as creep and shrinkage have diminished. It is also evident that temperature effects are still a major factor that continues to strain the bridge in such a way that should not be ignored in the design of bridges with similar continuity details. The high-localized strains at girder ends due to thermal variation caused cracking in a few girder ends.

17. Key Words	18. Distribution Statement
prestressed concrete; creep; continuous structures; bridges, live load	Unrestricted

19. Security Classification (of this report)	20. Security Classification (of this page)	21. No. of Pages	22. Price
N/A	N/A	104	N/A

Project Review Committee

Each research project will have an advisory committee appointed by the LTRC Director. The Project Review Committee is responsible for assisting the LTRC Administrator or Manager in the development of acceptable research problem statements, requests for proposals, review of research proposals, oversight of approved research projects, and implementation of findings.

LTRC appreciates the dedication of the following Project Review Committee Members in guiding this research study to fruition.

LTRC Manager

Walid Alaywan, PhD, P.E.
Senior Structures Research Engineer

Members

Paul Fossier, P.E.
David Miller, P.E.
Mike Boudreaux, P.E.
Arturo Aguirre, P.E.

Directorate Implementation Sponsor

Richard D. Savoie
DOTD Chief Engineer

Data Collection and Evaluation of Continuity Detail for John James Audubon Bridge No. 61390613004101

by

Ayman M. Okeil, Ph.D., P.E.
Associate Professor

Department of Civil and Environmental Engineering
3513-D Patrick F. Taylor Hall
Louisiana State University
Baton Rouge, LA 70803

LTRC Project No. 12-1ST
SIO No. 30000546

conducted for

Louisiana Department of Transportation and Development
Louisiana Transportation Research Center

October 2014

ABSTRACT

This report summarizes findings from monitoring data that was collected over a two-year period from Bridge No. 61390613004101 in the John James Audubon Project, which was formerly designated as Bridge #2 prior to construction completion. The bridge was instrumented as part of an earlier project (LTRC Project No.: 08-1ST). Results from the first monitoring project warranted resuming data collection to monitor the performance of Bridge No. 61390613004101 over a longer period of time. The focus of the monitoring effort for both projects is on the employed continuity detail, which is based on the recommendation of the National Cooperative Highway Research Program (NCHRP) Final Report 519. Continuity details are typically used to eliminate the need for high-maintenance joints that often lead to the acceleration of element deterioration near the joints. The employed positive moment continuity detail transfers forces between adjacent girders via positive moment reinforcement that extends out of the bottom flanges of the prestressed concrete (PSC) girders into a continuity diaphragm.

The 96-channel monitoring system that was installed as part of Project 08-1ST was reactivated in February 2012. Data from the embedded and surface-mounted sensors that measure strains, temperatures, rotations, and gap openings in critical locations in the monitored segment were collected for a period of two years. The collected data from both projects (12-1ST and 08-1ST) was analyzed and interpreted. Furthermore, four field visits were conducted to document the condition of the girder ends in the monitored segment.

Recommendations based on the project show that 5 years after the construction of the bridge, some long-term effects such as creep and shrinkage have diminished. It is also evident that temperature effects are still a major factor that continues to strain the bridge in such a way that should not be ignored in the design of bridges with similar continuity details. The high-localized strains at girder ends due to thermal variation caused cracking in a few girder ends.

ACKNOWLEDGMENTS

The author gratefully acknowledges the financial support provided by the Louisiana Transportation Research Center (LTRC) (LTRC Project No. 12-1ST) and the Louisiana Department of Transportation and Development (DOTD) (SIO No.3000546).

The author also acknowledges the assistance of Sushovan Ghimire, a graduate student in the Department of Civil and Environmental Engineering, for assistance in developing the plots of sensor records.

The authors would also like to thank Paul Fossier (DOTD) for initiating the idea behind this project and for providing information pertinent to the project throughout its execution. The support from DOTD's Structures and Facilities Maintenance Administration with field inspections is greatly appreciated.

Finally, special thanks are due to Dr. Walid Alaywan (LTRC), senior structures research engineer, for his support of this research.

IMPLEMENTATION STATEMENT

This study confirms the findings from LTRC Project 08-1ST. DOTD stands to directly benefit from this project by helping establish general policies for the design of multispan prestressed concrete girder bridges as follows:

1. The DOTD Bridge Design and Evaluation Manual, which is currently under development, should not adopt the NCHRP Final Report 519 positive moment continuity detail as one of the recommended details for employment in Louisiana bridges. Simpler details should be developed for inclusion in the manual. The new continuity details should be developed to achieve construction acceleration and lower potential for damage caused by leaks through expansion joints, while eliminating high positive restraint moments.
2. In cases where the NCHRP Final Report 519 positive moment continuity detail is adopted (e.g., Design-Build projects), it is prudent that the effect of thermal variations on bridges employing this detail be considered. Thermal effects should be superimposed on other long-term effects such as creep and shrinkage considering the construction sequence, i.e., girder age at time of continuity establishment.
3. The cracks that developed at girder ends in the monitored segment of Bridge No. 61390613004101 seem to have stabilized as no new cracks were observed during the last two visits. Regular inspections at the typical two-year interval can take place to search any new cracks and to monitor existing crack that have been documented in this report.

TABLE OF CONTENTS

LIST OF TABLES

LIST OF FIGURES

INTRODUCTION

In 2008, the Louisiana Transportation Research Center (LTRC) sponsored a research project to monitor a newly constructed bridge employing a positive moment continuity detail that is different from the continuity detail adopted in the Louisiana DOTD Bridge Design Manual [*1*]. The monitored segment is part of Bridge No. 61390613004101 from the John James Audubon Project that was contracted as a design-build project, which allowed the designer more freedom to choose the new detail. The DOTD Bridge Design section seized the opportunity and initiated the idea to monitor the new detail in one segment, which was chosen to be a skewed segment, built using bulb-T girders. Skewed layouts and bulb-T girders were not part of the scope of National Cooperative Highway Research Program (NCHRP) Final Report 519 that recommended the new continuity detail [*2*].

Figure 1(a) shows the adopted detail, which relies on additional hairpin bars that extend outside of bottom flanges at girder ends into a cast-in-place (CIP) diaphragm where continuity is to be established. As the name indicates, the purpose of the positive moment reinforcement, i.e., hairpin bars, is to resist positive moments that develop in continuous bridge structures due to long-term effects such as creep and thermal gradients. Such effects cause the continuous structure to camber up as can be seen in

Figure 2, which causes bottom flanges at girder ends to move away from each other if unrestrained as is the case for the continuity detail adopted in the Bridge Design Manual [see Figure 1(b)]. The positive moment reinforcement resists this movement by developing tension forces due to their extension.

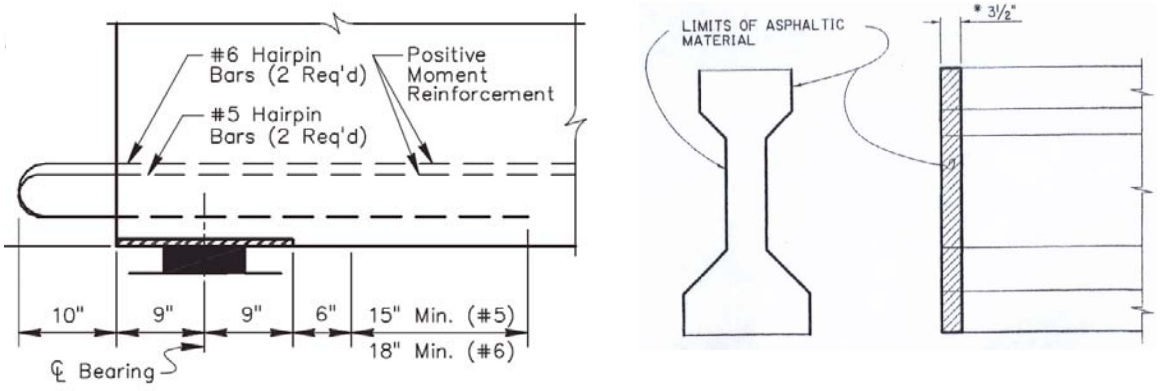

(a) NCHRP 519 detail (hairpin option) [*2*] **(b) Louisiana BDM detail**

Figure 1
Continuity detail for precast PSC girder bridges

Negative moments also develop over continuous supports and are larger than positive moments. However, the structural system and reinforcement details are such that it can be easily resisted by the abundance of tensile reinforcement in the deck and the ability of bottom flanges of precast prestressed concrete (PSC) girders to transfer compression forces from one span to another through the diaphragm. Many researchers have investigated the design, analysis, and behavior of continuous girder bridge construction. There are advantages and disadvantages for establishing full continuity (full integration), establishing partial continuity, or simply having no continuity at all, i.e., multi-simple span construction. A thorough review of continuity in bridge construction can be found in the final report of LTRC Project 08-1ST *[3]*.

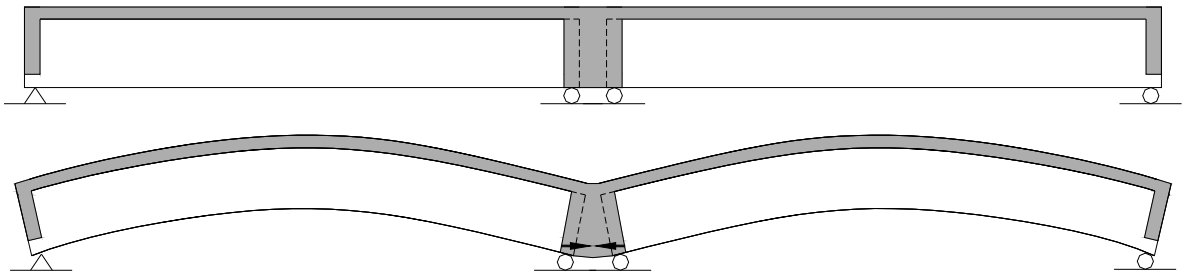

Figure 2
Development of positive moment in bridge connections with continuity diaphragm

Summary of Project LTRC 08-1ST Findings

Project LTRC 08-1ST was completed in December 2010 after more than two years of monitoring. Based on analyses of monitoring data, which was complemented by analytical and numerical models, a final report was published in June 2011 (*LTRC Final Report No. 477 [3]*). For the monitored segment of Bridge No. 61390613004101, two of the main conclusions were as follows:

1. The positive moment continuity detail has the ability to transfer forces from one girder end to the adjacent girder end across the continuity diaphragm. The tension forces in hairpin bars are caused by long-term and live load effects, however, the dominant effects were seasonal and daily temperature variations, especially temperature gradients. The level of restraint moment due to the combined seasonal and daily temperature changes is probably the most important factor in the design of this detail, since the designer has no influence over the temperatures at the bridge site. The other positive-moment causing factor, i.e., girder creep caused by prestressing forces, can be greatly reduced by not introducing continuity until a large portion of

the creep takes place prior to pouring the diaphragm.

2. Positive restraint moment can cause cracking in the diaphragm and/or girder ends. Both types of cracking affect the performance of the diaphragm and the bridge. More importantly, girder cracking may have adverse effects on the durability and on the shear capacity of the girders. Therefore, special care should be given to the level of positive restraint moment during design.

The main crack that was observed in Girder G3 can be seen in Figure 3. It was first observed during a site visit in May 2009. At that time, the crack could only be seen extending from the top of the bottom flange to its mid-height [see Figure 3(a)]. During another visit in October 2010, it was clear that the crack propagated and could be seen extending all the way to the soffit of the girder [see Figure 3(b)]. Other than this girder (G3), no other cracks were observed in the remaining girders except for a small crack at the other end of Girder G3 in Span 24 at Bent 25. The growth of the crack was attributed to additional creep deformation, which caused additional positive moments that lead to an increase in tension forces in the hairpin bars. Positive moments that develop due to the combined effects of creep and thermal gradient can cause tensile stresses at girder ends in excess of the tensile strength of concrete, hence the observed cracking. While no cracking was observed in other girders, it was hypothesized that there is a potential for cracking of other girders with time as more creep deformation takes place in addition to the inevitable thermal gradient effects, the most dominant cause of positive moment in the monitored segment.

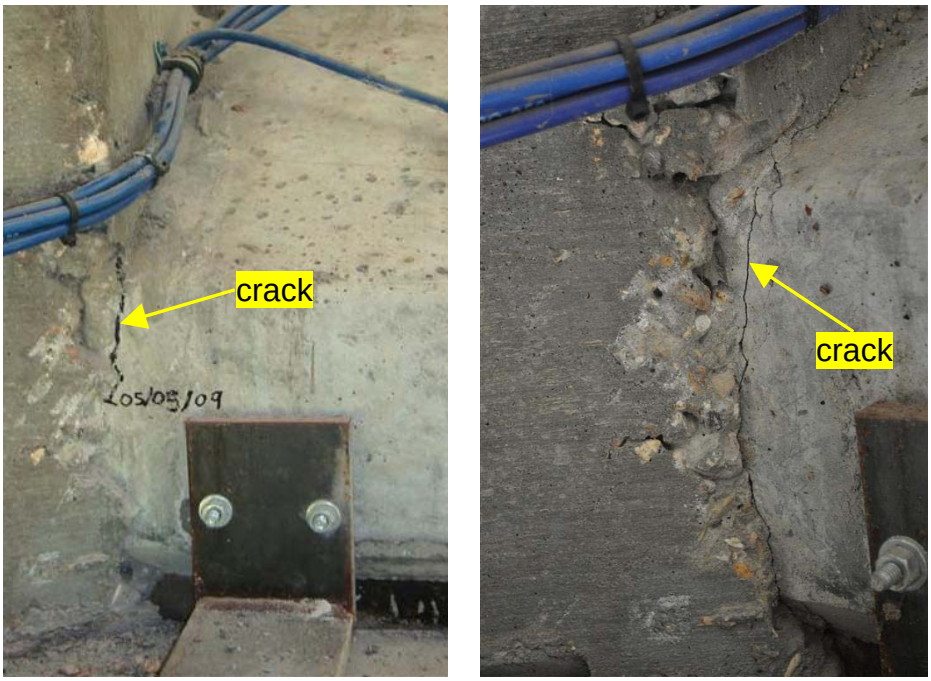

(a) May 5, 2009 **(b) October 22, 2010**

Figure 3
Observed crack at bottom flange of Girder G3 – Span 24 – Bent 24

Research Needs

After the completion of Project 08-1ST, it was concluded that additional monitoring was needed, especially in light of the girder end cracking observed in Girder G3. The additional monitoring would rely on the same monitoring system installed as part of Project 08-1ST. The additional data would be used for the purpose of further evaluating the performance of the positive moment detail that is employed in Bridge No. 61390613004101 of the James Audubon bridge project under long-term effects. Furthermore, repair work that took place to one of the girders in the monitored segment should be assessed and documented.

OBJECTIVE

The main objective of this project was to continue data collection from a monitoring system that was installed as part of Project LTRC 08-1ST for the purpose of further investigating the performance of a continuity diaphragm detail that is newly introduced in Louisiana and employed in Bridge No. 61390613004101 of the James Audubon Bridge Project.

The goals of the project were to:

1. Collect, analyze, and interpret field monitoring data to further understand the behavior of Bridge No. 61390613004101 under long-term and complement findings from original project.
2. Conduct periodic site visits to perform visual inspections of monitored segment with special emphasis on monitoring girder crack development.
3. Provide DOTD with recommendations to assist in the development of the new Bridge Design and Evaluation Manual and planning of future inspections of Bridge No. 61390613004101.

SCOPE

This study is focused on one bridge segment that was instrumented as part of Project 08-1ST. The instrumentation plan was designed to provide information about the performance of the positive moment continuity detail in a skewed bridge segment that covers Spans 23, 24, and 25 and is part of Bridge No. 61390613004101 of the John James Audubon Project. The monitored segment characteristics and the installed monitoring system, therefore, limit the scope of the project. The main focus of the project activities were similar to those of LTRC Project 08-1ST, which was to monitor long-term (creep, shrinkage, and thermal) effects on the continuity detail. The effects of live loads on the detail were not investigated for this project as they were in LTRC Project 08-1ST.

The results from this investigation were thoroughly documented to serve as a reference point for future projects that monitor similar and other continuity details.

METHODOLOGY

The performance of the new positive moment continuity detail was evaluated for long-term effects via Structural Health Monitoring (SHM) of a bridge in service that employs the detail from the beginning of construction. The following sections describe the main features of the SHM system, which was installed as part of LTRC Project 08-1ST. The reader is referred to the final report from this project for more details [*3*]. Visual inspections and implementation of an analytical model for the analysis of thermally induced stresses is also described in this section.

Structural Health Monitoring

A structural health-monitoring plan was devised for the bridge chosen by DOTD to conduct the assessment study. This section describes the details of the monitored bridge, instrumentation plan, data processing, and interpretation.

Description of Monitored Bridge

Bridge No. 61390613004101 is one of eight bridges in the John James Audubon Project that carries Louisiana Highway 10 (LA 10) across the Mississippi River between West Feliciana and Pointe Coupe parishes [see Figure 4(a)]. The purpose of Bridge No. 61390613004101 is to cross an existing railway track, which can be seen in Figure 4(b). Bridge No. 61390613004101 consists of 52 spans with a total length of about 4000 ft. divided into 14 continuous segments. The monitored segment is a 242-ft. three-span continuous superstructure with a skewed layout. The girder span lengths for the monitored segment ranged from 51 ft. to 89 ft. for the exterior spans due to the skewed layout, while the middle span was 102 ft. long. Figure 5(a) shows the main layout and dimensions of the monitored segment, which was constructed using AASHTO Bulb–T girders (BT-72). Only one of the identical (due to antisymmetry) intermediate bents (Bent 24 and Bent 25) was chosen for the investigation. This segment was chosen by DOTD for monitoring because of its configuration, which has not been covered by the tests conducted in NCHRP Final Report 519, namely skewed configuration and Bulb-T girders.

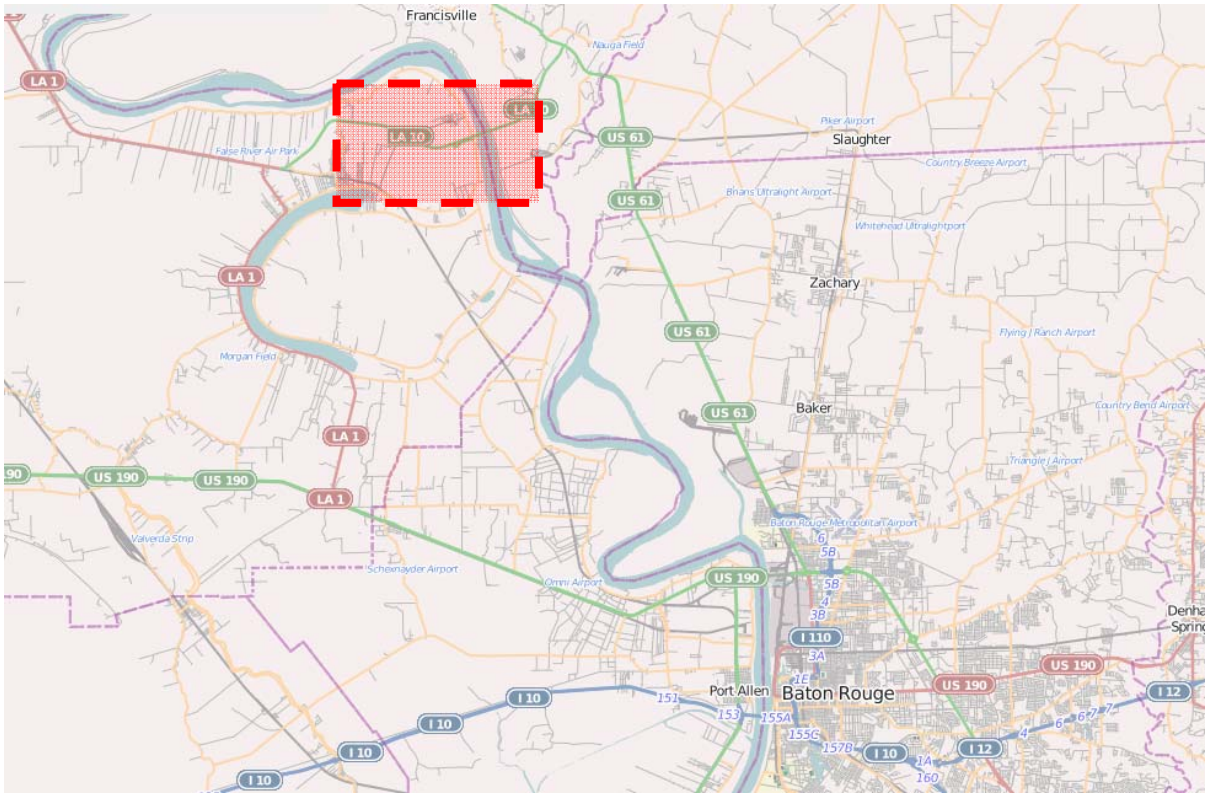

(a) General location (see box details below)

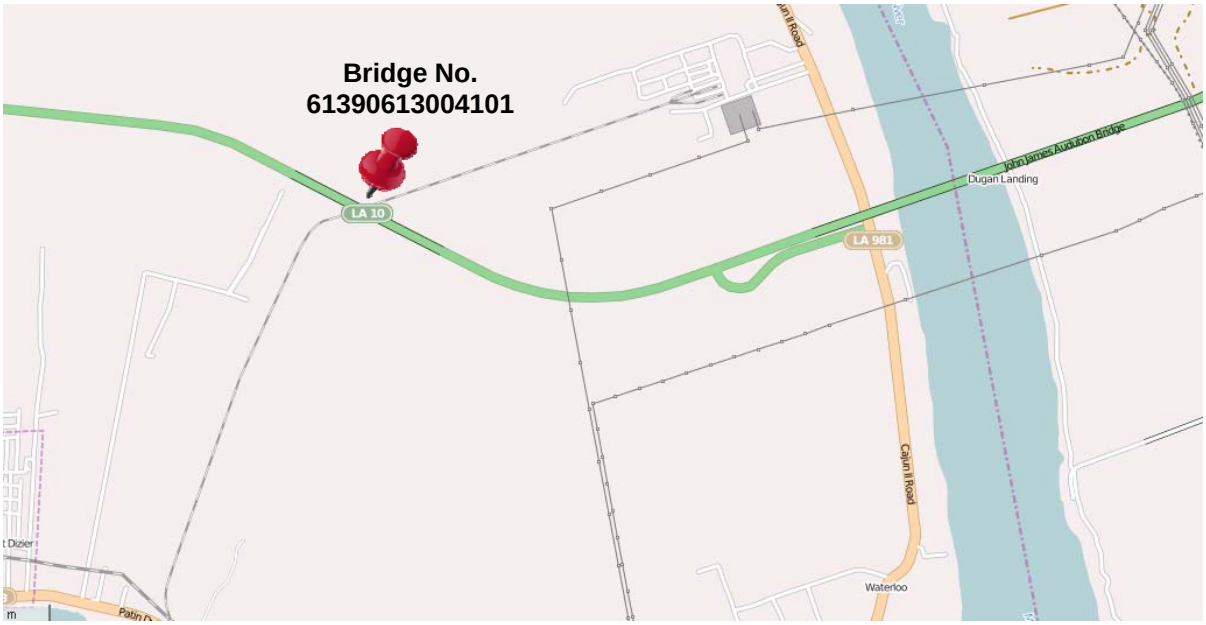

(b) Bridge site surroundings

Figure 4
Location of Bridge No. 61390613004101

Figure 5(b) shows a cross section of the monitored bridge segment, which includes two 11-ft. lanes in addition to two 8-ft. shoulders forming a clear roadway width of 38 ft. on five prestressed BT-72 girders spaced at 8.25 ft. The 7.5-in. reinforced concrete deck was monolithically cast with the continuity diaphragm joining adjacent girders over intermediate bents. Hairpin bars were embedded in the girders and extended 8 in. outside the girder ends to provide positive reinforcement. It should be noted that the girders are supported by neoprene bearing pads over typical pile bents.

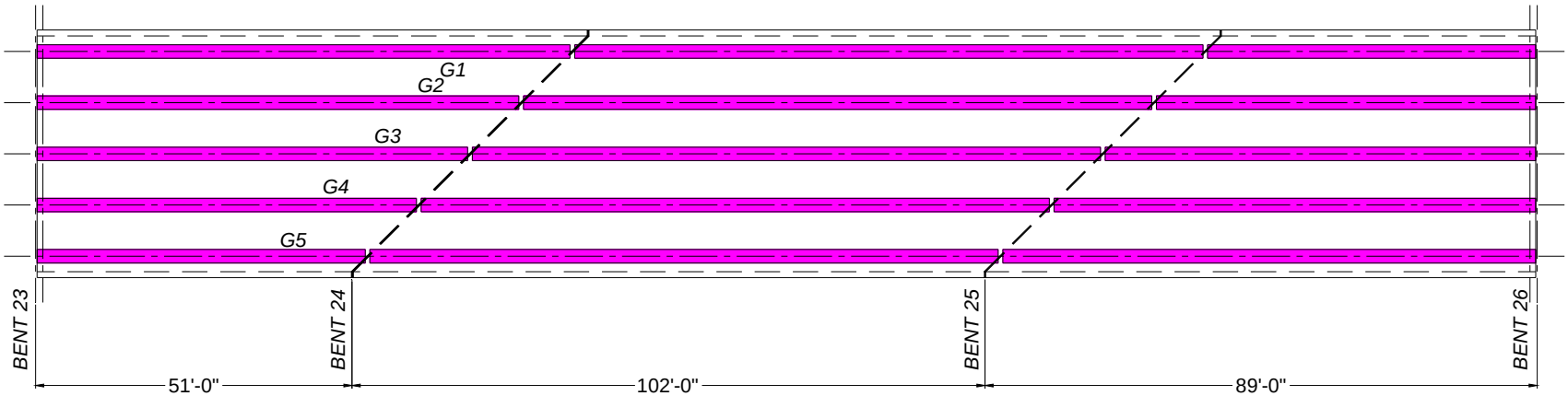

(a) Bridge layout

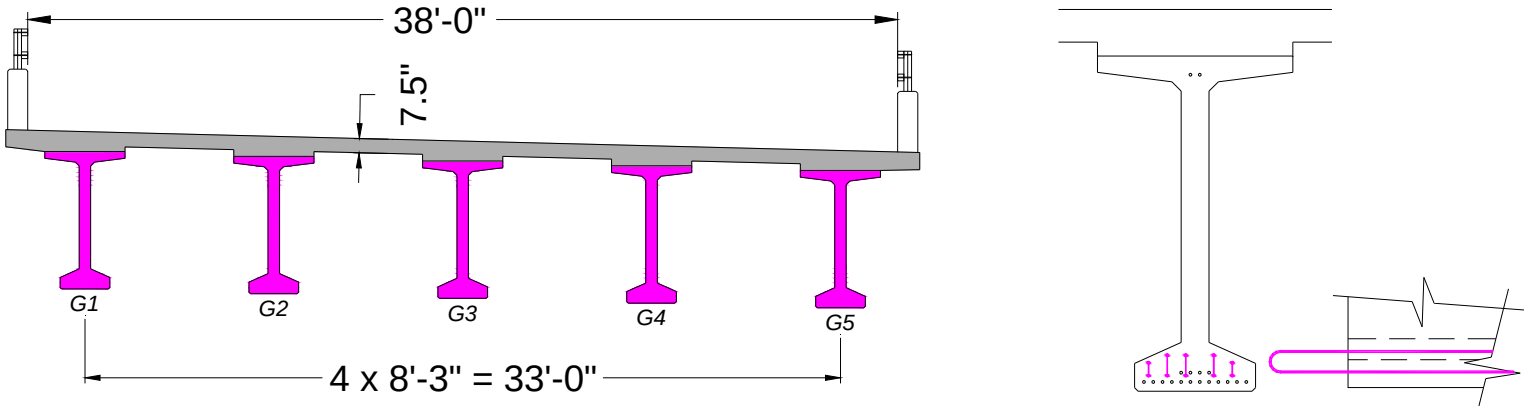

(b) Cross section and continuity detail (5#5 hairpin bars)

Figure 5
Main dimensions of monitored Bridge No. 61390613004101

Material Properties and Fabrication Details

Materials used in the construction of the PSC girders and reinforced concrete deck were tested and documented in the final report for LTRC Project 08-1ST [*3*]. The testing conducted to document material properties included concrete compressive strength after 28 days according to ASTM C 39, and modulus of elasticity, E_c, according to ASTM C 469 [*4, 5*]. The tensile strength of concrete was estimated using modulus of rupture tests according to ASTM C 78 for the girders and the splitting tensile strength test according to ASTM C469 for the reinforced concrete deck [*6, 7*]. It should be noted here that the tests revealed that the material properties of the as built structure exceeded the specified design compressive strength for the Bulb-T girders and bridge deck concretes.

The stress strain relationship for the prestressing strands was also documented in LTRC Project 08-1ST [*3*].

Instrumentation Plan

The monitoring system was designed to capture: (1) the tensile force in the positive moment reinforcement, (2) the strain distribution at key locations (intermediate bent and midspan), (3) differential shrinkage between cast-in-place (CIP) deck and precast girders, (4) the degree of continuity between adjacent girders, (5) the development of gaps at the continuity diaphragm, and (6) the corresponding temperature for each of the recorded readings. The sensor locations were selected to be at the most critical locations that deliver the information required to assess the performance of the continuity detail.

All of the selected gages are based on the vibrating wire technology, which is known to be well suited for long-term monitoring as they do not suffer from drifting with age [*8, 9*]. Table 1 lists the type and number of each of the employed sensors. A total of 66 embedded and external (surface mounted) sensors were used in the system, which has a logging capacity of 96 channels. As stated earlier, antisymmetry of the bridge segment layout was taken advantage of, allowing for only one bent to be monitored. Three positive moment continuity details were fully instrumented (connecting Griders G1, G3, and G5) at the support. Embedded sensors were installed in the deck over the support at the remaining two girders. At midspan, three girders (Girders G3, G4, and G5) were fully instrumented. Along the midspan line, Girder G1 is identical to Girder G5 and Girder G2 is identical to Girder G4. Therefore, information across the the midspan section is attainable.

Figure 6 shows the final instrumentation plan where the monitored girders, sensor types, locations, and numbers can be seen.

Table 1
Types and number of sensors employed in this study

Sensor Type	Measurement	Location	Number
Sisterbars (VW4911)	Strain in concrete	Embedded	12
Strandmeters (VW4410)	Strain in reinforcement		16
Strain gages (VW4000)	Surface strains	Surface Mounted	29
Gapmeters (VW4420)	Gap width		3
Tiltmeter (VW6350)	Slope		6
Crackmeter*	Crack width		7
		Total:**	**66**

*Crackmeters were not installed due to lack of significant cracking.

**Excluding uninstalled crackmeters

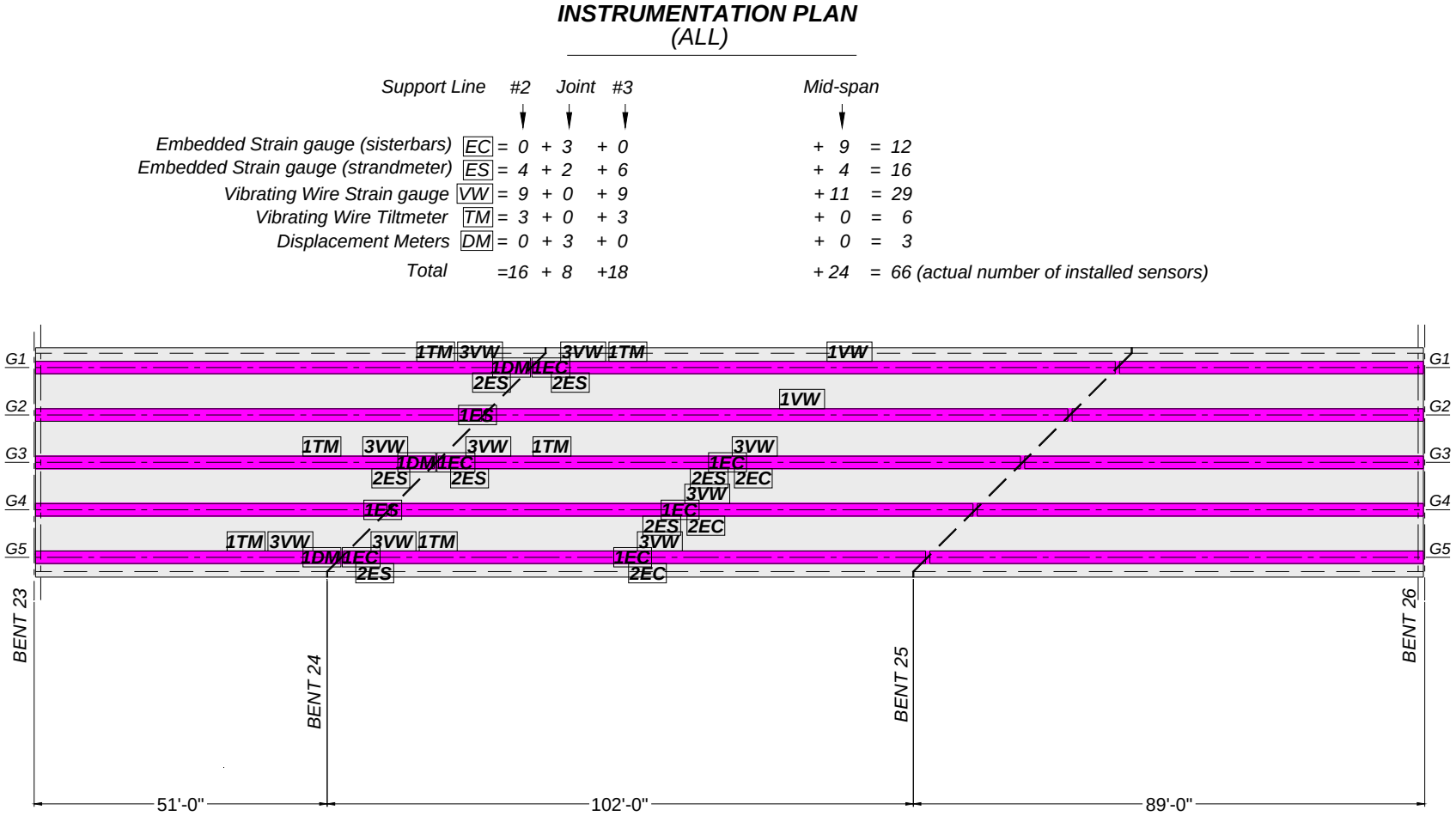

Figure 6
Instrumentation Plan for structural health monitoring of positive moment continuity detail in Bridge No. 61390613004101

Details about the sensor locations at each monitored section can be found in the final report of Project 08-1ST [*3*]. For easier readability, they are also summarized in Appendix A of this report. They were grouped into six multiplexers that were connected to a DC battery-powered Campbell Scientific datalogger, which was recharged by a solar panel. Recorded data was retrieved remotely via cellular modem through an internet (IP – Internet Protocol) connection.

Data Processing

Raw data obtained directly from the logger had to be first processed before it could be interpreted. Three steps of data proceses were conducted before they could be interpreted: (1) Cleaning the record from any outliers, (2) joining or disjoining records in case data channel was changed during the monitoring period, and (3) temperature correction as specified by the sensor manufacturer.

The final report for LTRC Project 08-1ST has more details about each of these steps *[3]*.

Visual Inspections

In addition to data collection and interpretation, four visits to the bridge site took place to visually inspect the monitored bridge segment. With the help of DOTD Bridge Maintenance crews, a snooper truck was used to reach underneath the bridge and observe any changes to girder ends. The visits were scheduled to take place during different weather seasons to study the effect of thermal variations on the positive moment continuity detail. The visits took place on:

- February 24, 2012 (Cold/Mild Winter Weather)
- August 6, 2012 (Hot Summer Weather)
- March 13, 2013 (Mild Winter Weather)
- August 22, 2013 (Hot Summer Weather)

During the site visits, it was also possible to document the performance of two repairs to girder ends, which were triggered by the crack observed in Girder G3 (see Figure 3).

Implementation of Thermal Gradient Analysis in mRestraint

mRestraint is a modified version of the program developed as part of NCHRP Final Report 519 [*2*]. The initial modification of the original Restraint program was part of LTRC Project 08-1ST efforts for the purpose of eliminating many of the limitations inherent in the original version. As was revealed by the findings of LTRC Project 08-1ST, thermal effects are as important, if not more important, than other long-term effects such as creep. Therefore, it was deemed appropriate to incorporate a module for thermal analysis in mRestraint to allow designers to have one tool that is capable of performing both analyses. The theoretical background for this part of the effort is summarized next.

There are two types of thermally induced stresses: primary thermal stresses and secondary thermal stresses. Primary thermal stresses develop due to the nonlinear distribution of temperature across the height of structure whereas the secondary thermal stresses develop in statically indeterminate structures as a result of the compatibility to maintain the boundary conditions. The sum of these two stresses results in the total stress induced by temperature. Priestly presented an analysis method for estimating the thermal stresses induced by a temperature gradient [*10*]. These equations are based on fundamental mechanics principles in addition to some assumptions such as, material properties are independent of temperature, materials are homogenous and isotropic, plane section remains plane after thermal loading and temperature profile can be defined throughout the intended structure.

Primary Thermal Stresses

The primary thermal stress is calculated based on the assumption that plane sections remain plane. This assumption leads to the following equation:

$$f_{p(y)} = E_c\left(\varepsilon_y - \alpha_c\theta_{(y)}\right) \quad (1)$$

where, E_c is the modulus of elasticity of concrete, ε_y is the linear strain distribution, α_c is the coefficient of thermal expansion of concrete, and $\theta_{(y)}$ is the change in temperature. Integrating Equation 1 over the section depth d results in the internal axial force. The equation can also be used to calculate the corresponding internal bending moment due to the primary thermal stresses. For primary thermal stress calculations, the structure is assumed to be determinate by removing sufficient redundancies. As a result, the internal axial force and bending moment cannot develop and assumed as zero. This leads to the following equations:

$$P = E_c \int\left(\varepsilon_y - \alpha_c\theta_{(y)}\right) b_y dy = 0 \quad (2)$$

$$M = E_c \int\left(\varepsilon_y - \alpha_c\theta_{(y)}\right) b_y (y-n) dy = 0 \quad (3)$$

where, b_y is the net section width at height y, n is the distance between the neutral axis and any arbitrary datum, and y is the height at which net section width is taken. The equation for the assumed linear strain distribution can be written as:

$$\varepsilon_y = \varepsilon_0 + \psi y \tag{4}$$

where, ε_0 the final is strain at $y = 0$ and ψ is the final curvature. The curvature and strain equations can then be calculated by substituting for ε_y into the force and moment equation:

$$\psi = \frac{\alpha_c}{I} \int \theta_y b_y (y - n) dy \tag{5}$$

$$\varepsilon_0 = \frac{\alpha_c}{A} \int \theta_y b_y dy - n\psi \tag{6}$$

where, A and I are the cross section's area and moment of inertia, respectively. Since most cross-sectional geometries will not be amenable for expressing their relations in the form of equations suitable for integration, it is more suitable to express the curvature and strain in summation form as:

$$\psi = \frac{\alpha_c}{I} \sum_{i=1}^{m} \theta_i (y_i - n) dA_i \tag{7}$$

$$\varepsilon_0 = \frac{\alpha_c}{A} \sum_{i=1}^{m} \theta_i dA_i - n\psi \tag{8}$$

where, the section is discretized into m elements, θ_i and y_i are the average temperature change of the i-th fiber element of area dA_i, and centroid located a height y above the datum respectively. Once the strain and curvature is known, the primary thermal stress induced by θ_i is then calculated as:

$$f_{py} = E_c\left(\varepsilon_0 + \psi y - \alpha_c \theta_y\right) \tag{9}$$

Secondary Thermal Stresses

Secondary thermal stresses also develop in continuous bridge structures due to temperature changes. The secondary stresses are calculated using the fixed end moment produced by curvature, ψ. This is done by conducting a statically indeterminate structural analysis where the redundancies in the system are first removed and then the compatibility equations are solved. Figure 7 illustrates two ways for solving the problem. The restraint moment can be either negative or positive depending on the sign of curvature, which depends on whether the temperature gradient is positive or negative. The fixed end moment is calculated from the flexural rigidity of the section, $E_c I$, and the curvature, ψ:

$$M = E_c I \psi \tag{10}$$

The final moment M' is then calculated based using any structural analysis method (e.g., the moment distribution theorem), from which the secondary stress can be calculated:

$$f_{sy} = \frac{M'(y-n)}{I} \tag{11}$$

The total thermal stresses due to the temperature gradient can now be calculated as the summation of primary and secondary stresses as:

$$f_{ty} = E_c\left(\varepsilon_0 + \psi y - \alpha_c \theta_y\right) + \frac{M'(y-n)}{I} \tag{12}$$

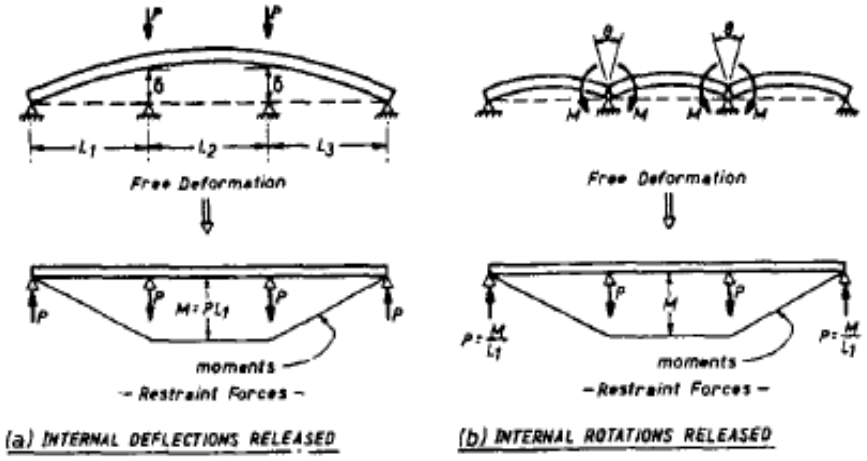

Figure 7
Schematic representation of obtaining restraint moment developed due to temperature gradient

DISCUSSION OF RESULTS

In this section, the results from all approaches described in the Methodology section are presented. The results presented in this report complement the results presented in the final report for LTRC Project 08-1ST and should be viewed in tandem. It should be noted that the results presented herein are the key results that are pertinent to the objectives of this project.

Structural Health Monitoring Data

Temperature Data

Temperature readings were recorded using the built-in thermal sensing capabilities in each vibrating wire sensor. The plots in this section show three temperature plots for each girder at midspan sections of G3, G4, and G5 in Span 24. The first is from a deck sensor, while the other two are girder sensors in the top and bottom flanges.

It can be seen from Figure 8 that the temperature fluctuations from about 20ºF to 115ºF due to seasonal changes are unchanged during the project period as compared to the earlier monitoring period 2008-2010. As expected, deck sensors recorded the highest temperatures as a result of the direct exposure to sunlight. Girder sensors recorded lower temperatures with the top flange temperatures always higher than the bottom flange temperatures. This is true throughout the monitoring period for all girders except for Girder G5 during the winter months, which was attributed to sunlight directly hitting the bottom flange of G5 during the winter months, while the barrier shaded the deck and the overhang shaded the top flange.

As was stated in LTRC Final Report 477, deck surface temperatures are typically higher than temperature from the deck sensors, which is located on the lower mesh of the reinforcement, by about 10-15ºF [*3*].

These temperatures are also used to plot a representative temperature gradient by subtracting the bottom flange temperature readings from the deck temperature readings, which can be seen in Figure 9 for Girder G3. The plot shows that the difference in temperature between the deck sensor and the bottom flange is as high as +18ºF and as low as a –6ºF. It should be reiterated that the deck sensor is installed on the bottom layer of deck reinforcement, which means that the deck surface temperature is even hotter. This means that the actual temperature gradient can easily exceed 25ºF. Such a high temperature gradient can cause the structure to undergo substantial deformations, especially if it is a large structure such as a bridge.

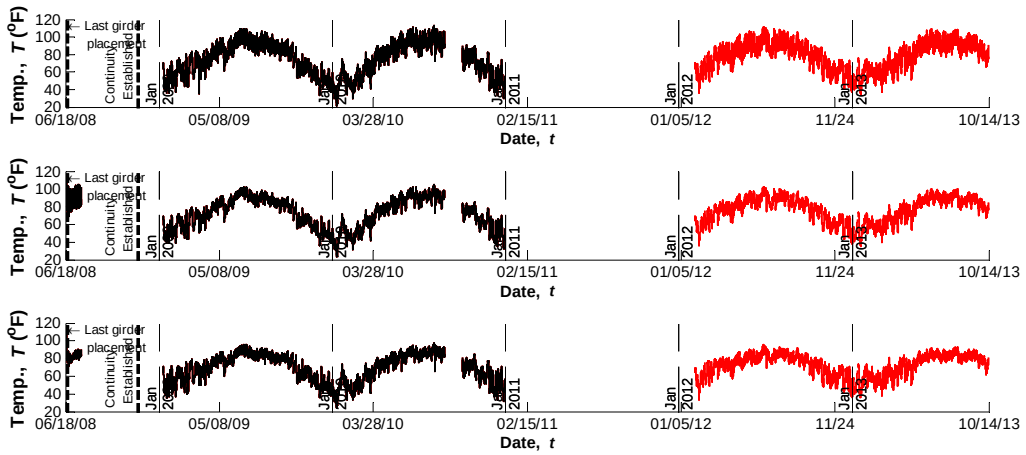

(a) Girder G3

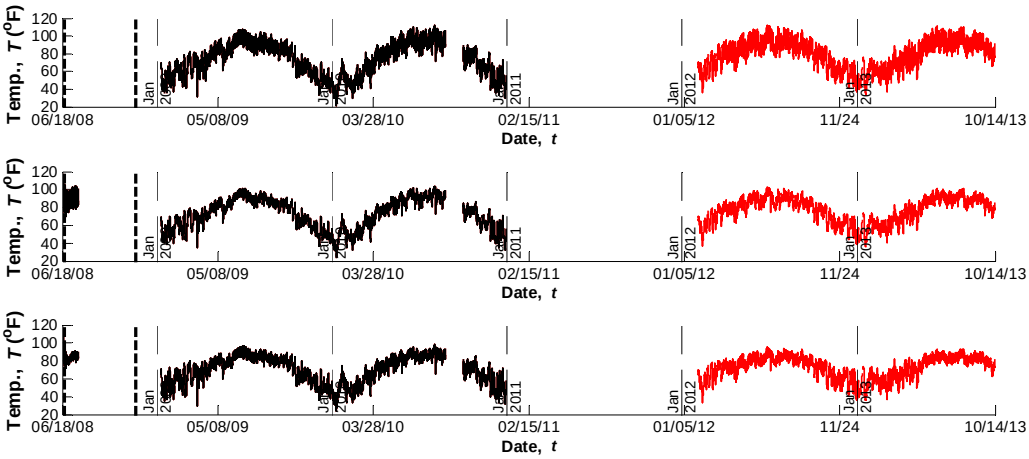

(b) Girder G4

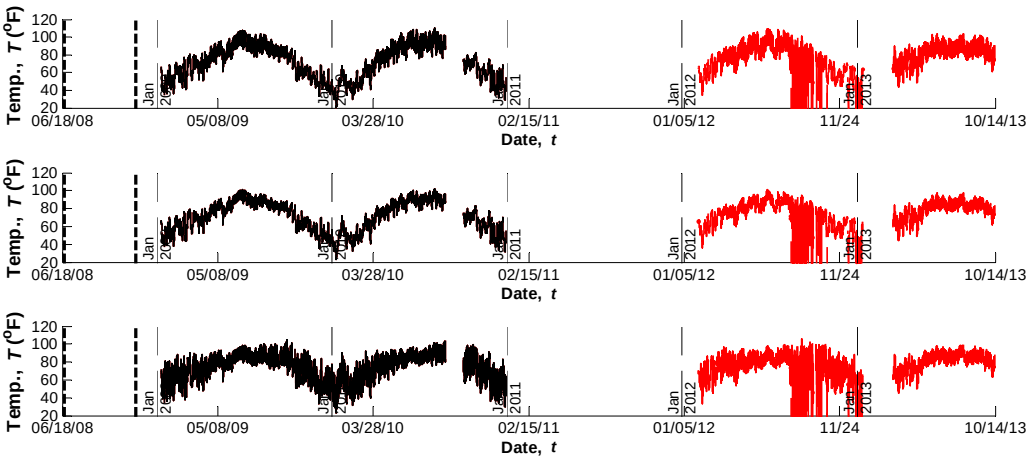

(c) Girder G5

Figure 8
Temperature readings in deck, top, and bottom girder flanges (Span 24)

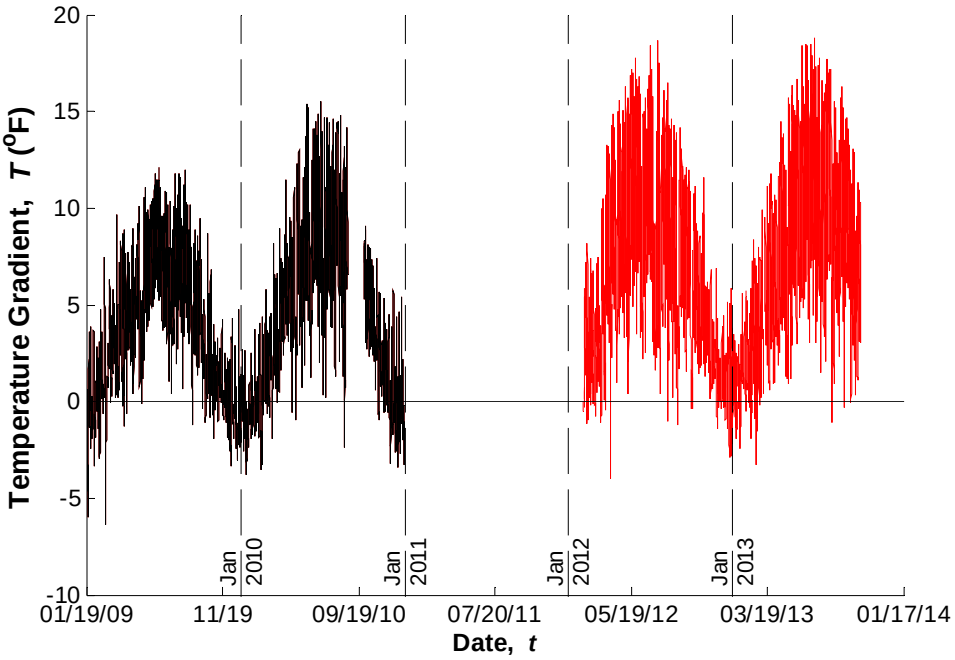

Figure 9
Temperature gradient (Girder G3 in the middle of Span 24)

Strains in Hairpin Bars

High strain readings from sensors on the hairpin bars were the first indicators of potential for cracking in bottom flanges at girder ends. Field inspections that took place during LTRC Project 08-1ST revealed that Girder G3 had cracked at the locations where the high strains were recorded. These cracks, documented earlier (see Figure 3), were part of the motivation behind extending the monitoring of Bridge No. 61390613004101 through the current project. Strains for the same hairpin bars are plotted in Figure 10 for all three monitored joints connecting Span 23 and Span 24 at Girders G1, G3, and G5. As explained in LTRC Final Report 477, no strandmeters were installed on the hairpin bars in Girder G5 in Span 23, hence the missing plot [*3*]. The presented results are the average of readings from two strand meters installed at each monitored location. The top and bottom plot for each girder represent the strain in the hairpin bars installed on the Span 23 side and on the Span 24 side, respectively.

The similarity of the plotted strain records from exterior Girders G1 and G5 is clear. The seasonal change (difference between low temperature in winter and low temperature in summer) in strains remains at 100 microstrains (με), as was noticed in the initial monitoring period. The daily range of fluctuations, however, increased from about 100 $\mu\varepsilon$ to almost

200 $\mu\varepsilon$. This increase alerted the research team to inspect these girders for possible cracking. The results of these inspections are discussed later. As expected, the behavior of Girder G3 was different that the two exterior girders due to the crack discussed earlier (see Figure 3). Higher seasonal and daily fluctuations were recorded in the range of 300 $\mu\varepsilon$ and 900 $\mu\varepsilon$, respectively. The highest recorded strain was almost 1500 $\mu\varepsilon$, which is still below the yield strain for Grade 60 reinforcing bars. The long-term creep effect seems to subside as is clear by comparing the last two seasonal cycles in comparison with the first two seasonal cycles. The increase in strains from July 2009 to July 2010 was about 200 $\mu\varepsilon$. It appears that strains continued to increase during the period in between projects, where no data was collected. After the reactivation of the monitoring system, strains continued to increase as can be seen by comparing readings from July/August 2012 and July/August 2013, however, at a much smaller rate (less than 100 $\mu\varepsilon$) indicating that most of the creep has already taken place. As a result, it can be said that strains higher than those recorded so far are not likely under similar conditions. Furthermore, daily strain fluctuations are the most important factor among long-term effects at this point in the life of the bridge.

Figure 11 shows the strain records from the surface mounted gages on the bottom flanges on Girders G1, G3, and G5 on both sides of the continuity diaphragm, i.e., Span 23 and Span 24. These vibrating wire strain gages were installed 18 in. away from the continuity diaphragm's face. These plots confirm the conclusions from LTRC Project 08-1ST further in the sense that higher hairpin strains are local phenomena due to stress concentrations due to the hairpin detail, which was exacerbated by the crack for Girder G3. At girder ends, the hairpin bars are the sole mechanism for resisting the tensile forces caused by positive restraint moments, hence the stress concentrations, which are quickly distributed among larger areas of the girder away from the diaphragm. According to Saint Venant's principle, at a distance equal to the depth of the member, such local stress concentrations are completely diminished. Also, the effect of prestressing starts showing at this distance, which is almost equal to half the transfer length, in the form of negative strains as opposed to the positive strains at the ends where the hairpin bars sensors were installed. The strain levels are not alarming (less than 200 $\mu\varepsilon$ for G1 and less than 100 $\mu\varepsilon$ for G3 and G5). Finally, Figure 11 also confirms that most of the creep has already taken place, as evidenced by the lack of substantial changes between similar time periods during the last two seasonal cycles.

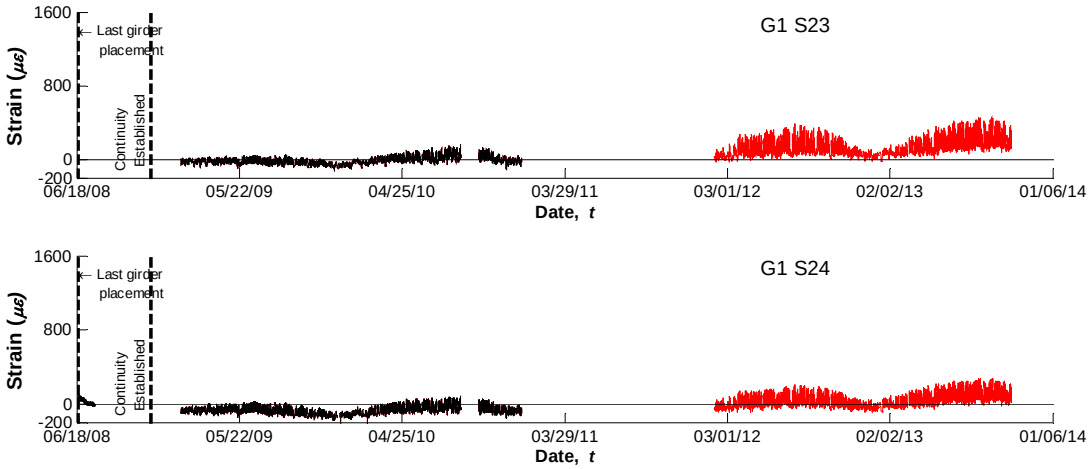

(a) Girder G1

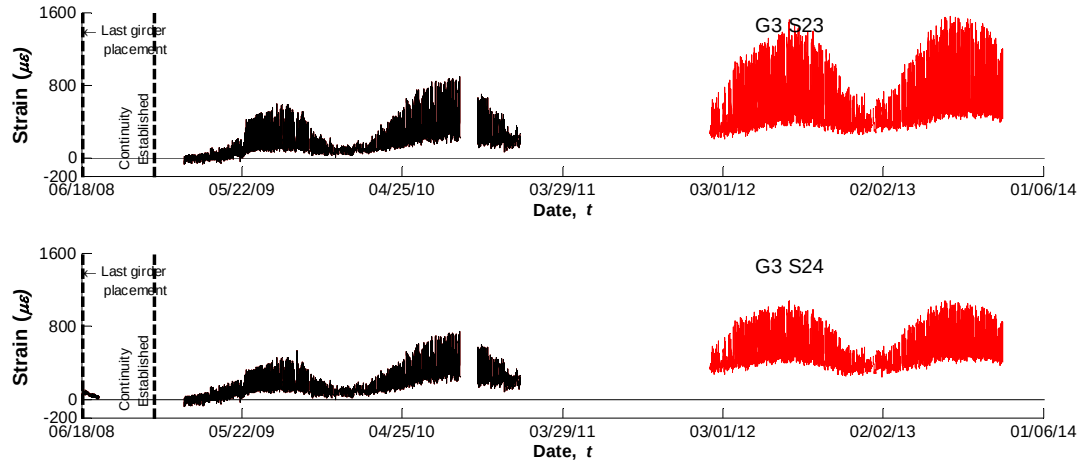

(b) Girder G3

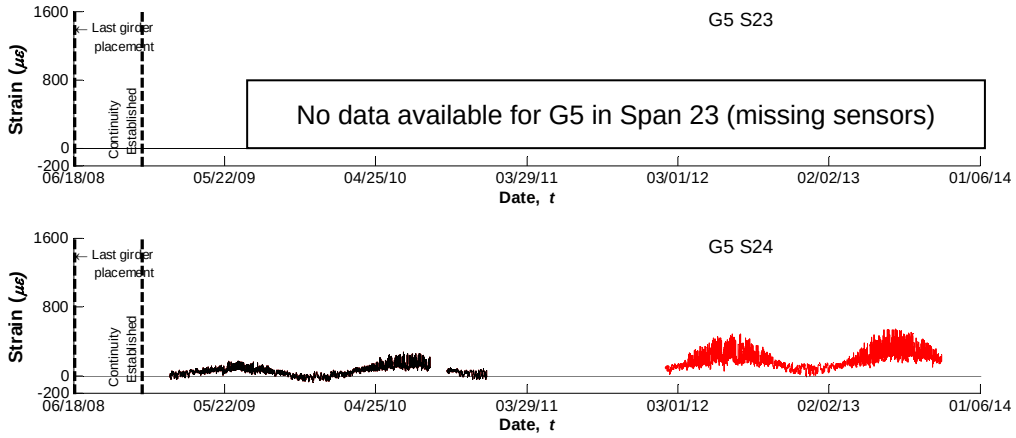

(c) Girder G5

Figure 10
Strains in hairpin bars at both sides of continuity diaphragm

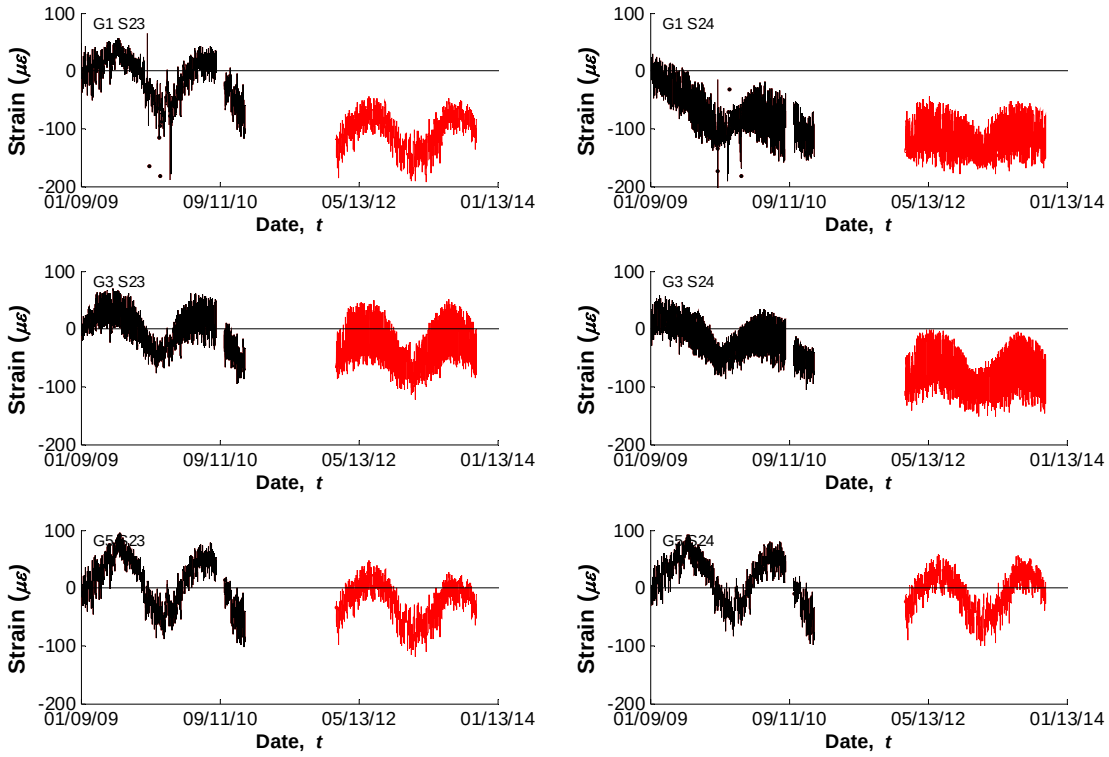

Figure 11
Surface-mounted VW strains at bottom flanges on both sides of continuity diaphragm (Girders G1, G3, and G5)

Relative Movement between Bottom Flanges in Adjacent Spans

The relative movement between the bottom flanges at the ends of the adjacent girders on both sides of the continuity diaphragm is measured using the gapmeters (DM) installed at Girders G1, G3, and G5. Any displacement captured by the gapmeters would indicate the relative movement between the bottom flanges of the girders. Positive displacements mean that the distance between the bottom flanges have increased, i.e., the girders are applying tension on the diaphragm and vice versa. Figure 12 shows a plot of the temperature corrected readings from all three gapmeters at Bent 24. The plots confirm the findings discussed earlier in the report and the even earlier in LTRC Report 477 [*3*]. Out of the three instrumented girders, Girder G3 experienced the largest gap movements. This confirms the readings shown in Figure 10, which also indicated that Girder G3 experienced larger strains than Girders G1 and G5. A gap opening equal to 0.0919 for Girder G3 translates into an equivalent, or apparent, strain over the distance between the gage ends (43 in.) of 0.0919/43=2140 $\mu\varepsilon$, as opposed to 0.0237/46=515 $\mu\varepsilon$, and 0.0474/45.5=1042 $\mu\varepsilon$ for Girders G1 and G5, respectively. These strain calculations assume that construction is monolithic, which is not the case between the girders and the continuity diaphragm where a cold joint exists. Cracking in the

diaphragm and/or the girders within the gage length also increases the displacement, hence the larger estimates than what is recorded by the hairpin sensors. The figure also confirms that the daily changes are less in the cold months (December, January, and February) than in the summer due to the smaller temperature gradients during cold months (see Figure 9), which in turn reduces girder rotations at the joint.

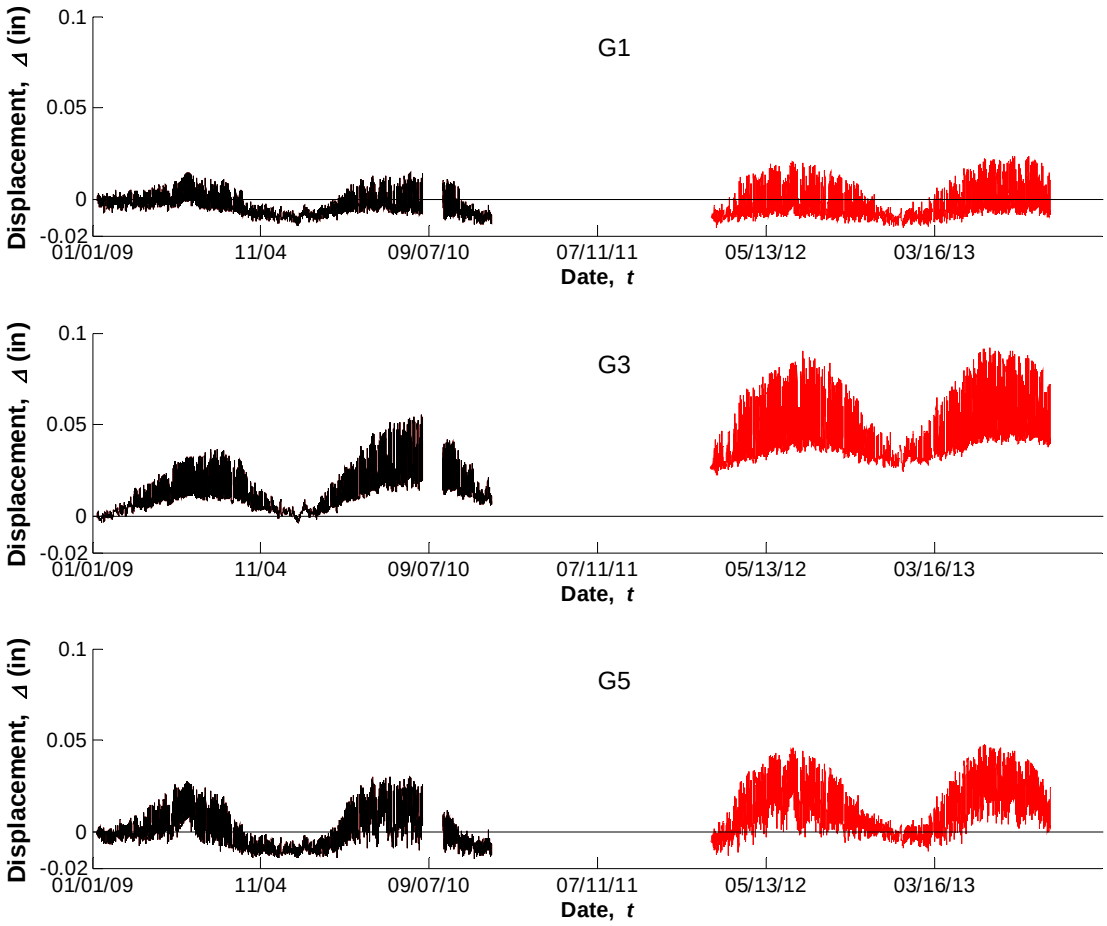

Figure 12
Gapmeter displacements for Girders G1, G3, and G5

Rotation of Girder Ends in Adjacent Spans

Figure 13 shows plots of the recorded rotations from the tiltmeters installed on the webs at girder ends on both sides of the monitored continuity diaphragm (Bent 24). The tiltmeter reading plots start at different dates reflecting the different times when trouble shooting was completed as is explained in LTRC Final Report 477 *[3]*. As was observed in this report, girder ends tilting was almost synchronized as rotations followed the same pattern and almost the same magnitude. This is more true for Girder G3 than it is for G1 and G5. It should be noted that the sensor installed on Girder G5 in Span 24 showed two abrupt shifts around

April 2012 and August 2012. The reason for these shifts is unclear, but it may be due to any impacts to the sensor housing, loosening of the anchors used to mount the sensor, or simply a sensor malfunction. The record can be easily adjusted to remove these shifts and join the different segment. However, the research team thought it was more appropriate to document the readings as they were recorded.

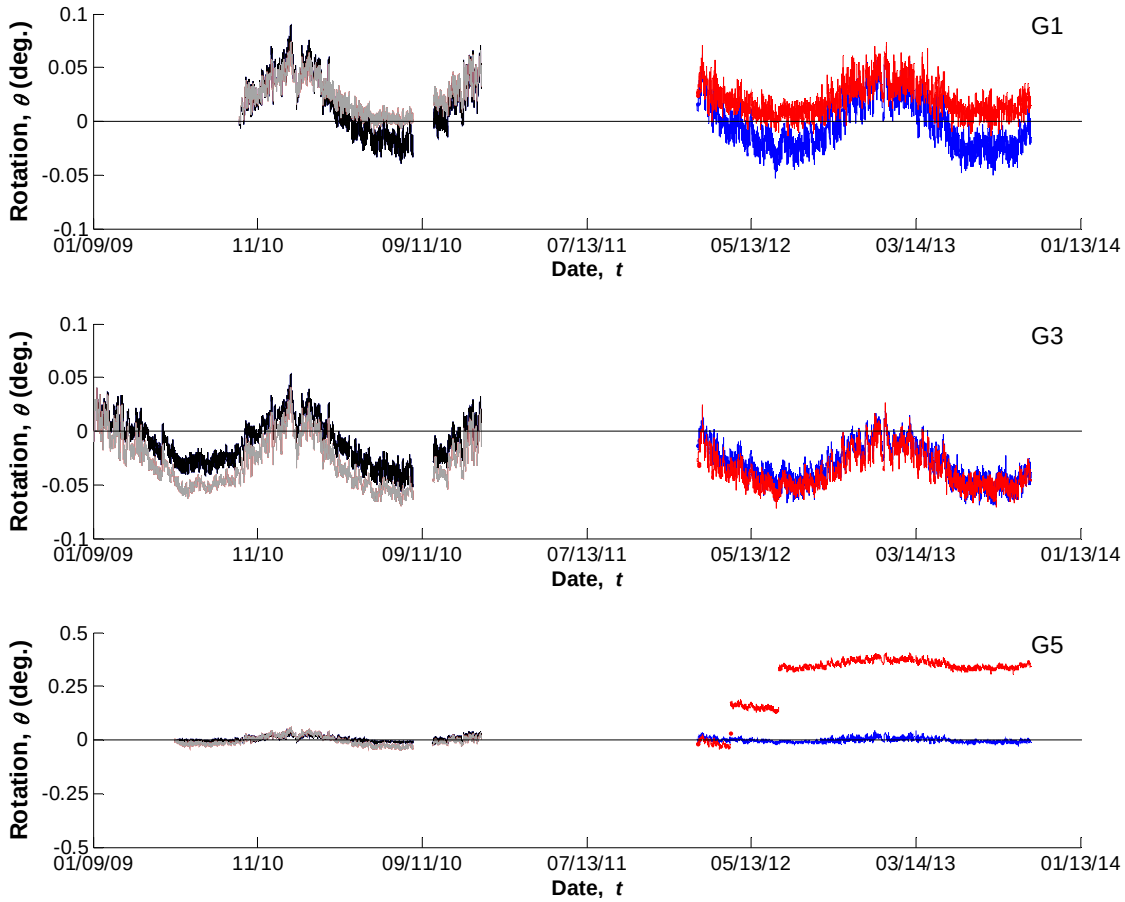

Figure 13
Rotation of girder ends (G1, G3, and G5)

Visual Inspection

The research team visited the bridge site four times during the two-year project period. As stated earlier, the dates when these visits took place were chosen to be at extreme weather conditions, i.e., hot summer months and cold or mild months. The main focus of the visits was to observe any developments in the first crack that was documented in LTRC Final Report 477 [*3*]. Documentation of any repair work and newly developed cracks was also done during these site visits.

Crack in Girder G3

Figure 14 shows the bottom flange of Girder G3 at six different times since bridge construction completion. Figure 14(a) and (b) show the crack as it was observed and documented in LTRC Final Report 477. It can be seen that the initial crack appeared about 6 months after establishing continuity, which coincides with the bridge getting exposed to hot weather conditions. The crack initially did not extend all the way to the soffit of the girder, but rather extended to only half the bottom flange height. In August 2012, it was clear that the crack grew and that the bottom flange was completely cracked. This crack helped explain the high strain readings in hairpin bars for Girder G3.

This crack triggered the first attempt to seal the crack to avoid accelerated deterioration of the girder end. When the current project started in January 2012, the research team visited the bridge site on February 24, 2012. At that time, the crack was sealed using an epoxy-like material that entirely covered the crack, which could not be seen [Figure 14(c)]. Six months later, on August 6, 2012, the second visit to the bridge site took place. Figure 14(d) shows the conditions at that time, which revealed that the epoxy-like sealant has cracked along the same path of the original crack. This was not a surprise to the research team as the used sealant was brittle and could not withstand the large strains at this location due to the thermal gradient induced restraining moment that was discussed earlier. In other words, the brittle sealant failed after less than a year once the bridge was subjected to the first cycle of hot summer weather. On March 13, 2013, the research team visited the bridge site for the third time and the same crack could still be seen [see Figure 14(e)]. In between the third and fourth site visits (around June 2013), the second attempt to seal the crack was made. The sealant for this attempt was an elastomeric, crack-bridging coating (Sikagard® Elastic Base Coat + Sikagard® 550W Elastocolor), which can accommodate strains in excess of 300% [*11, 12*]. This product was chosen primarily because of its ability to elongate to these levels without rupture, which would definitely be needed as the thermal cycles opened and closed the crack. Figure 14(f) shows the same crack location on August 22, 2013, after applying the elastomeric coating. The crack could not be seen as it was completely covered by the new coating. Although only two months had passed since applying the new coating till the time of the last site visit, those two months (July and August) are when the most severe thermal cycles take place. Therefore, it can be said that the new coating had been exposed to the most demanding conditions that caused the crack to develop initially in May 2009, and the first epoxy like sealant to crack in August 2012. In both case, the crack developed after the bridge was exposed to the first hot thermal cycle. Therefore, the research team believes that the current conditions will last for an extended period of time. Therefore, it is recommended that

the bridge be entered into a regular inspection routine (every two years), i.e., no special inspections need to be scheduled for Bridge No. 61390613004101.

(a) May 5, 2009 **(b) October 22, 2010** **(c) February 24, 2012**

(d) August 6, 2012 **(e) March 13, 2013** **(f) August 22, 2013**

Figure 14
Observed crack at bottom flange of Girder G3 at Bent 24 – Span 24

It should be noted that the elastomeric coating was applied to the diaphragms and girder ends up to a distance of about 5 ft. on both sides of the diaphragm as can be seen in Figure 15.

(a) Girder G1 at Bent 24 **(b) Diaphragm between G1 and G2 at Bent 25**

Figure 15
Extent of elastomeric coating at continuity diaphragm locations

New Girder Cracks

In addition to the old crack in Girder G3, the research team observed new cracks in Girder G4. The cracks can be seen in Figure 16. The crack features (location, width, and extents) were similar to those observed in Girder G3. This means that all girders are vulnerable to cracking like Girder G3 and G4. The crack in Girder G4 could not be correlated to any recorded strain readings as no sensors were installed at these locations.

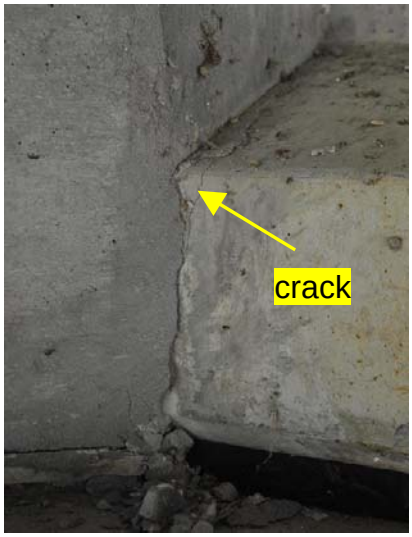

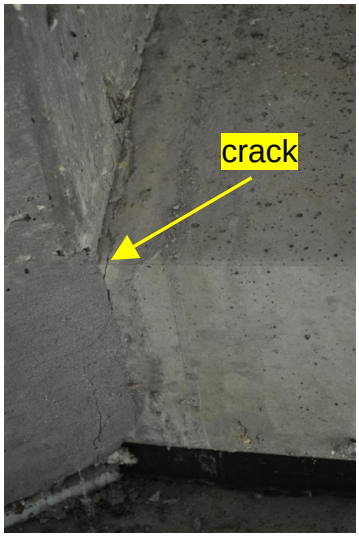

(a) Girder G4 – Span 23 - Bent 24 **(b) Girder G4 – Span 24 - Bent 25**

Figure 16
New cracks observed in Girder G4

Diaphragm cracking was also observed at exterior girders. This type of cracking is expected in light of the fact that the diaphragm is not prestressed and is responsible for transferring the tension force between adjacent girder ends. In addition to the intermediate diaphragm crack that can be seen in Figure 17, separation cracks can also be observed at the cold joint interface. Both crack types are inevitable in this type of construction. However, they are not detrimental to the prestressed girder, but can lead to spalling of diaphragm concrete if excessive. Also, cracking reduces the diaphragm stiffness, which is known to influence the level of continuity for the superstructure.

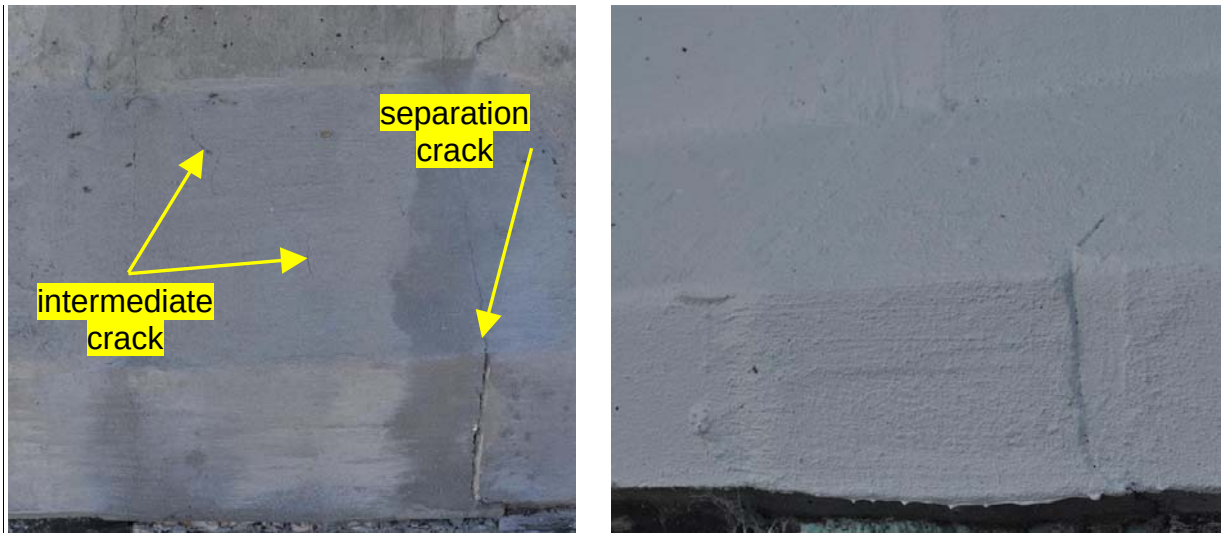

(a) Before coating (March 13, 2013) **(b) After coating (August 22, 2013)**

Figure 17
Diaphragm cracking (Girder G1)

All observed cracks could not be seen after applying the elastomeric coating to girder ends.

`mRestraint` Enhancement

Implementation of the thermal analysis described earlier in `mRestraint` is presented in this section. After entering the bridge details as described in LTRC Final Report 477, the user is prompted whether thermal analysis needs to be performed or using the window shown in Figure 18. Because the thermal analysis is based on a fiber section analysis where the cross section is sliced into multiple thin layers with different properties (width, height and material properties), the user is then prompted for the number of fibers (slices) using the window shown in Figure 19.

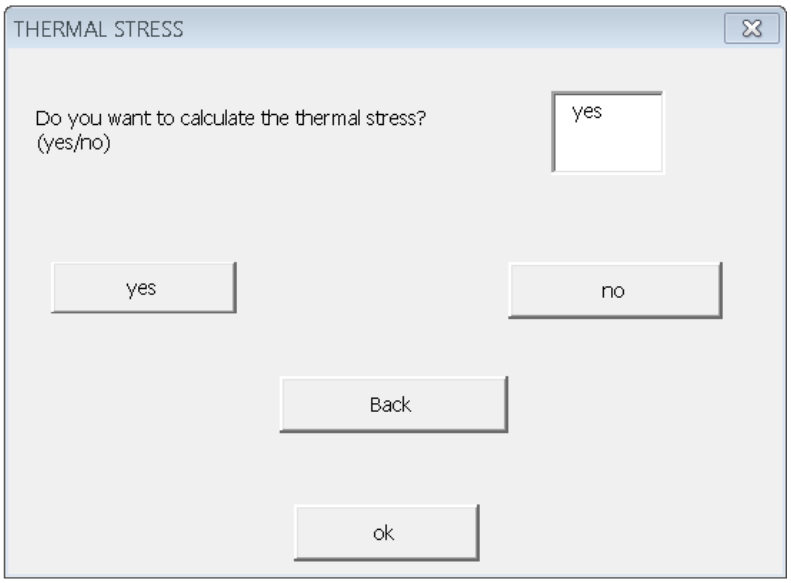

Figure 18
Main thermal stress analysis option window

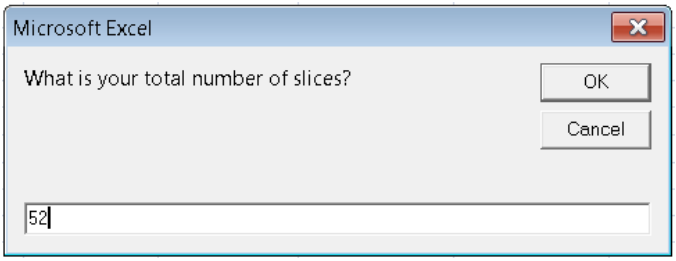

Figure 19
Window where number of fibers across section height is chosen by user

Figure 20 shows a sample output of the restraint moment, M_r, developing in a two-span bridge. The solid curve in the plot is M_r due to long-term effects without including the effect of thermal gradient. This solid curve is what the original `mRestraint` was capable of producing as a result of modifications described in LTRC Final Report 477 [*3*]. The other two dashed curves represent the predicted restraint moment due to the combined effect of long-term as well as thermal gradients. The first dashed plot represents the effect of positive thermal gradient, while the second one represents the effect of a negative thermal gradient.

It should be noted that `mRestraint` also estimates the primary thermal stresses that are not associated with any cross-sectional moment as they are balanced internally.

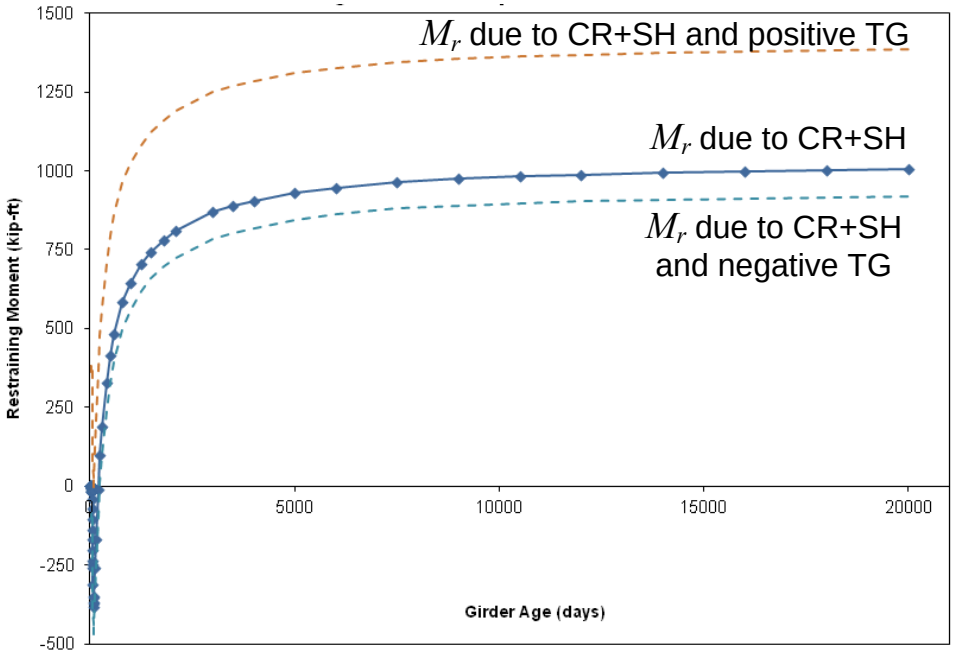

Figure 20
Sample output from `mRestraint`

A parametric study was conducted using the `mRestraint` program to study the effect of thermal gradients on the development of restraint moment. The details of the parametric study are identical to those presented in the the final report for Project 08-1ST [*3*], which is also listed in Table 2.

Table 2
Variables considered in parametric study

Parameter		**Investigated Values**				
Number of Spans		2	3	—	—	—
Span Length Ratio	2 Spans	1 : 1	0.75 : 1	0.50 : 1	—	—
	3 Spans	1 : 1 : 1	1 : 1.5 : 1	1 : 2 : 1	—	—
Diaphragm Stiffness I_d		I_g	0.50 I_g	0.25 I_g	0.125 I_g	0.05 I_g
Age of Continuity (days)		28	60	90	180	—

Figure 21 shows the effect of girder age on the development of restraint moment for two-span bridges considered in the parametric study. It should be noted that the calculated restraint moment in these plots is that caused by the thermal gradient effect in addition to the creep and shrinkage long-term effects. It can be seen that the restraint moment increases with the increase in diaphragm stiffness. It can also be seen that large differences between

adjacent span lengths lead to larger restraint moments as the shorter span lengths are stiffer and restrain girder rotation more than if the lengths of adjacent spans were equal.

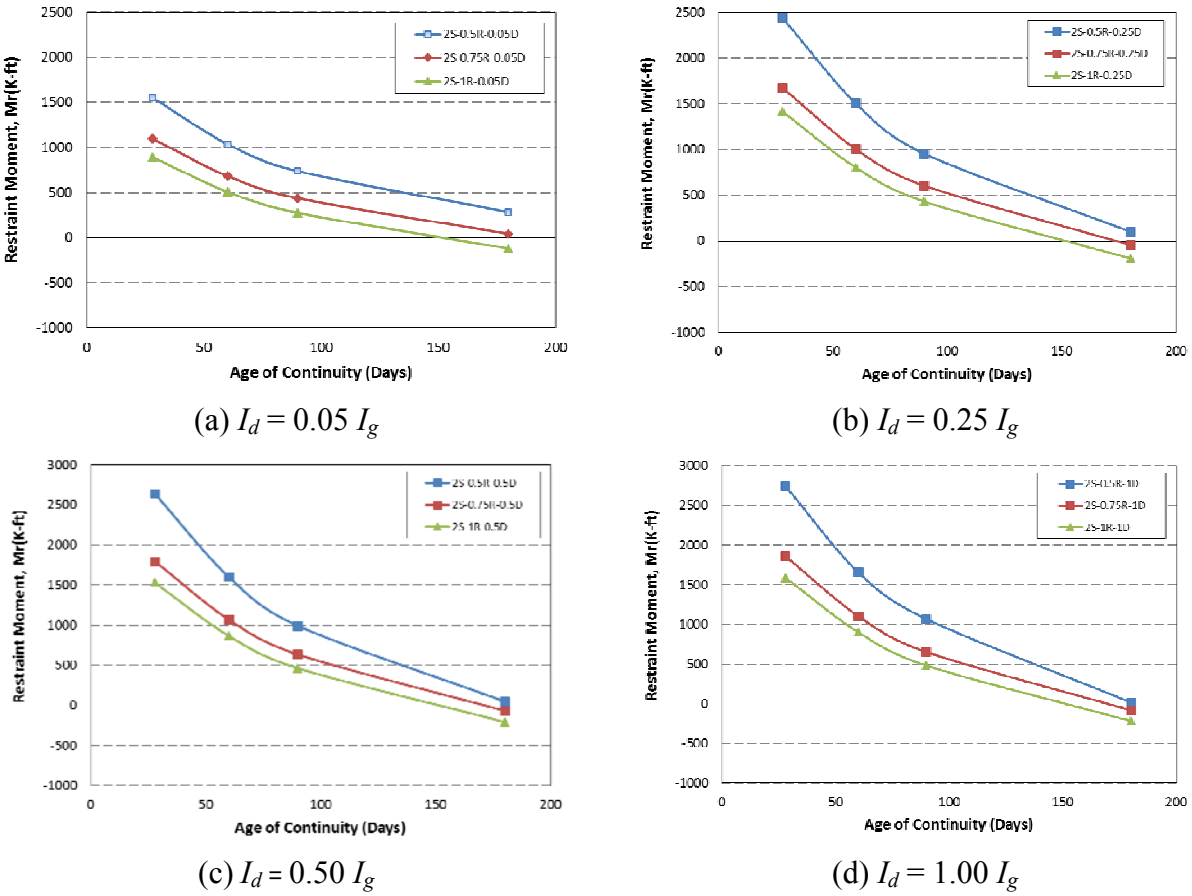

(a) $I_d = 0.05\ I_g$ (b) $I_d = 0.25\ I_g$

(c) $I_d = 0.50\ I_g$ (d) $I_d = 1.00\ I_g$

Figure 21
Effect of girder age on total developed restraint moment (2 spans – 200 days)

The results plotted in Figure 21 were then utilized to estimate a reliabile girder age after which continuity can be established with a low probability of cracking due to positive restraint moments. The girder age at the time when the positive restraint moment reaches an allowable value, $M_{r,all}$, is calculated and listed in Table 3. Four $M_{r,all}$ values were considered in determining the optimum girder age, which were taken as a percentage of the cracking moment, M_{cr}, namely 25%, 50%, 75%, and 90%. As expected the average girder age at time of establishing continuity is inversely proportional to the magnitude of the allowable moment, $M_{r,all}$. For example, if the allowable moment is set to 25% of M_{cr}, the average age of the girders for the analyzed two-span bridges is 140 days; whereas, a higher allowable moment of 75% of M_{cr}, drops the girder age to 79 days. This shows that a single value for girder age such as the 90-day recommended in NCHRP Final Report 519 is not suitable for

all bridge configurations. Furthermore, the established values for girder age vary because of the specifics of each bridge configuration (e.g., strand pattern, deck surface area to girder area ratio). To achieve a level of acceptable reliability with respect to girder end cracking, a new variable will be introduced. The new variable will be called the Reliable Age, D_r, which is the age that coorespomds to a desired probability of the restraining momement, M_r, exceeding the allowable moment, $M_{r,all}$.

$$P_f = P\left(M_r > M_{r,all}\right) \tag{13}$$

For any target, P_f, D_r can be determined using equation (14), by choosing an appropriate κ-value. For example, for a 5% probability of exceedance, κ is computed as 1.64 assuming a normal distribution. Table 3 gives different D_r values for three different P_f values, namely 2%, 5%, and 10%.

$$D_r = \mu_D + \kappa\sigma_D \tag{14}$$

Table 3
Girder age results for two-span bridge configurations

		Calculated Girder Age			
Case		M_{all}=0.25 M_{cr}	M_{all}=0.50 M_{cr}	M_{all}=0.75 M_{cr}	M_{all}=0.90 M_{cr}
2S-0.50R-0.05D		174	111	69	54
2S-0.75R-0.05D		140	90	63	52
2S-1.00R-0.05D		103	69	48	37
2S-0.50R-0.25D		157	124	91	80
2S-0.75R-0.25D		143	113	86	76
2S-1.00R-0.25D		121	89	72	61
2S-0.50R-0.50D		155	125	95	83
2S-0.75R-0.50D		143	115	89	79
2S-1.00R-0.50D		123	94	76	69
2S-0.50R-0.125D		162	122	86	74
2S-0.75R-0.125D		143	108	81	69
2S-1.00R-0.125D		116	84	64	55
2S-0.50R-1.0D		155	128	101	87
2S-0.75R-1.0D		143	116	90	81
2S-1.00R-1.0D		124	96	78	68
Mean, μ_D		**140**	**106**	**79**	**68**
Std. Dev., σ_D		**19**	**17**	**14**	**14**
Reliable Age, D_r	**P_f=0.02**	**179**	**141**	**107**	**96**
	P_f=0.05	**171**	**137**	**102**	**91**
	P_f=0.10	**164**	**127**	**97**	**86**

CONCLUSIONS

Summary

This study was conducted for the purpose of continuing to evaluate the performance of the NCHRP Final Report 519 continuity detail in Bridge No. 61390613004101 of the John James Audubon Project [*2*]. The effort is a continuation to the work that started with LTRC Project 08-1ST through which a 96-channel monitoring system comprised of embedded and surface-mounted sensors that measure strains, rotations, and gap openings was installed. The instrumented segment of Bridge No. 61390613004101 was chosen for monitoring because it is skewed and uses Bulb-T (BT-72) girders. Data from almost a 24-month period has been collected and added to data recorded from the initial monitoring period to provide readings over a period of almost five years (2008 – 2013) including a gap of almost two years in between projects. The data was processed and analyzed to better understand the performance of the new detail.

Visual inspections of the monitored segments were conducted during four site visits that were chosen to be in different seasonal times to study the performance under hot summer months as well as cold/mild winter months.

Finally, the `RESTRAINT` program, developed as part of NCHRP Final Report 519 and modified as part of LTRC Project 08-1ST (`mRESTRAINT`), was enhanced by adding the capability to conduct primary and secondary thermal analyses.

Conclusions

The conclusions from this study can be summarized in the following:

1. Positive restraint moment can cause cracking in the diaphragm and/or girder ends. New cracks were observed in bottom flanges at girder ends during visual inspections as a result of local stress concentrations around hairpin bars. These cracks are in addition to the old crack that was documented in LTRC Final Report 477 [*3*]. Cracking can affect the performance of the diaphragm and hence the bridge. More importantly, girder cracking may have adverse effects on the durability and on the shear capacity of the girders. Therefore, special care should be given to the level of positive restraint moment during design.

2. Seasonal and daily temperature variations can cause large restraint moments in the bridge, especially temperature gradients. The level of restraint moment due to the combined seasonal and daily temperature is probably the most important factor in the

design of this detail, since the designer has no influence on the temperatures at the bridge site. The other positive-moment causing factor, i.e., girder creep caused by prestressing forces, can be greatly reduced by not introducing continuity until a large portion of the creep takes place prior to pouring the diaphragm.

3. The first repair attempt of the crack in Girder G3 used an epoxy-like sealant which was not successful in sustaining one hot summer seasonal cycle due to its brittleness. The second attempt, which relied on an elastomeric crack-bridging coating with ultra high stretching capabilities, seems to be working. After two hot summer months (July and August), no surface cracks were observed.

4. Sensor readings indicate that most of the long-term effects such as creep have already taken place.

5. The monitoring system is now over five years old. At this age, some maintenance work may be needed to troubleshoot some of the sensors that are exhibiting erratic behavior such as shifting or large fluctuations.

6. The parametric study conducted using the enhanced `mRESTRAINT` program revealed that a single value for girder age such as the 90-day recommended in NCHRP Final Report 519 is not suitable for all bridge configurations. A statistical approach was introduced to determine a newly defined variable (Reliable Age, D_r) that ensures that the probability of exceeding the allowable moment is equal to target value. Preliminary girder age values were determined for three different P_f values, namely 2%, 5%, and 10%.

RECOMMENDATIONS

Based on the findings of this project, which confirm earlier findings in the final report of LTRC Project 08-1ST, the research team recommends that a simpler detail that eliminates the expansion joint without developing large continuity moment over the supports be adopted for Louisiana bridges. This can be achieved by pouring continuous decks over simply supported girders to develop what is normally referred to as partial integration. Large thermal gradients in Louisiana during summer months are the norm and can cause large restraint moments if full integration details are employed.

If employment of the NCHRP Final Report 519 positive moment continuity is inevitable such as the case in design-build projects, a thorough investigation of its benefits, both structurally and economically, on a per project basis should be conducted. The investigation should consider all factors that contribute to the development of the positive moments acting on the continuity detail including creep due to prestressing forces, differential shrinkage, and seasonal as well as daily thermal variations. Special consideration shall be given to the effects of temperature gradient in the design of this detail.

Temperature gradient effects, which is one of the most important causes of positive restraint moment, must be considered in the design of bridges employing the new detail. The modified `RESTRAINT` program (`mRESTRAINT`) in its latest version is capable of conducting primary and secondary thermal analysis of continuous girder bridges. It is therefore recommended that thermal effects be studied using `mRESTRAINT` or any other structural analysis tools with thermal analysis capabilities.

Regular inspection routines (every two years) of the monitored segment are recommended since it appears that most of the creep effects have already taken place and the likelihood of major changes in short time intervals is low.

ACRONYMS, ABBREVIATIONS, & SYMBOLS

AASHTO	The American Association of State Highway and Transportation Officials
BDM	Bridge Design Manual
DOT	Department of transportation
DOTD	Department of Transportation and Development
CIP	Cast-in-place
D_r	Reliable Age
EC	Sisterbar
E_c	Modulus of elasticity of concrete
ES	Strandmeter
GUI	Graphical User Interface
LRFD	Load and Resistance Factor Design
LSD	Limit State Design
LTRC	Louisiana transportation research center
MUX	Multiplexer
M'	Final restraint moment due to secondary thermal stress effects
$M_{r,all}$	Allowable restraint moment
M_{cr}	Cracking moment
M_r	Restraint Moment
n	Distance between the neutral axis and any arbitrary datum
NCHRP	National Cooperative Highway Research Program
PCA	Portland Cement Association
PCBT	Precast concrete bulb tee girders
PCI	Prestressed Concrete Institute
PSC	Prestressed concrete
P_f	Probability of exceeding $M_{r,all}$
PRC	Project Review Committee
P_e	Effective prestressing force
SHM	Structural Health Monitoring
TM	Tiltmeter
VBA	Visual Basic
VW	Vibrating wire strain gauge
y_i	Centroidal height above the datum of the i-th fiber element
α_c	Coefficient of thermal expansion of concrete
ε_0	Axial strain at $y = 0$

ε_y	Axial strain at depth y
θ_i	Average temperature change of the i-th fiber element
$\theta_{(y)}$	Change in temperature
ψ	Final girder curvature
$\mu\varepsilon$	Microstrain
μ_D	Average girder age in days
σ_D	Standard deviation of girder age in days

REFERENCES

1. Bridge Design Section. "Bridge Design Manual." 4th English Edition, State of Louisiana Department of Transportation and Development, Baton Rouge, LA, 2005.

2. Miller, R. A.; Castrodale, R.; Mirmiran, A.; and Hastak, M. "Connection of Simple-Span Precast Concrete Girders for Continuity." *NCHRP Report 519*, Transportation Research Board, Washington, D.C., 2004.

3. Okeil, A. M.; Cai, C. S.; Chebole, V.; and Hossain, T. "Evaluation of Continuity Detail for Precast Prestressed Girders." *477*, Louisiana Transportation Research Center, Baton Rouge, LA, 2011.

4. ASTM Standard C 39. "Standard Test Method for Compressive Strength of Cylindrical Concrete Specimens," ASTM International, West Conshohocken, PA, 2005.

5. ASTM Standard C 469. "Standard Test Method for Static Modulus of Elasticity and Poisson's Ratio of Concrete in Compression," ASTM International, West Conshohocken, PA, 2002.

6. ASTM Standard C 78. "Standard Test Method for Flexural Strength of Concrete (Using Simple Beam With Third-Point Loading)," ASTM International, West Conshohocken, PA, 2002.

7. ASTM Standard C 496. "Standard Test Method for Splitting Tensile Strength of Cylindrical Concrete Specimens," ASTM International, West Conshohocken, PA, 2004.

8. Choquet, P.; Juneau, F.; DeBreuille, P. J.; and Bessette, J. "Reliability, Long-Term Stability and Gage Performance of Vibrating Wire Sensors With Reference to Case Histories," *5th International Symposium Field Measurements in Geomechanics*, Taylor & Francis, Singapore, 1999, pp. 49-54.

9. Bordes, J. L.; and DeBreuille, P. J. "Some Facts about Long-Term Reliability of Vibrating Wire Instruments," *Reliability of Geotechnical Instrumentation*, Natl Research Council, Transportation Research Board, Washington, DC, USA, 1985, pp. 20-27.

10. Priestley, M. J. N. "Long Term Observations of Concrete Structures. Analysis of Temperature Gradient Effects," *Materials and Structures/Materiaux et Constructions*, No. 106, 1985, pp. 309-316.

11. Sika Corporation. "Sikagard® 550W Elastocolor." http://usa.sika.com/dms/getdocument.get/b0fe2696-0707-3b80-9fe2-0aec84f3dcd4/pds-cpd-Sikagard%20550W%20Elastocolor-us.pdf (accessed February 17, 2014).

12. Sika Corporation. "Sikagard® Elastic Base Coat." http://usa.sika.com/dms/getdocument.get/d512da72-ad54-3994-a668-934e12d48704/pds-cpd-Sikagard%20Elastic%20Base%20Coat-us.pdf (accessed February 17, 2014).

APPENDIX A

Details of Installed Sensors

Table 4
Installed sensor details

MUX 1					
Logger Ch.	Mux Chan	SN	Type	Cal	Location
1	1	7885	ES	3.07	G1 Span 24 (Support - Bottom)
2	2	7886	ES	3.06625	G1 Span 24 (Support - Bottom)
3	3	10244	ES	3.04125	G1 Span 23 (Support - Bottom)
4	4	10245	ES	3.04375	G1 Span 23 (Support - Bottom)
5	5	22073	EC	0.347	G1 Span 24 (Support - Top)
6	6	20554	ES	3.07	G2 Span 24 (Support - Top)
7	7	15373	TM	0.002488	G1 Main Span 24 (+ Towards Mid Span)
8	8	15963	TM	0.002452	G1 Main Span 23 (+ Towards Mid Span)
9	9	21547	DM2	0.0004124	G1 Connection
10 through 16	10 - 16	-	-	-	
MUX 2					
Logger Ch.	Mux Chan	SN	Type	Cal	Location
17	1	-	VW	0.96	G1 Span 24 (Support -Top)
18	2	-	VW	0.96	G1 Span 24 (Support - Middle)
19	3	-	VW	0.96	G1 Span 24 (Support - Bottom)
20	4	-	VW	0.96	G1 Span 23 (Support -Top)
21	5	-	VW	0.96	G1 Span 23 (Support -Middle)
22	6	-	VW	0.96	G1 Span 23 (Support -Bottom)
23 through 32	7 - 16	-	-	-	-
MUX 3					
Logger Ch.	Mux Chan	SN	Type	Cal	Location
33	1	-	VW	0.96	G5 Span 24 (Support -Top)
34	2	-	VW	0.96	G5 Span 24 (Support - Middle)
35	3	-	VW	0.96	G5 Span 24 (Support - Bottom)
36	4	-	VW	0.96	G5 Span 23 (Support - Top)
37	5	-	VW	0.96	G5 Span 23 (Support - Middle)
38	6	-	VW	0.96	G5 Span 23 (Support - Bottom)
39	7	-	VW	0.96	G3 Span 24 (Support - Top)
40	8	-	VW	0.96	G3 Span 24 (Support - Middle)
41	9	-	VW	0.96	G3 Span 24 (Support - Bottom)
42	10	-	VW	0.96	G3 Span 23 (Support - Top)
43	11	-	VW	0.96	G3 Span 23 (Support - Middle)
44	12	-	VW	0.96	G3 Span 23 (Support - Bottom)
45	13	10240	ES	3.0525	G5 Span 24 (Support - Bottom)
46	14	10241	ES	3.05	G5 Span 24 (Support - Bottom)
47	15	10432	EC	0.346	G5 Span 24 (Support - Top)
48	16	20552	ES	3.06375	G4 Span 24 (Support - Top)

Table 4 (continued)
Installed sensor details

MUX 4					
Logger Ch.	Mux Chan	SN	Type	Cal	Location
49	1	7882	ES	3.06625	G3 Span 24 (Support - Bottom)
50	2	10242	ES	3.045	G3 Span 23 (Support - Bottom)
51	3	10243	ES	3.05	G3 Span 23 (Support - Bottom)
52	4	10252	ES	3.05	G3 Span 24 (Support - Bottom)
53	5	22072	EC	0.355	G3 Span 24 (Support - Top)
54	6	15966	TM	0.002518	G5 Main Span 24 (+ Towards Bent 24)
55	7	15964	TM	0.002468	G3 Main Span 24 (+ Towards Main Span)
56	8	15965	TM	0.002449	G3 Main Span 23 (+ Towards Mid Span)
57	9	15967	TM	0.002465	G5 Main Span 23 (+ Towards Mid Span)
58	10	21549	DM2	0.0004115	G3 Connection
59	11	21548	DM2	0.0004107	G5 Connection
60 through 64	12 - 16	-	-	-	-

MUX 5					
Logger Ch.	Mux Chan	SN	Type	Cal	Location
65	1	-	VW	0.96	G5 Span 24 (Midspan - Top)
66	2	-	VW	0.96	G5 Span 24 (Midspan - Middle)
67	3	-	VW	0.96	G5 Span 24 (Midspan - Bottom)
68	4	10430	EC	0.345	G5 Span 24 (Midspan - Top)
69	5	10431	EC	0.343	G5 Span 24 (Midspan- Bottom)
70	6	10435	EC	0.354	G5 Span 24 (Midspan - Deck)
71	7	-	VW	0.96	G2 Span 24 (Midspan - Bottom)
72	8	-	VW	0.96	G1 Span 24 (Midspan - Bottom)
73 through 80	9 - 16	-	-	-	-

MUX 6					
Logger Ch.	Mux Chan	SN	Type	Cal	Location
81	1	-	VW	0.96	G3 Span 24 (Midspan -Top)
82	2	-	VW	0.96	G3 Span 24 (Midspan - Middle)
83	3	-	VW	0.96	G3 Span 24 (Midspan - Bottom)
84	4	-	VW	0.96	G4 Span 24 (Midspan -Top)
85	5	-	VW	0.96	G4 Span 24 (Midspan -Middle)
86	6	-	VW	0.96	G4 Span 24 (Midspan -Bottom)
87	7	7883	ES	3.0475	G3 Span 24 (Midspan -Top)
88	8	7884	ES	3.075	G3 Span 24 (Midspan -Bottom)
89	9	10250	ES	3.05625	G4 Span 24 (Midspan - Bottom)
90	10	10251	ES	3.02625	G4 Span 24 (Midspan - Top)
91	11	10426	EC	0.343	G4 Span 24 (Midspan - Top)
92	12	10427	EC	0.351	G4 Span 24 (Midspan - Bottom)
93	13	10428	EC	0.349	G3 Span 24 (Midspan -Top)
94	14	10429	EC	0.351	G3 Span 24 (Midspan -Bottom)
95	15	10433	EC	0.351	G3 Span 24 (Midspan - Deck)
96	16	10434	EC	0.344	G4 Span 24 (Midspan - Deck)

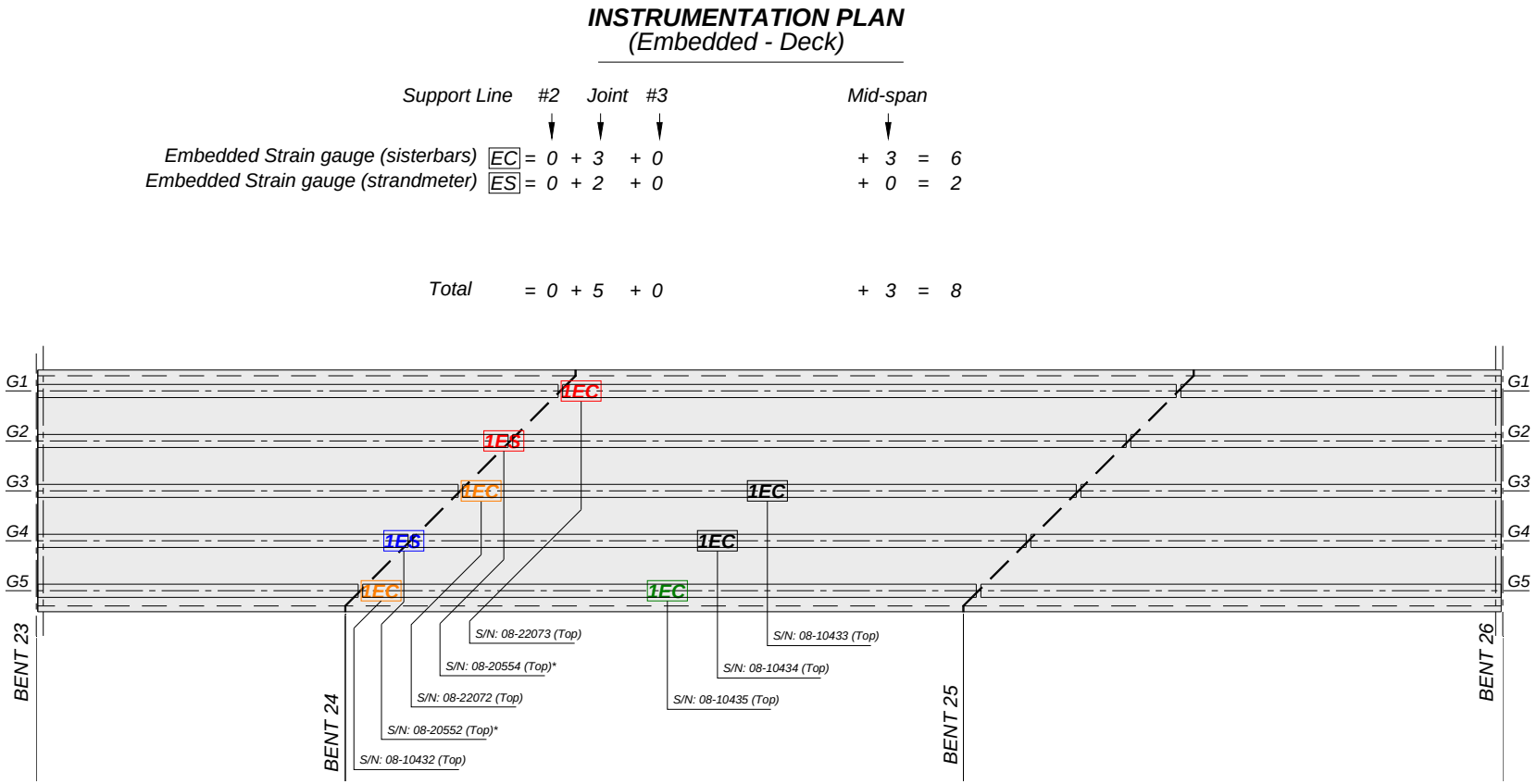

Figure 22
Distribution of embedded sensors in deck

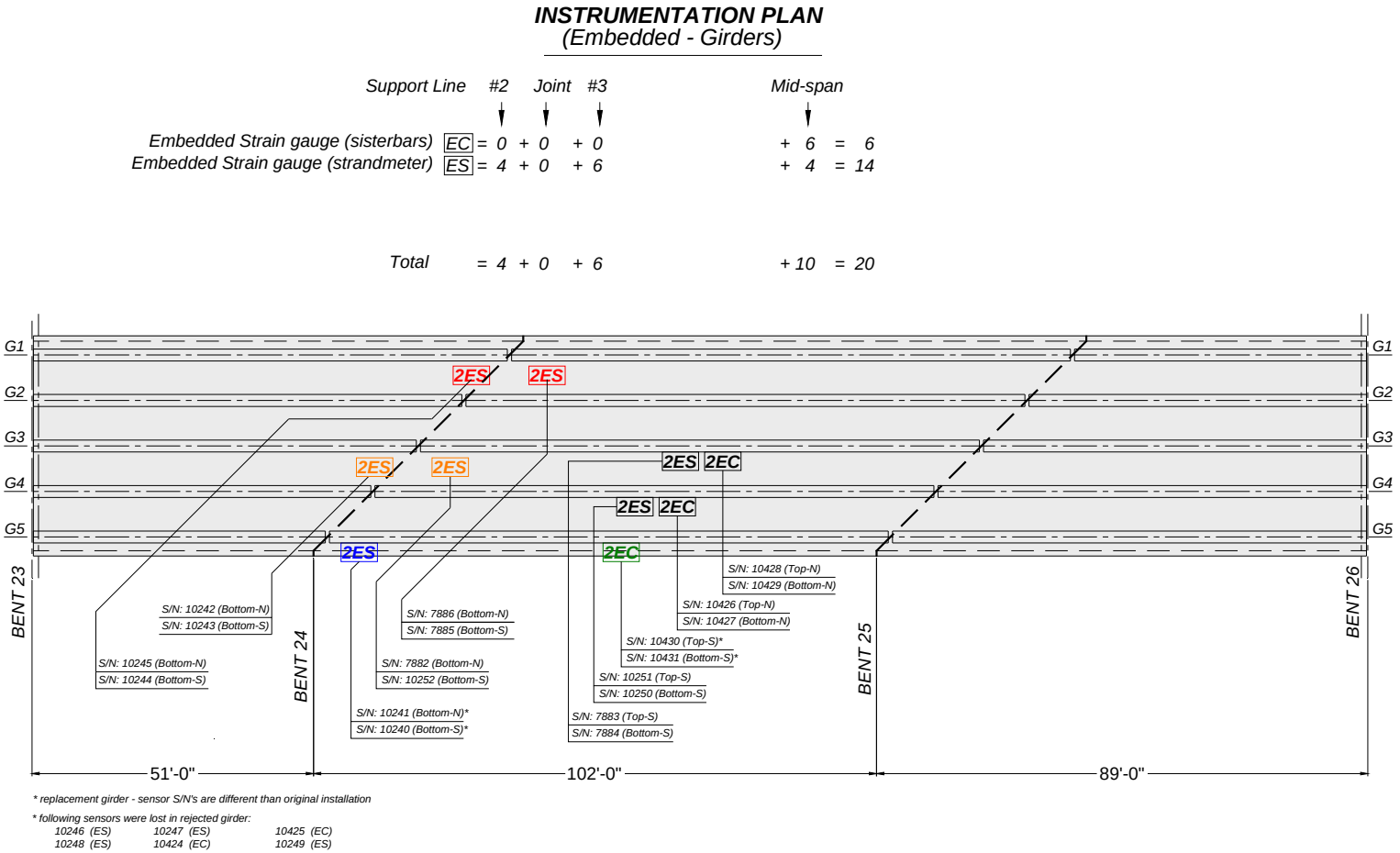

Figure 23
Distribution of embedded sensors in girders

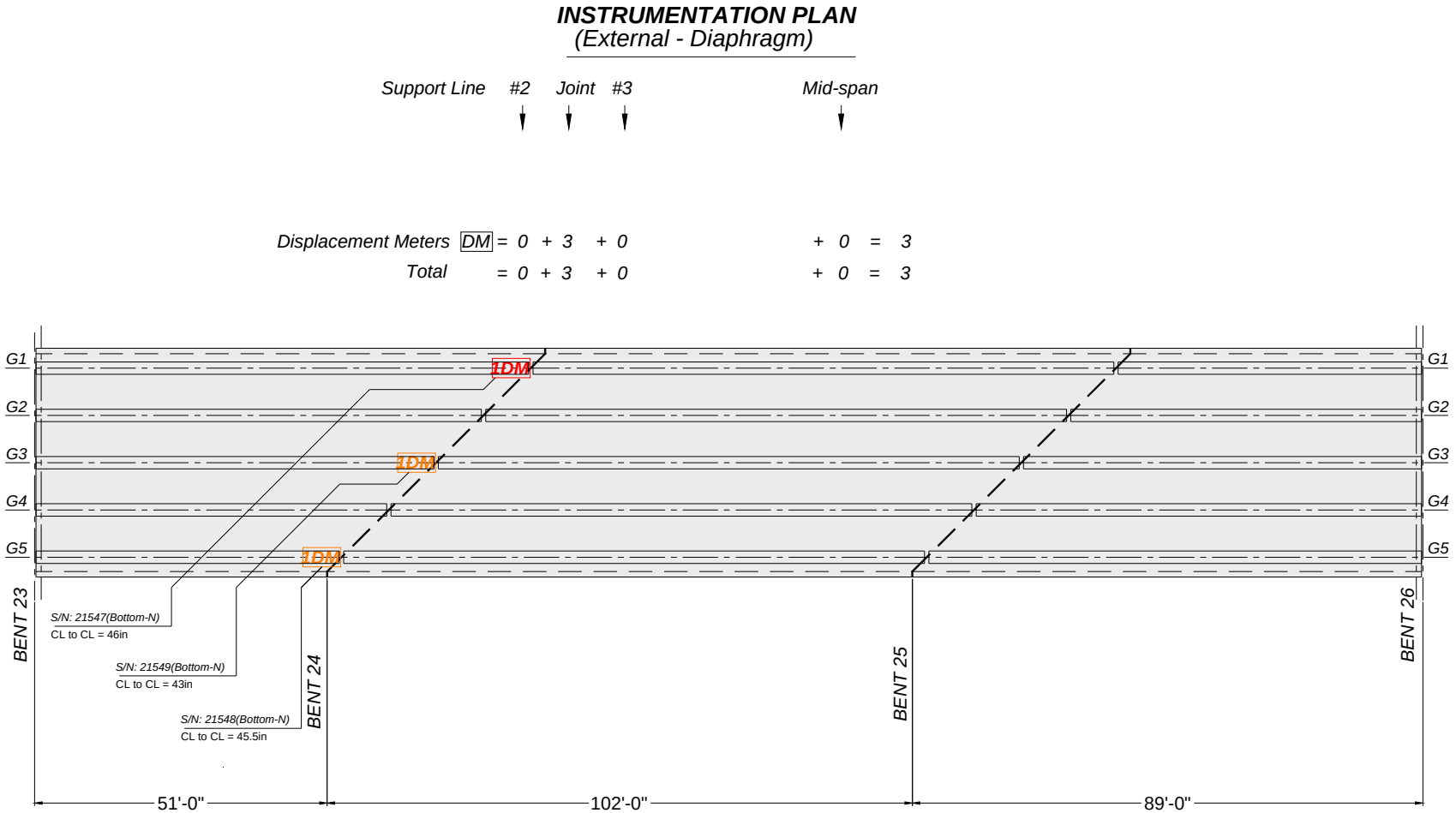

Figure 24
Distribution of gap meters

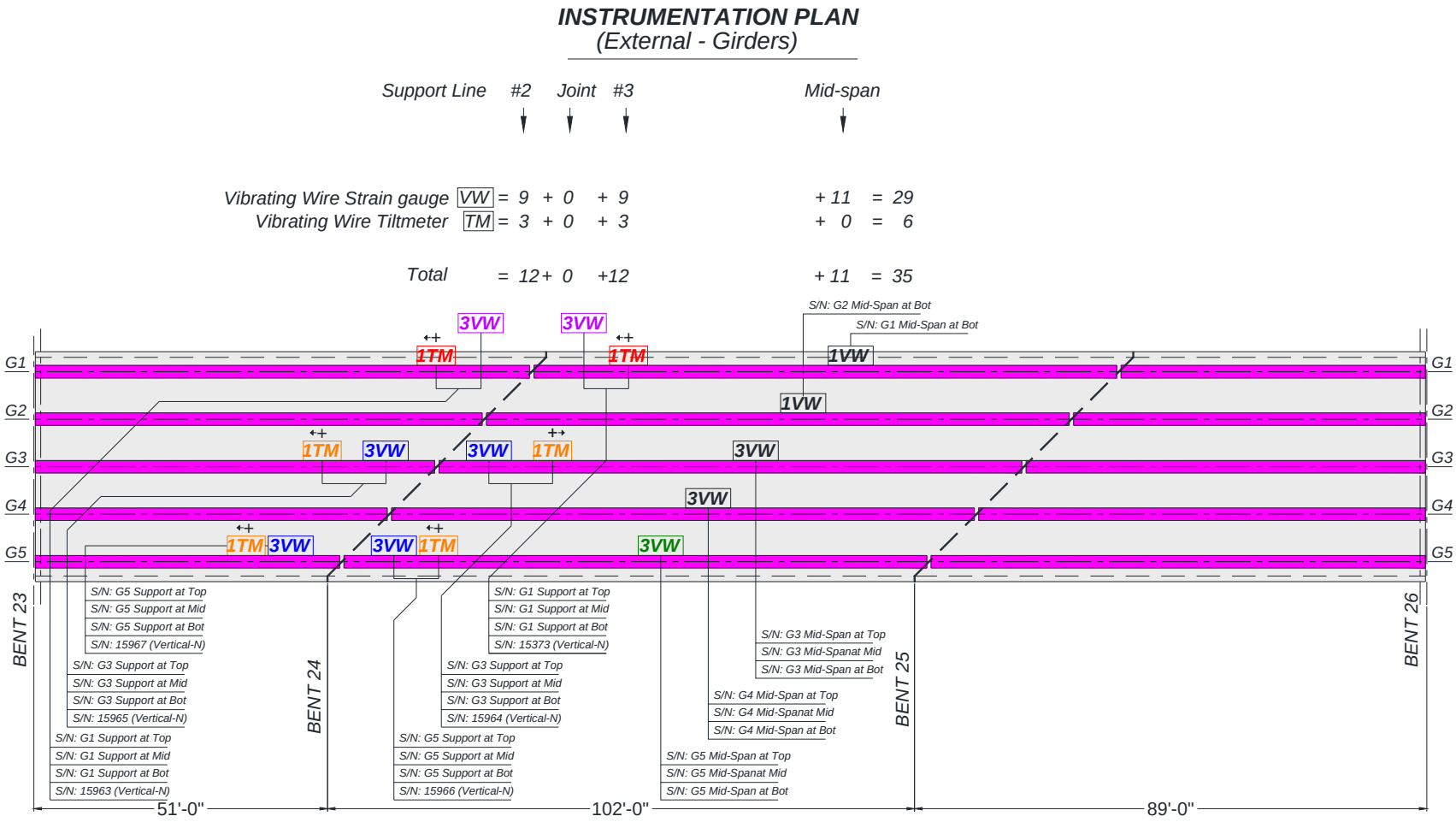

Figure 25
Distribution of surface mounted sensors

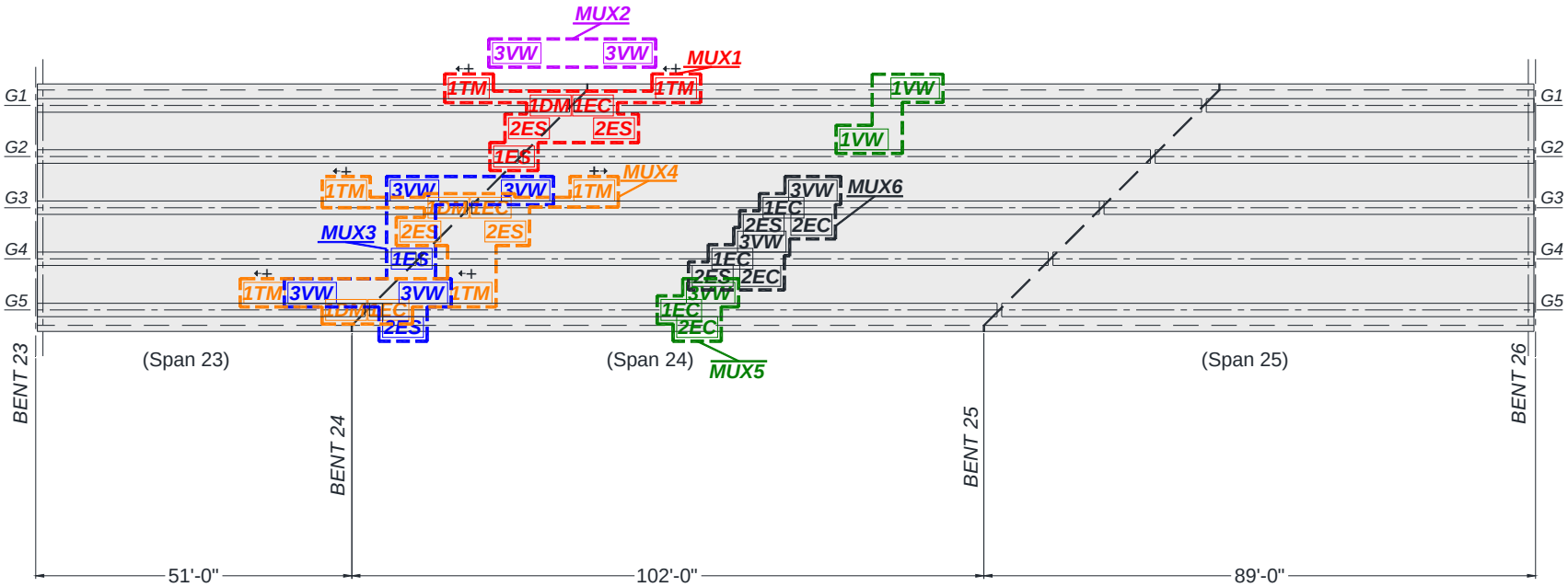

Figure 26
Distribution of sensors on system multiplexers (MUX1 through MUX6)

APPENDIX B

Recorded Readings from All Sensors

The following plots are a documentation of all sensor readings obtained since the beginning of installation of embedded sensors at the casting yard on June 18, 2008, as part of LTRC Project 08-1ST through the end of the current project (LTRC Project 12-1ST) on December 31, 2013. No data was collected during the period between the end of LTRC Project 08-1ST on December 10, 2010, and the reinstatement of the monitoring system for the current project on February 2012, hence the gap that appears in the plots for all sensors. It should be noted that surface mounted sensors were installed at the bridge site, and therefore, their plots cover the period from January 9, 2009, through December 2013.

Note: Three plots are provided for each sensor. The first is the temperature reading obtained from the vibrating wire gage readings. The second and third are plots of the relative uncorrected and relative temperature corrected sensor readings (e.g., strain, gap, slope).

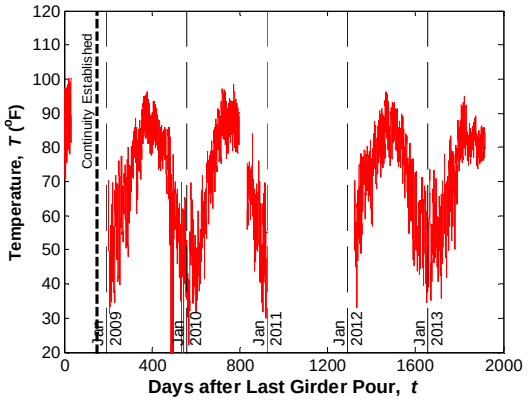

a) Temperature reading of the sensor

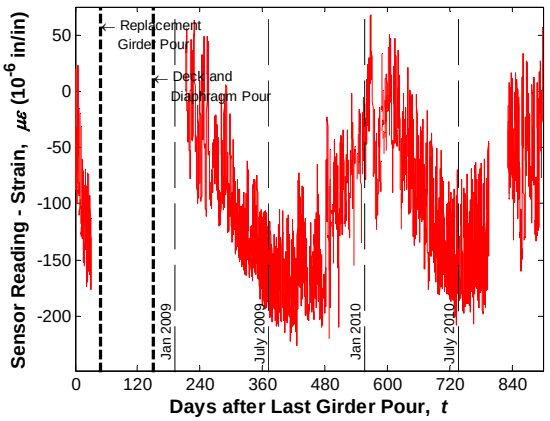

b) Sensor reading without temperature correction

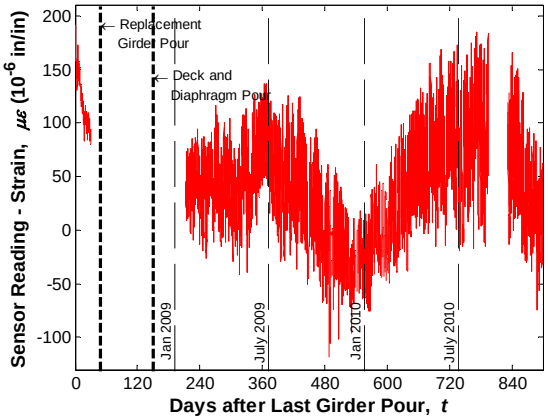

c) Sensor reading after temperature correction

Figure 27
Sensor No. 1, Location G1S24, Support Bottom (ES)

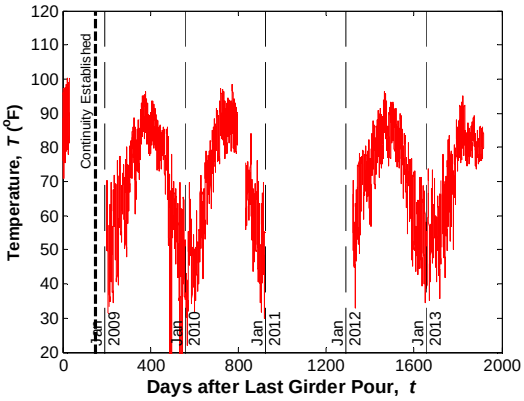

a) Temperature reading of the sensor

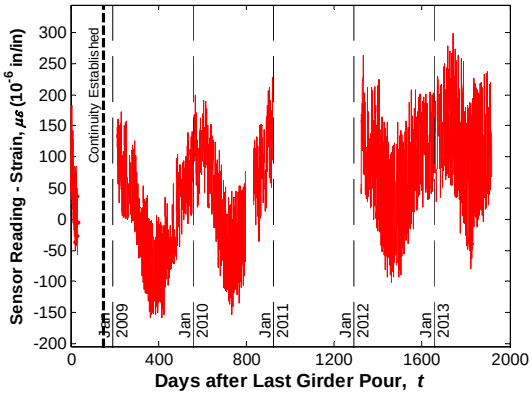

b) Sensor reading without temperature correction

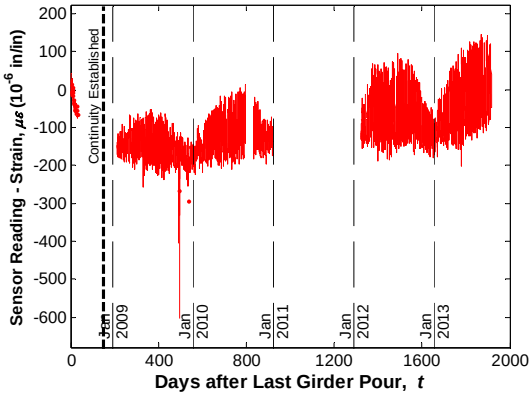

c) Sensor reading after temperature correction

Figure 28
Sensor No. 2, Location G1S24, Support Bottom (ES)

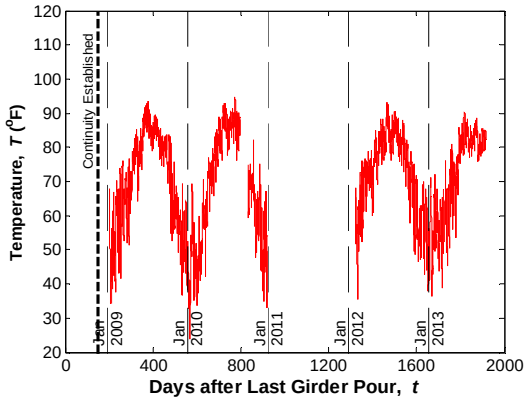

a) Temperature reading of the sensor

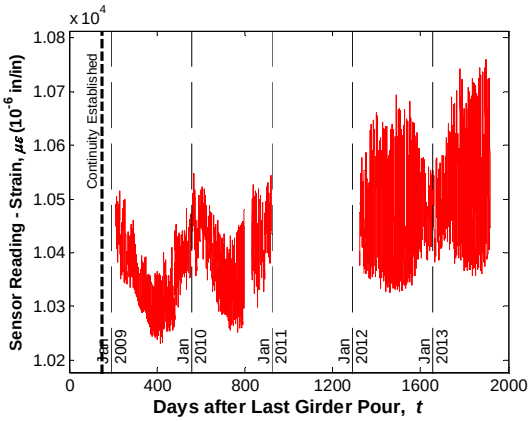

b) Sensor reading without temperature correction

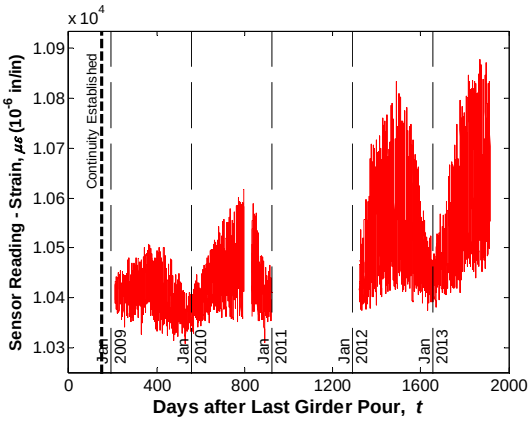

c) Sensor reading after temperature correction

Figure 29
Sensor No. 3, Location G1S23, Support Bottom (ES)

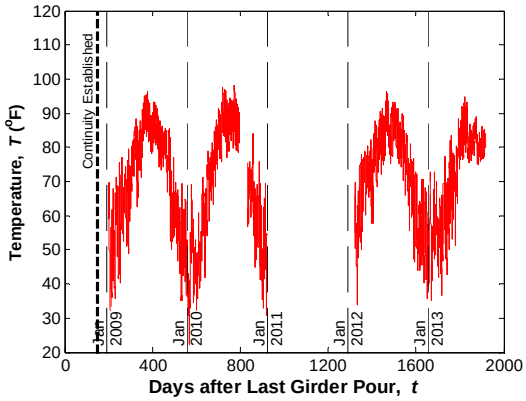

a) Temperature reading of the sensor

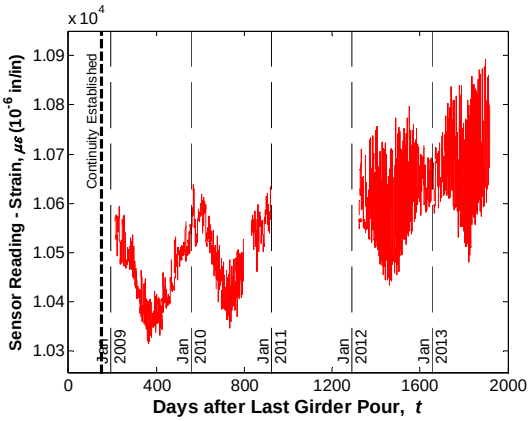

b) Sensor reading without temperature correction

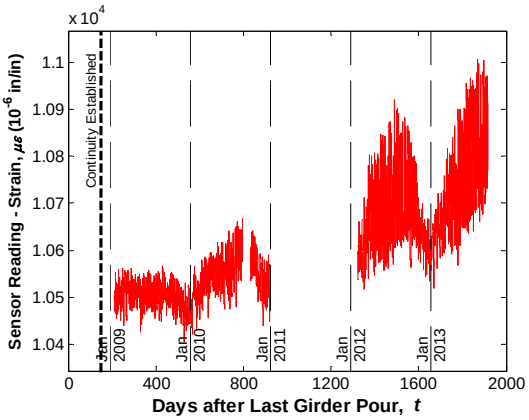

c) Sensor reading after temperature correction

Figure 30
Sensor No. 4, Location G1S23, Support Bottom (ES)

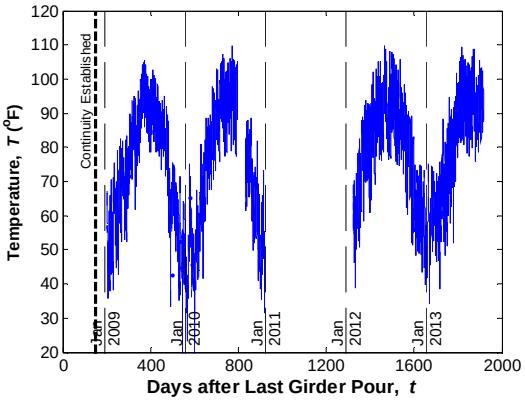

a) Temperature reading of the sensor

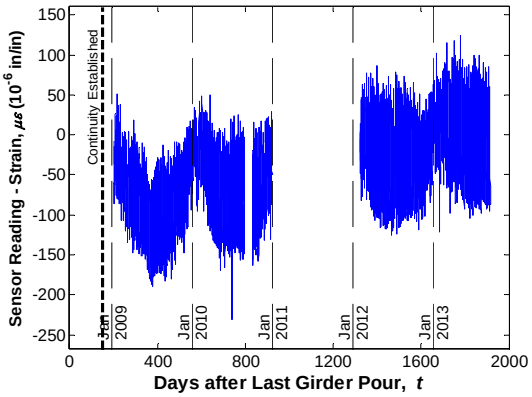

b) Sensor reading without temperature correction

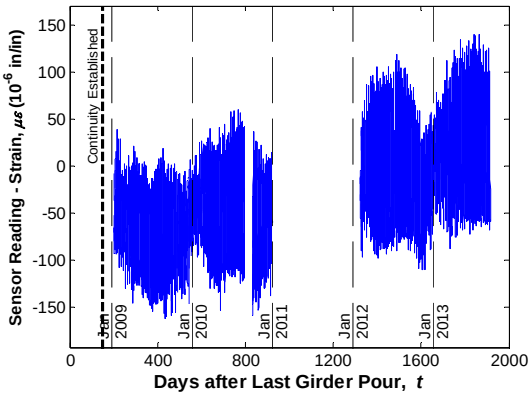

c) Sensor reading after temperature correction

Figure 31
Sensor No. 5, Location G1S24, Support Top (EC)

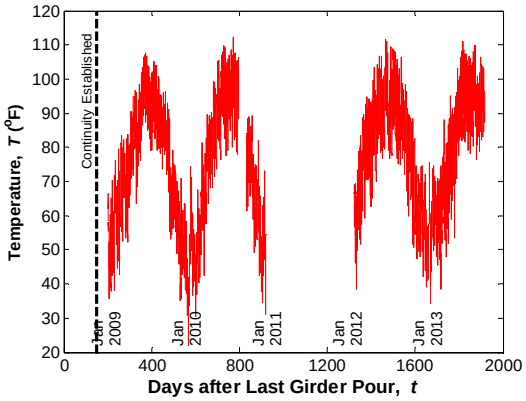

a) Temperature reading of the sensor

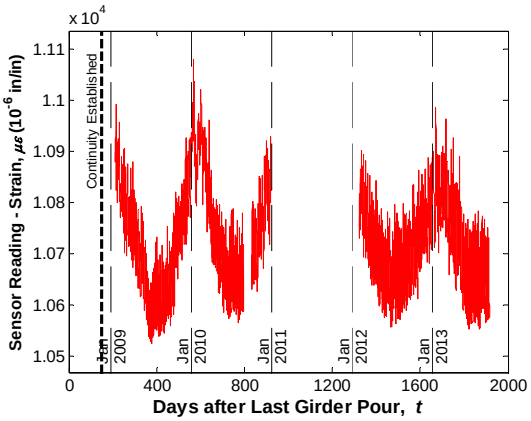

b) Sensor reading without temperature correction

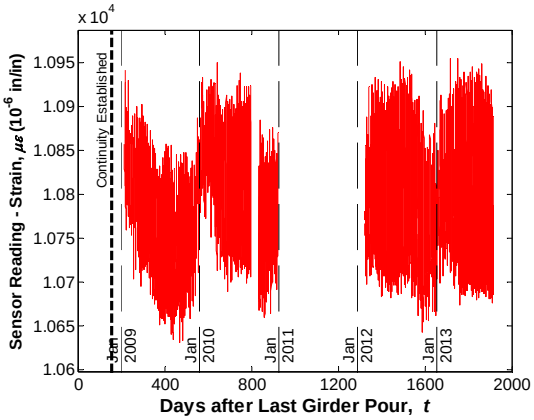

c) Sensor reading after temperature correction

Figure 32
Sensor No. 6, Location G2S24, Support Top (ES)

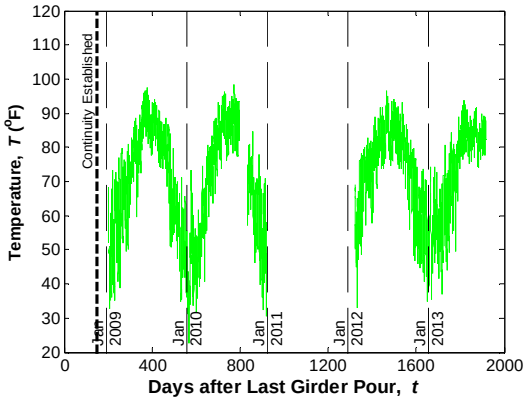

a) Temperature reading of the sensor

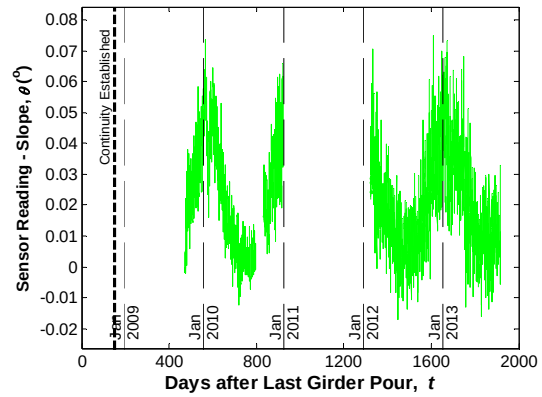

b) Sensor reading without temperature correction

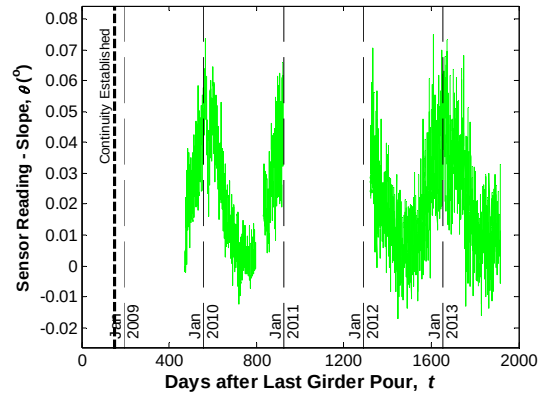

c) Sensor reading after temperature correction

Figure 33
Sensor No. 7, Location G1S24, Support (TM)

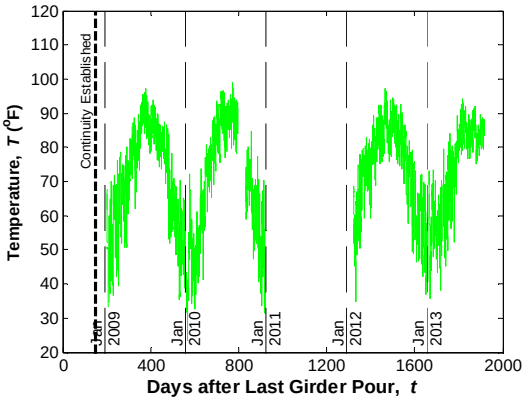

a) Temperature reading of the sensor

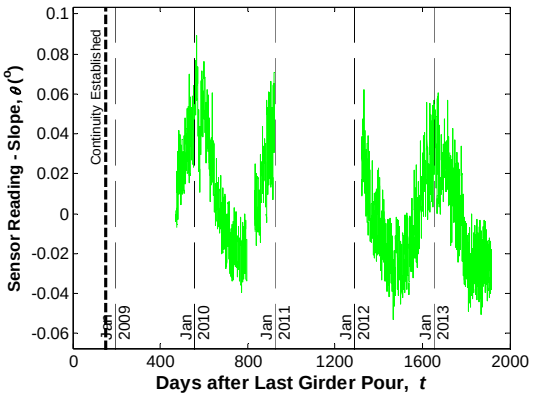

b) Sensor reading without temperature correction

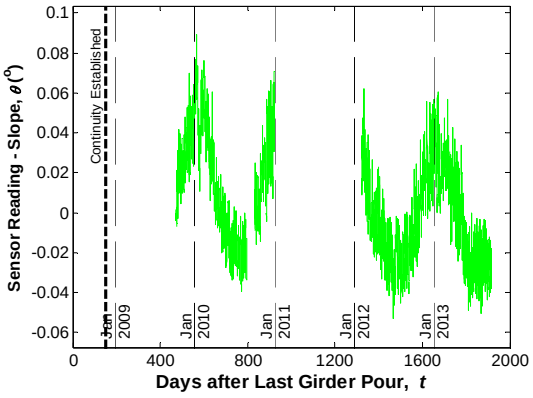

c) Sensor reading after temperature correction

Figure 34
Sensor No. 8, Location G1S23, Support (TM)

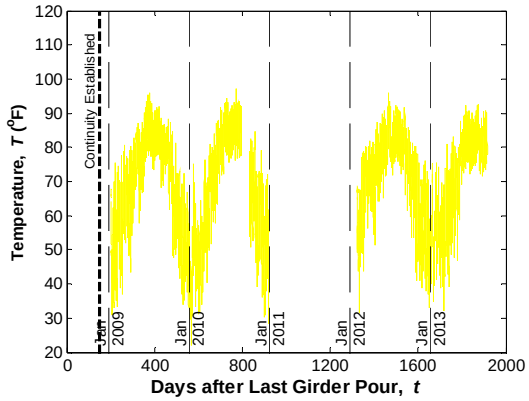

a) Temperature reading of the sensor

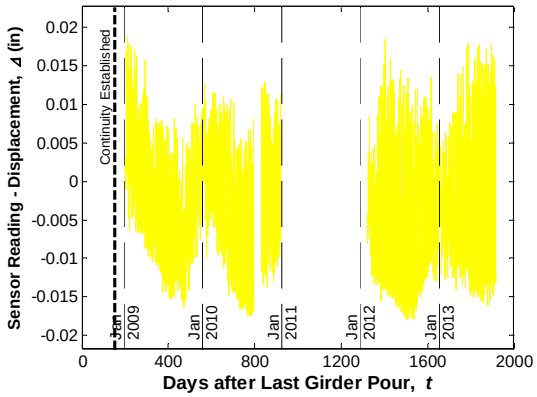

b) Sensor reading without temperature correction

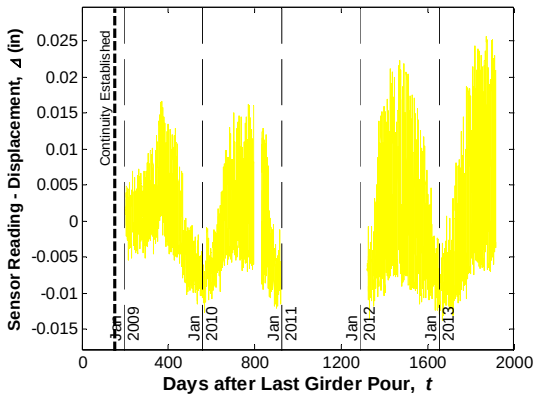

c) Sensor reading after temperature correction

Figure 35
Sensor No. 9, Location G1, End Connection (DM)

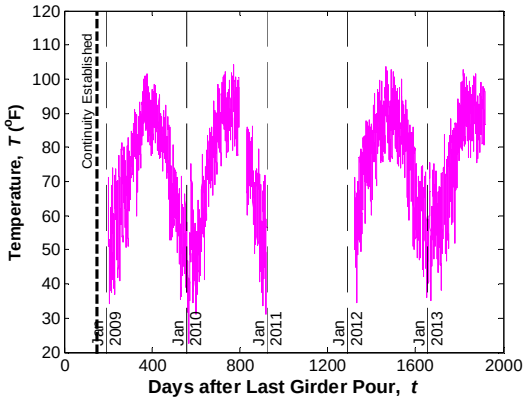

a) Temperature reading of the sensor

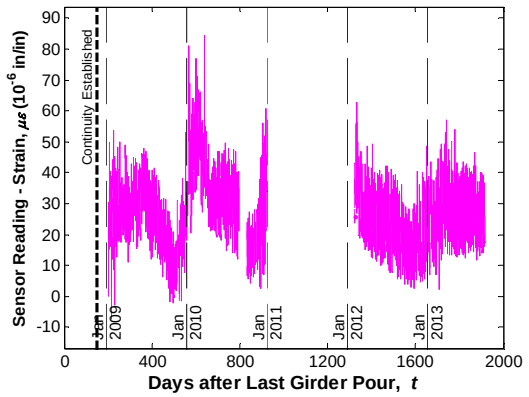

b) Sensor reading without temperature correction

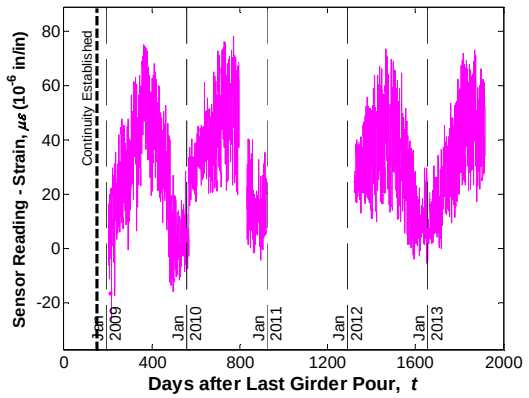

c) Sensor reading after temperature correction

Figure 36
Sensor No. 17, Location G1S24, Support Top (VW)

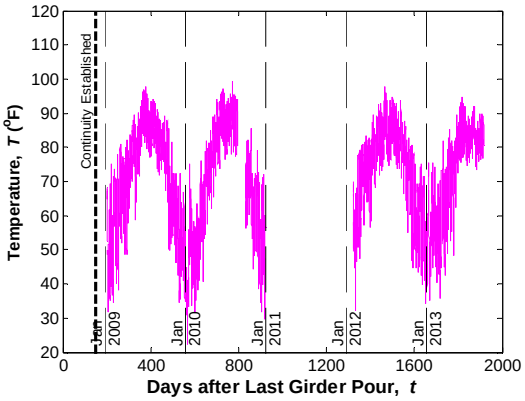

a) Temperature reading of the sensor

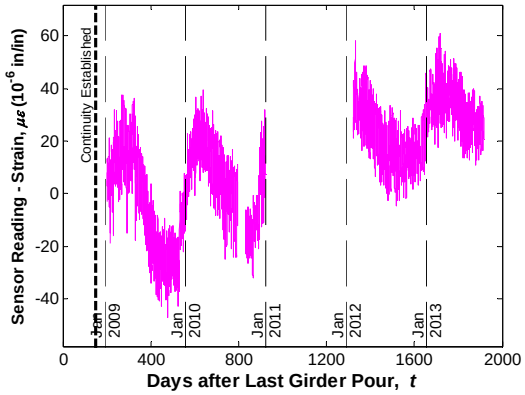

b) Sensor reading without temperature correction

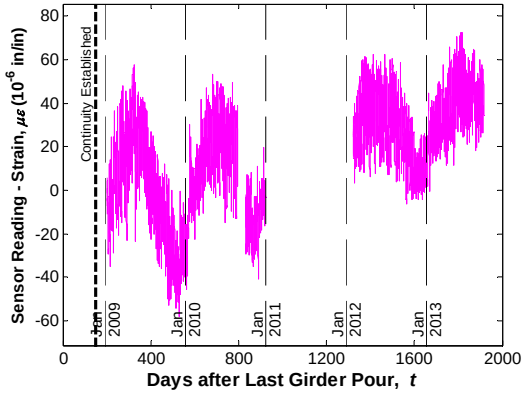

c) Sensor reading after temperature correction

Figure 37
Sensor No. 18, Location G1S24, Support Middle (Vibrating wire gauge)

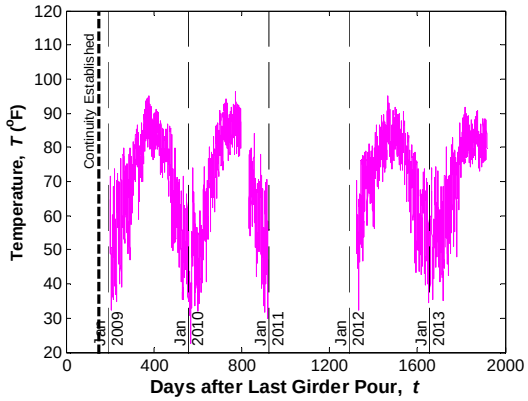

a) Temperature reading of the sensor

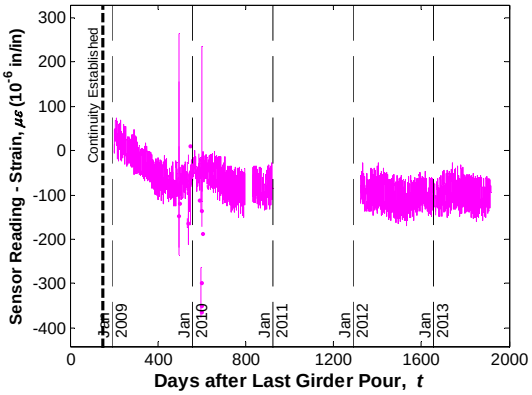

b) Sensor reading without temperature correction

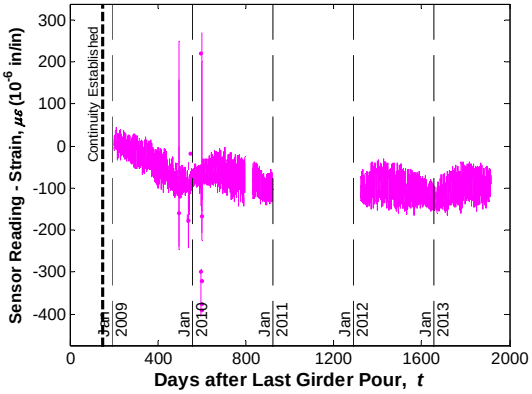

c) Sensor reading after temperature correction

Figure 38
Sensor No. 19, Location G1S24, Support Bottom (Vibrating wire gauge)

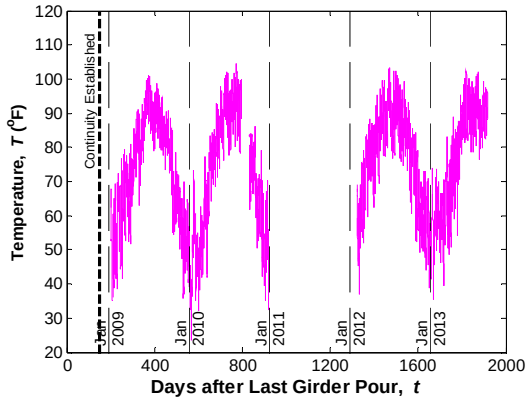

a) Temperature reading of the sensor

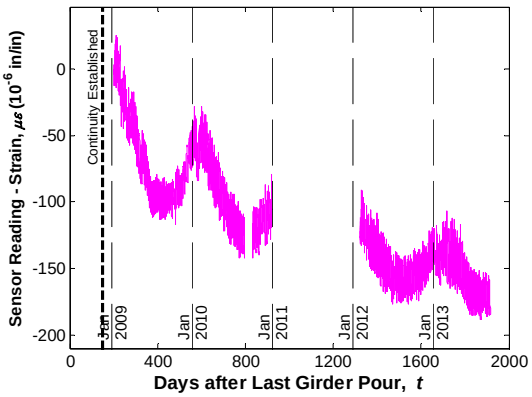

b) Sensor reading without temperature correction

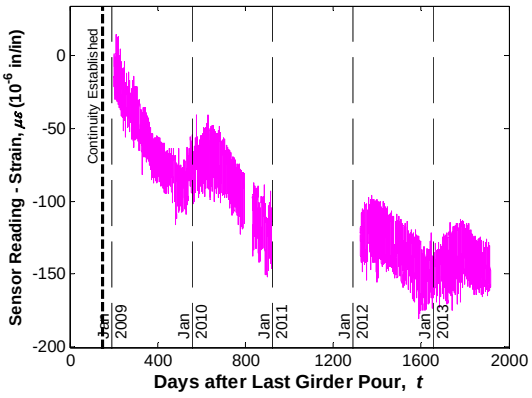

c) Sensor reading after temperature correction

Figure 39
Sensor No. 20, Location G1S23, Support Top (VW)

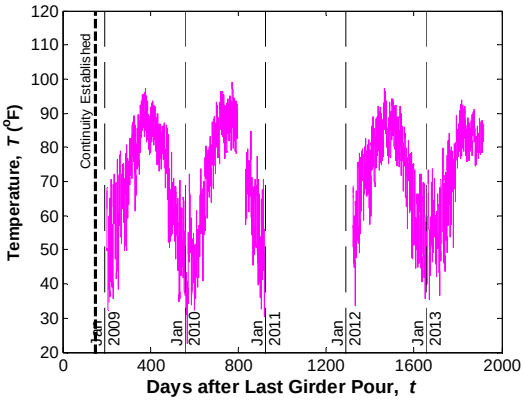

a) Temperature reading of the sensor

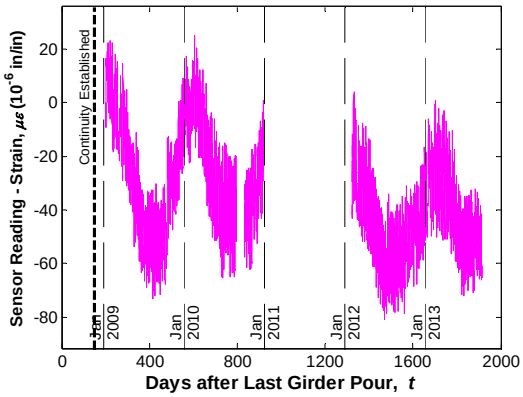

b) Sensor reading without temperature correction

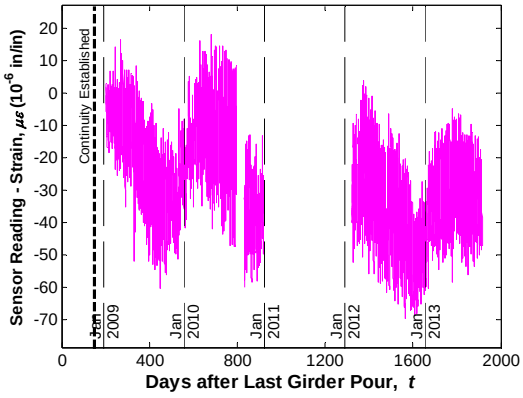

c) Sensor reading after temperature correction

Figure 40
Sensor No. 21, Location G1S23, Support Middle (VW)

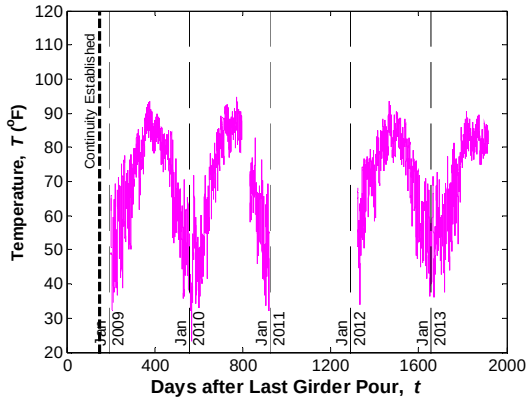

a) Temperature reading of the sensor

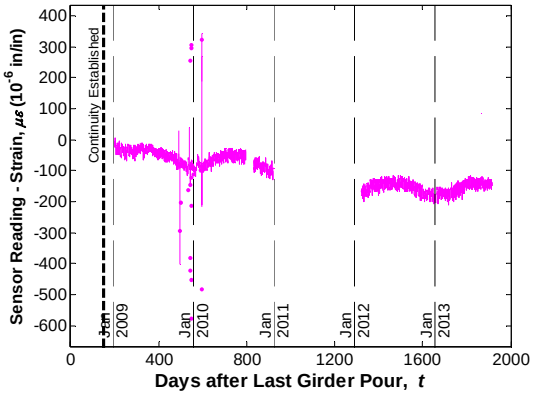

b) Sensor reading without temperature correction

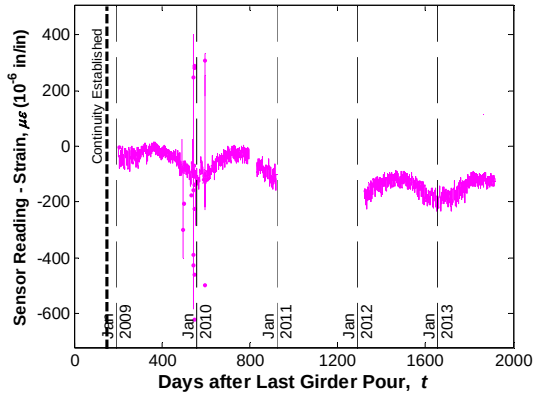

c) Sensor reading after temperature correction

Figure 41
Sensor No. 22, Location G1S23, Support Bottom (VW)

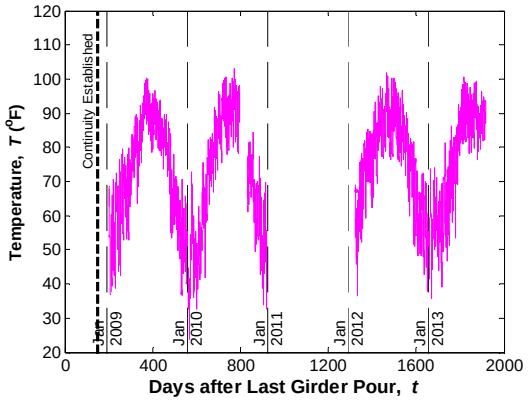

a) Temperature reading of the sensor

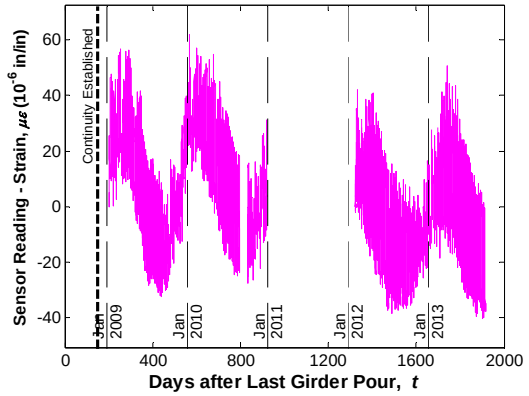

b) Sensor reading without temperature correction

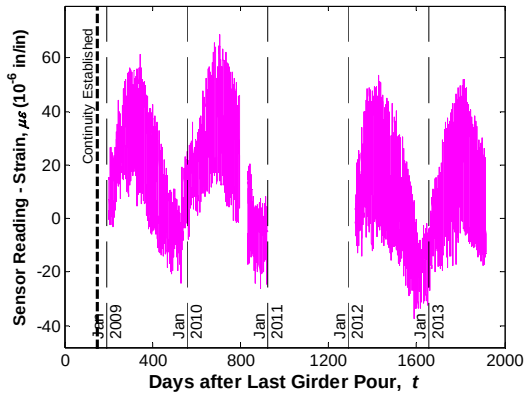

c) Sensor reading after temperature correction

Figure 42
Sensor No. 33, Location G5S24, Support Top (VW)

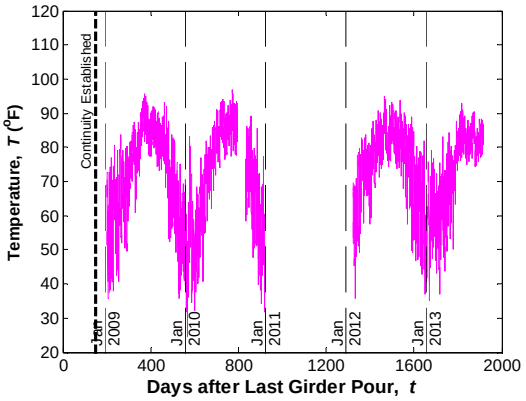

a) Temperature reading of the sensor

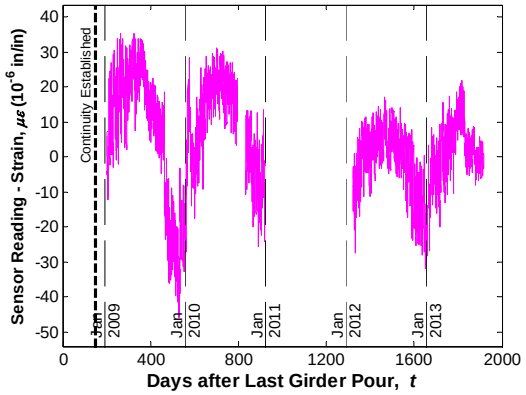

b) Sensor reading without temperature correction

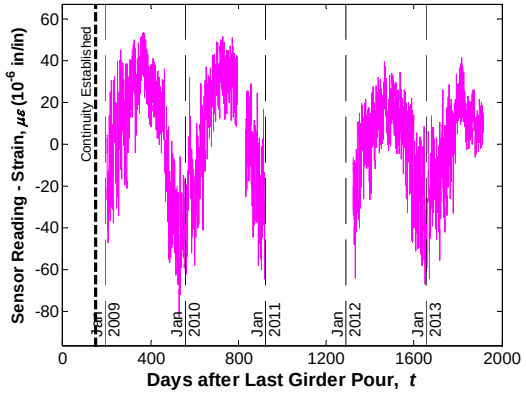

c) Sensor reading after temperature correction

Figure 43
Sensor No. 34, Location G5S24, Support Middle (VW)

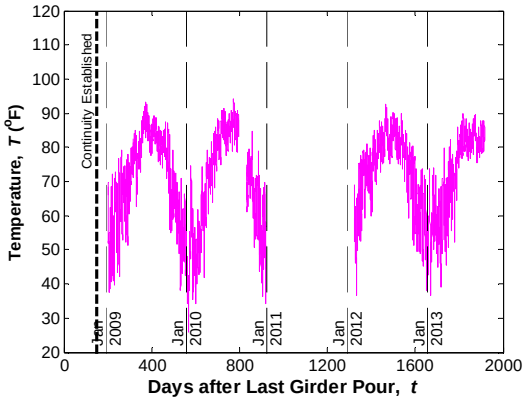

a) Temperature reading of the sensor

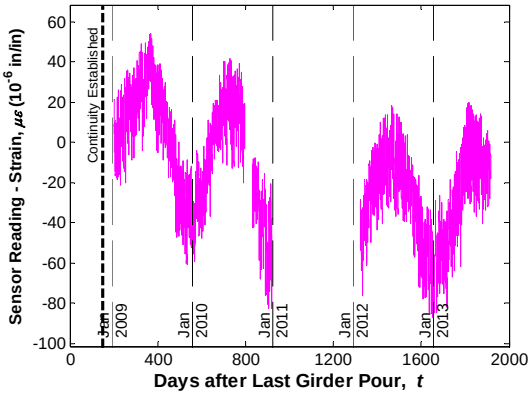

b) Sensor reading without temperature correction

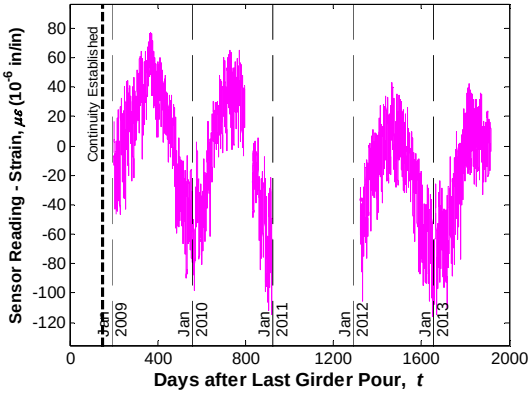

c) Sensor reading after temperature correction

Figure 44
Sensor No. 35, Location G5S24, Support Bottom (VW)

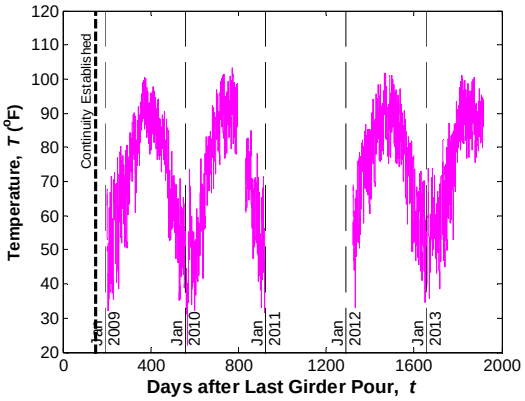

a) Temperature reading of the sensor

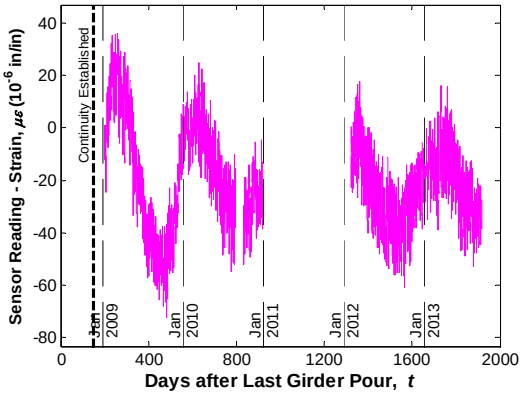

b) Sensor reading without temperature correction

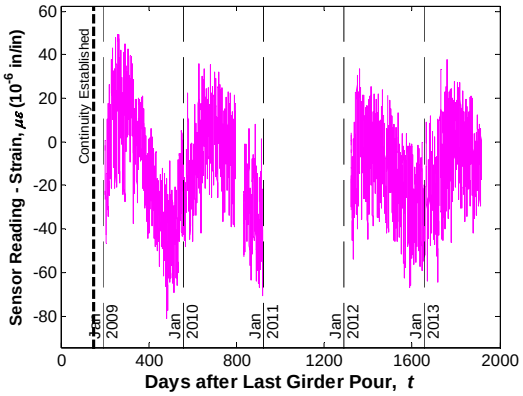

c) Sensor reading after temperature correction

Figure 45
Sensor No. 36, Location G5S23, Support Top (VW)

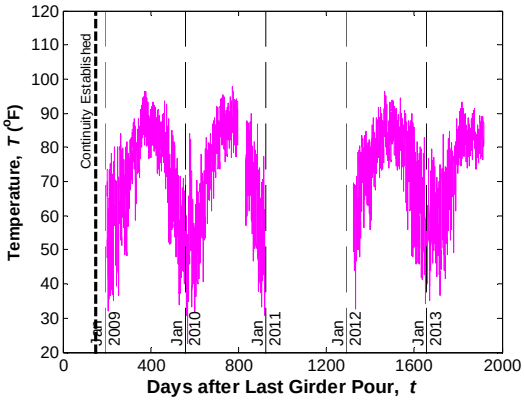

a) Temperature reading of the sensor

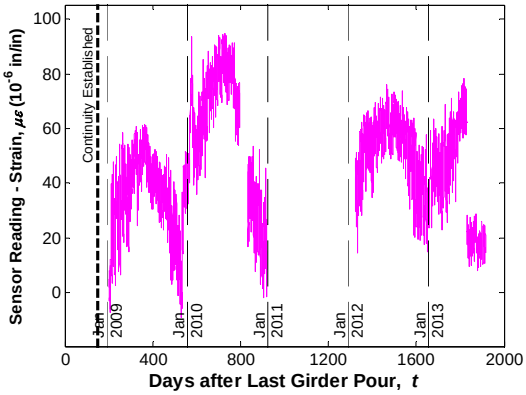

b) Sensor reading without temperature correction

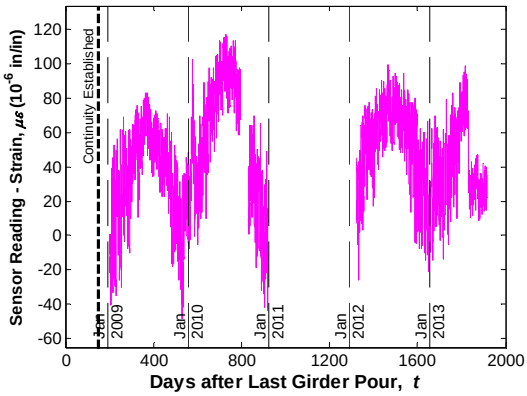

c) Sensor reading after temperature correction

Figure 46
Sensor No. 37, Location G5S23, Support Middle (VW)

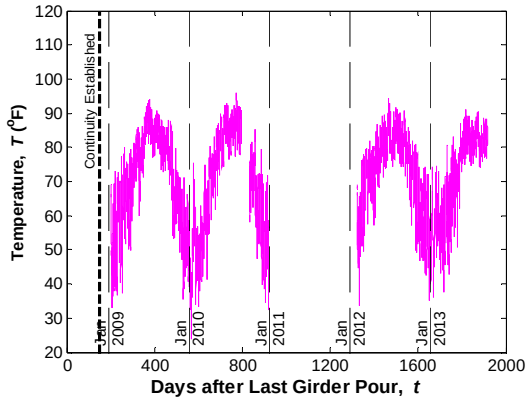

a) Temperature reading of the sensor

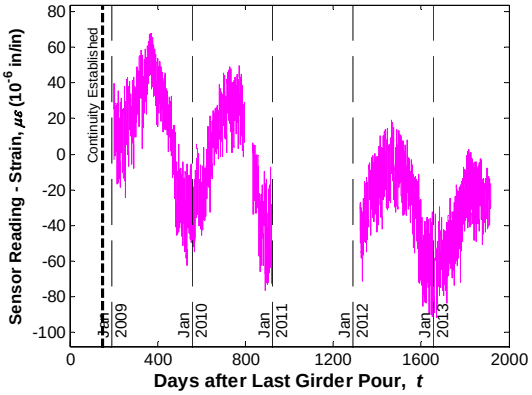

b) Sensor reading without temperature correction

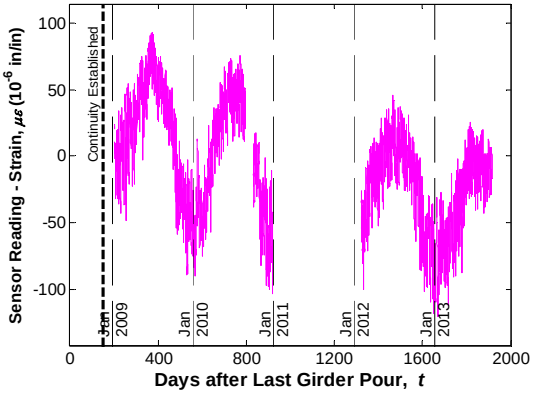

c) Sensor reading after temperature correction

Figure 47
Sensor No. 38, Location G5S23, Support Bottom (VW)

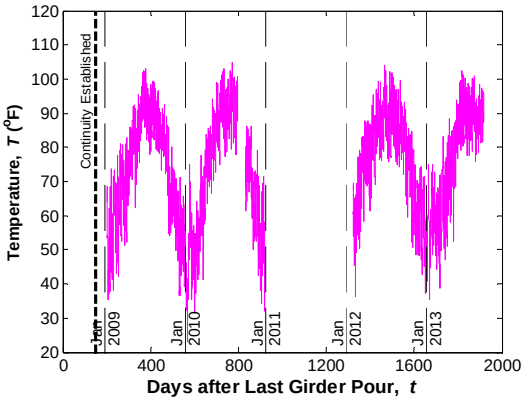

a) Temperature reading of the sensor

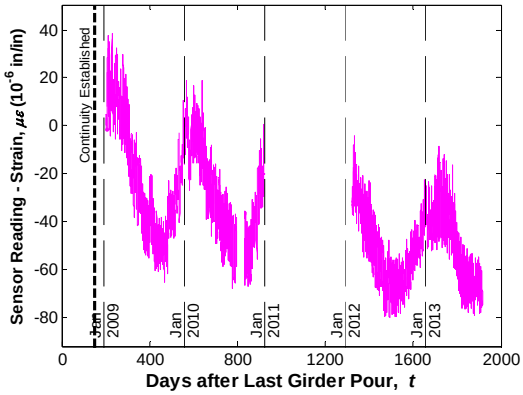

b) Sensor reading without temperature correction

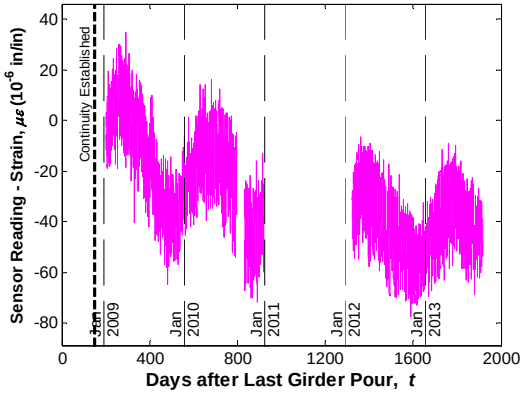

c) Sensor reading after temperature correction

Figure 48
Sensor No. 39, Location G3S24, Support Top (VW)

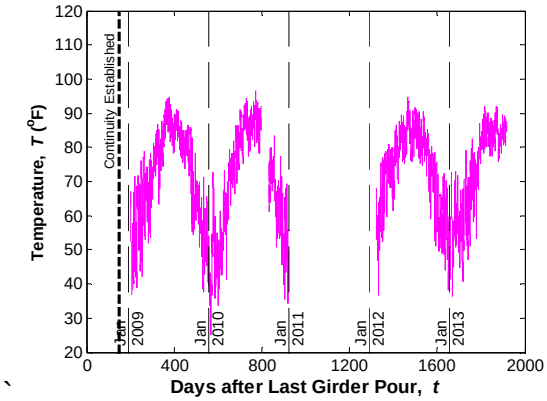

a) Temperature reading of the sensor

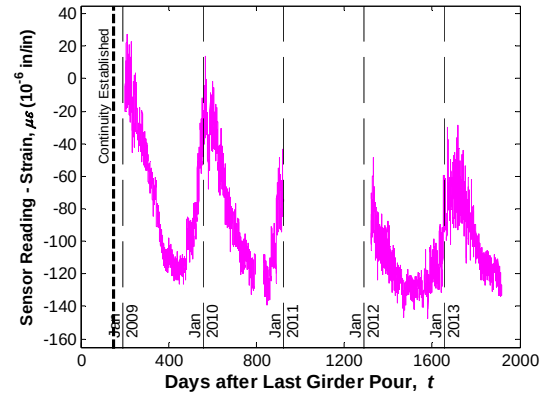

b) Sensor reading without temperature correction

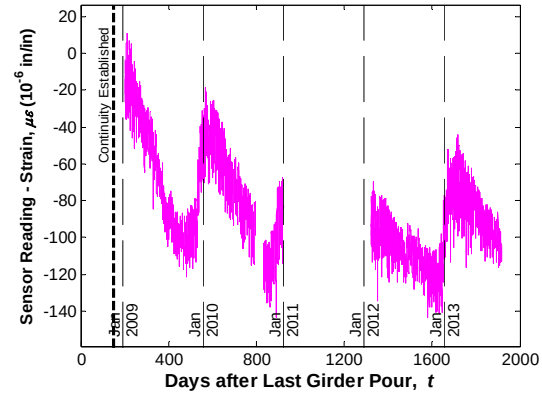

c) Sensor reading after temperature correction

Figure 49
Sensor No. 40, Location G3S24, Support Middle (VW)

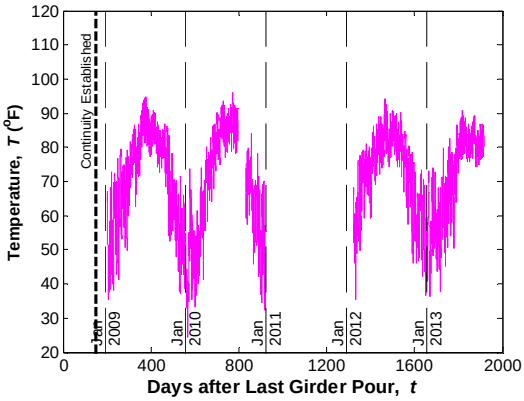

a) Temperature reading of the sensor

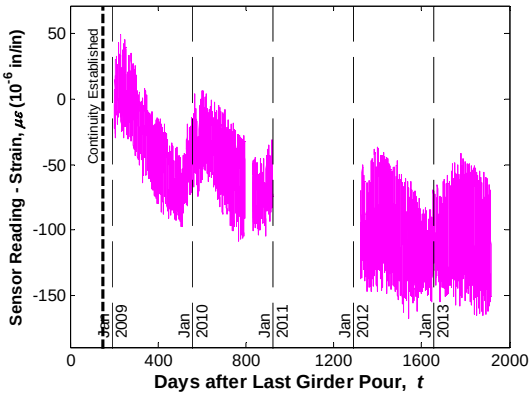

b) Sensor reading without temperature correction

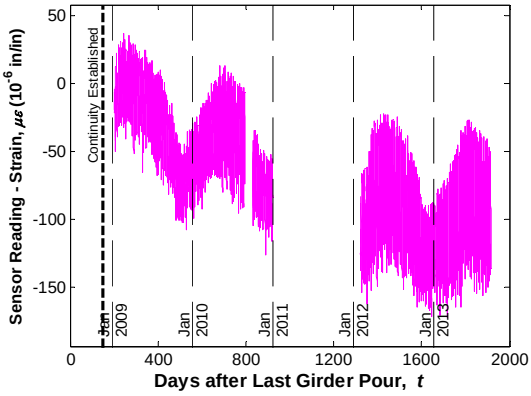

c) Sensor reading after temperature correction

Figure 50
Sensor No. 41, Location G3S24, Support Bottom (VW)

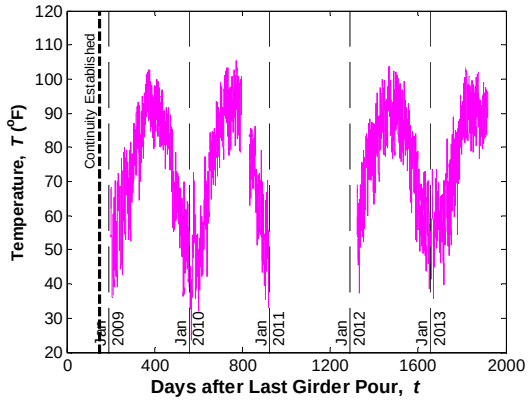

a) Temperature reading of the sensor

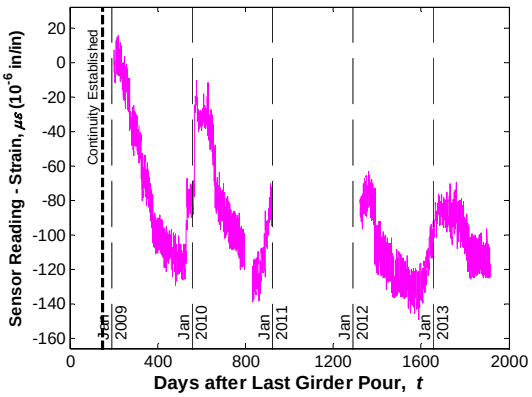

b) Sensor reading without temperature correction

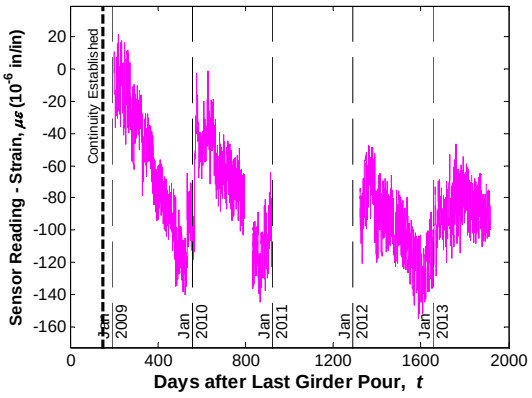

c) Sensor reading after temperature correction

Figure 51
Sensor No. 42, Location G3S23, Support Top (VW)

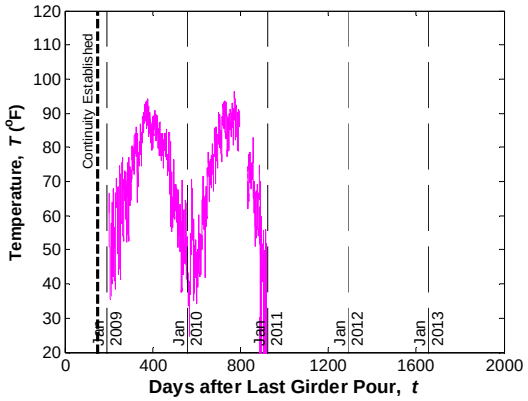

a) Temperature reading of the sensor

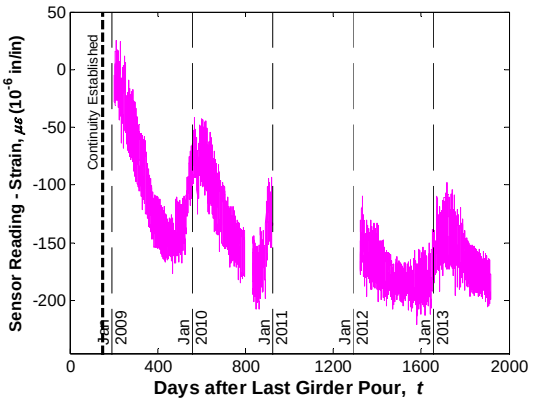

b) Sensor reading without temperature correction

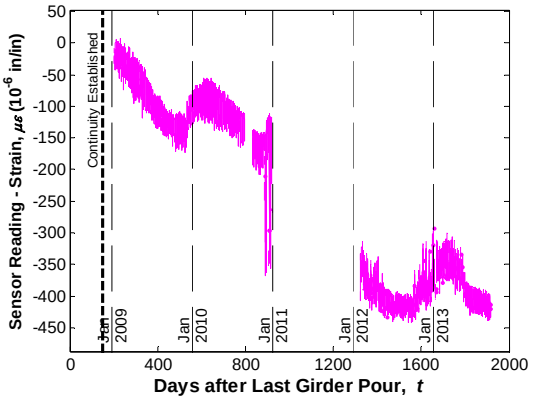

c) Sensor reading after temperature correction

Figure 52
Sensor No. 43, Location G3S23, Support Middle (VW)

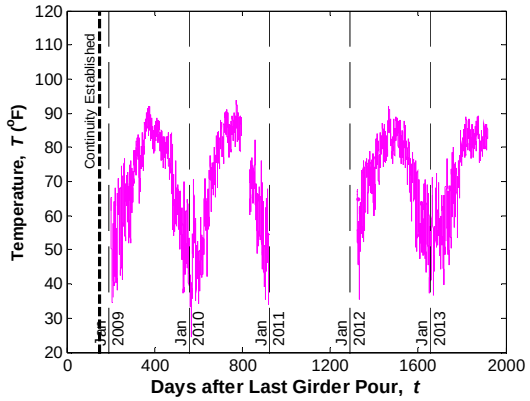

a) Temperature reading of the sensor

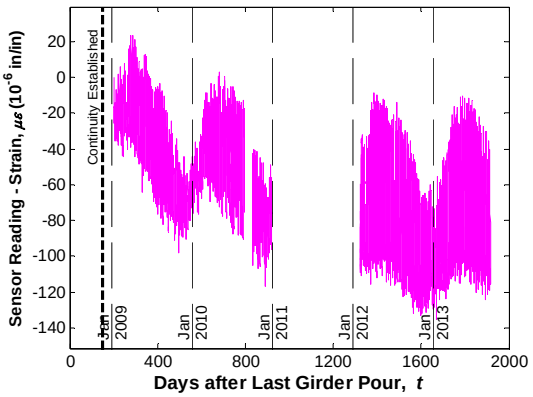

b) Sensor reading without temperature correction

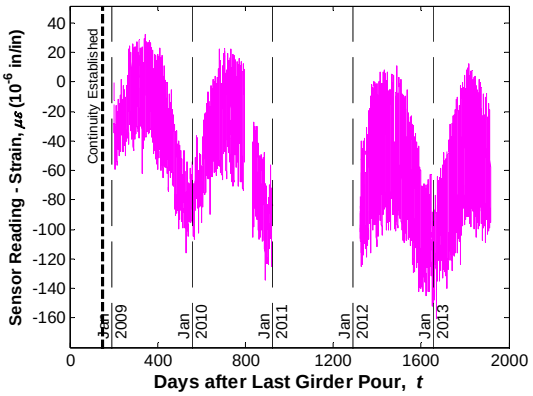

c) Sensor reading after temperature correction

Figure 53
Sensor No. 44, Location G3S23, Support Bottom (VW)

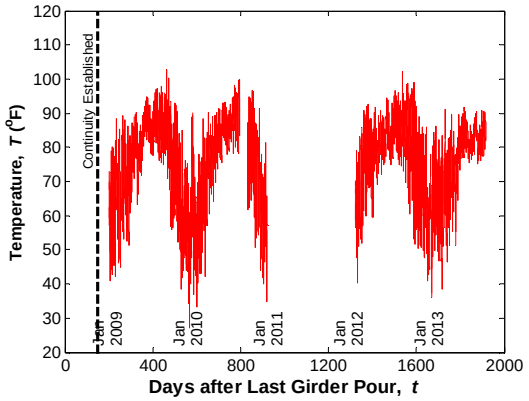

a) Temperature reading of the sensor

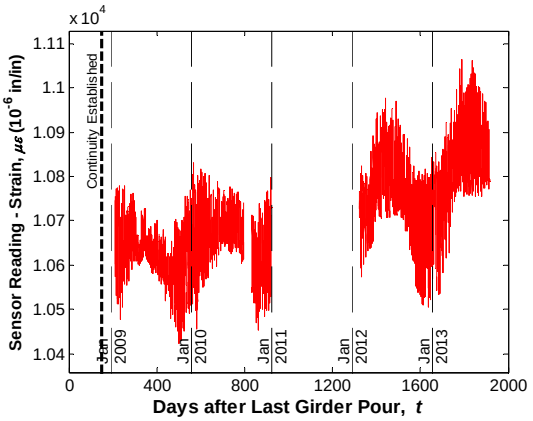

b) Sensor reading without temperature correction

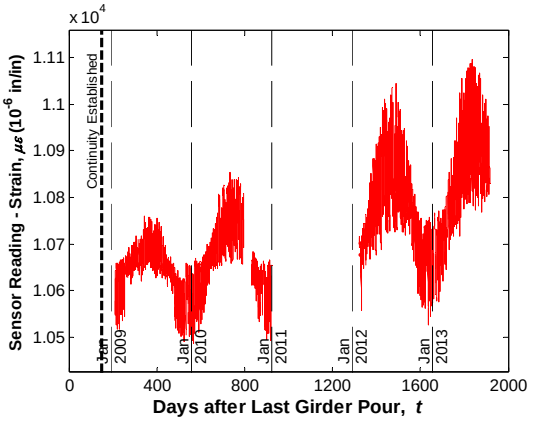

c) Sensor reading after temperature correction

Figure 54
Sensor No. 45, Location G5S24, Support Bottom (ES)

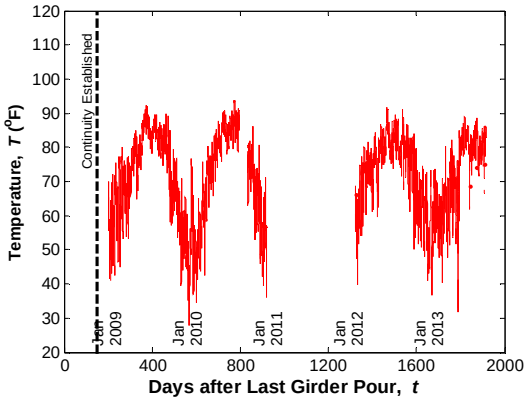

a) Temperature reading of the sensor

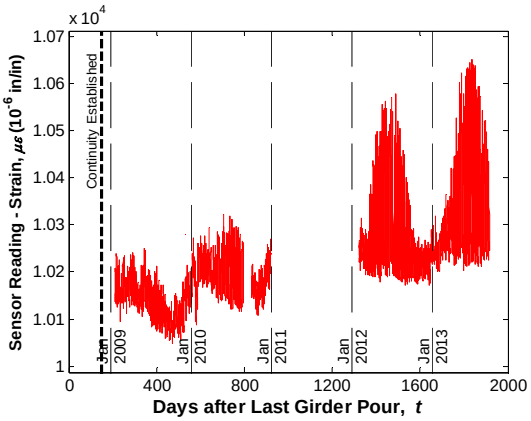

b) Sensor reading without temperature correction

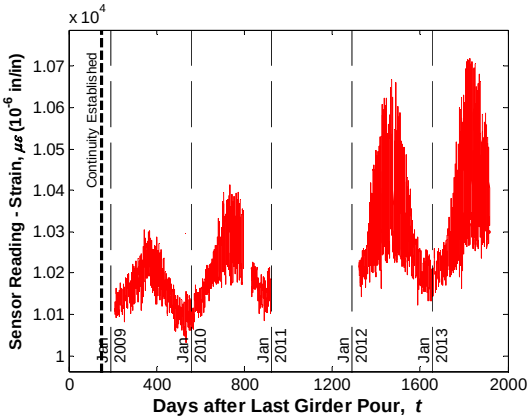

c) Sensor reading after temperature correction

Figure 55
Sensor No. 46, Location G5S24, Support Bottom (ES)

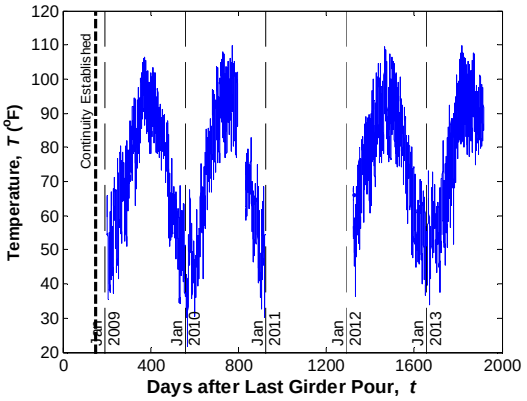

a) Temperature reading of the sensor

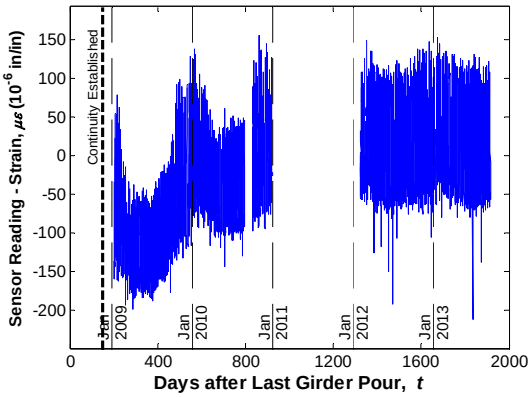

b) Sensor reading without temperature correction

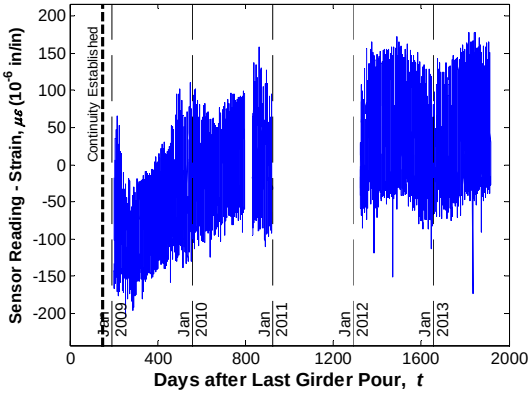

c) Sensor reading after temperature correction

Figure 56
Sensor No. 47, Location G5S24, Support Top (EC)

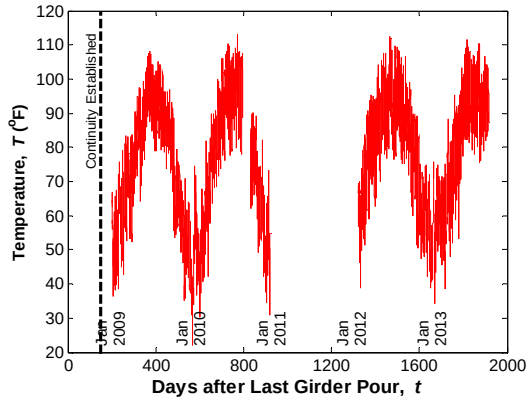

a) Temperature reading of the sensor

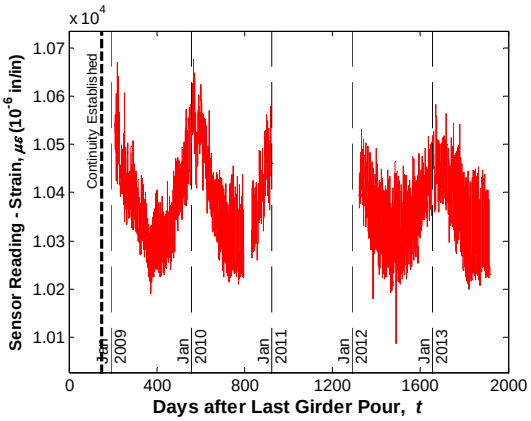

b) Sensor reading without temperature correction

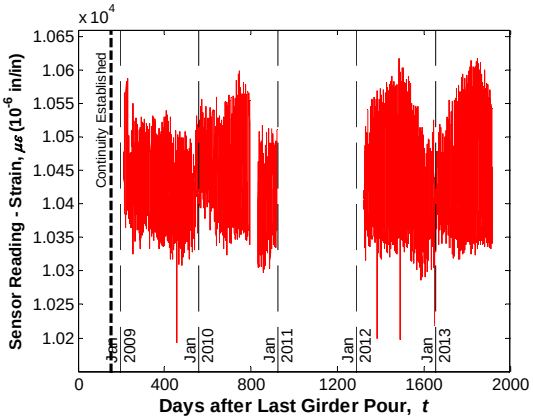

c) Sensor reading after temperature correction

Figure 57
Sensor No. 48, Location G4S24, Support Top (ES)

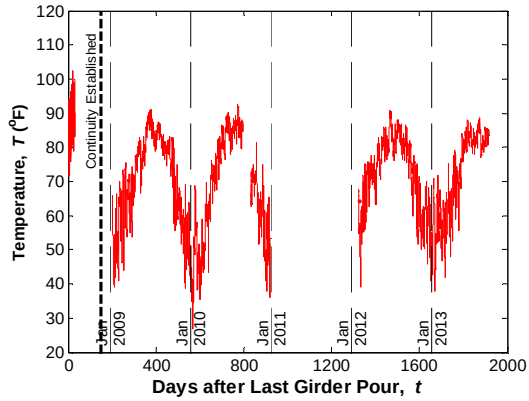

a) Temperature reading of the sensor

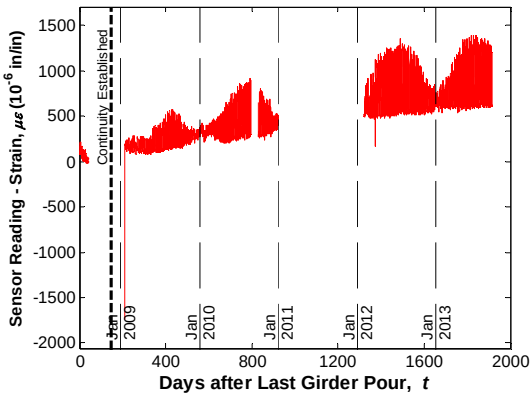

b) Sensor reading without temperature correction

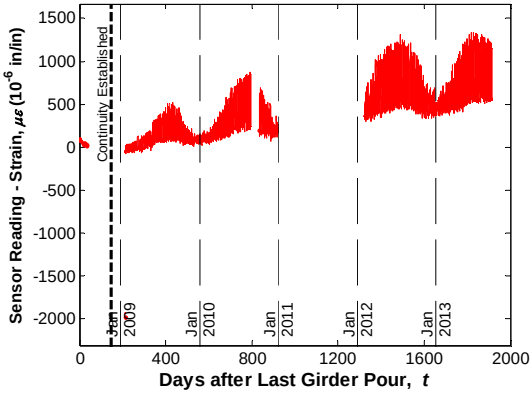

c) Sensor reading after temperature correction

Figure 58
Sensor No. 49, Location G3S24, Support Bottom (ES)

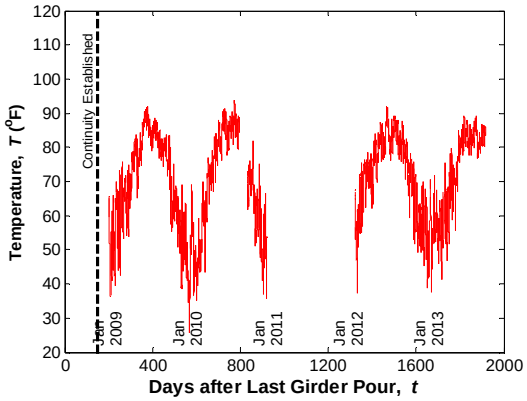

a) Temperature reading of the sensor

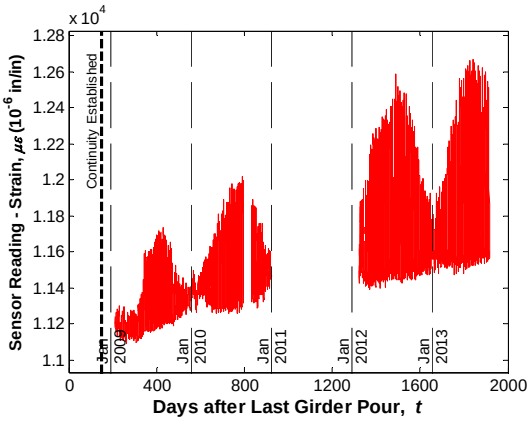

b) Sensor reading without temperature correction

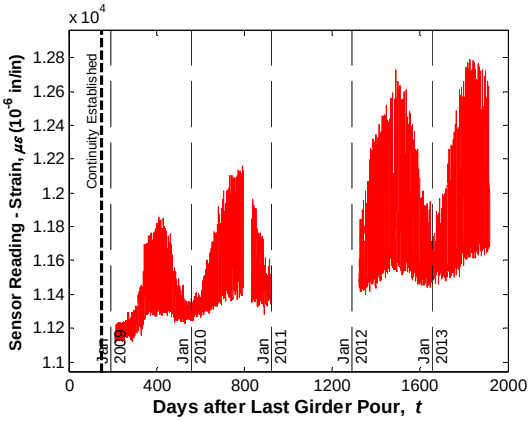

c) Sensor reading after temperature correction

Figure 59
Sensor No. 50, Location G3S23, Support Bottom (ES)

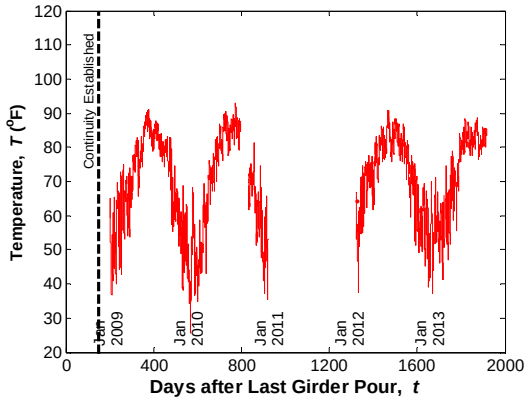

a) Temperature reading of the sensor

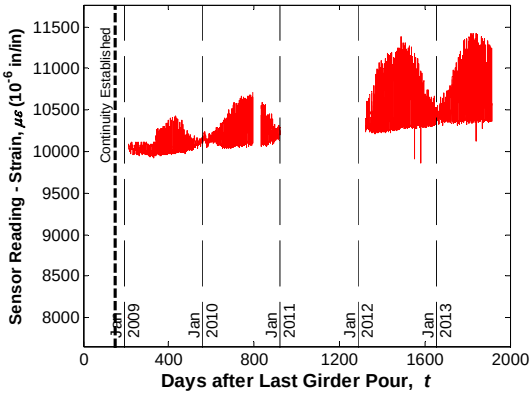

b) Sensor reading without temperature correction

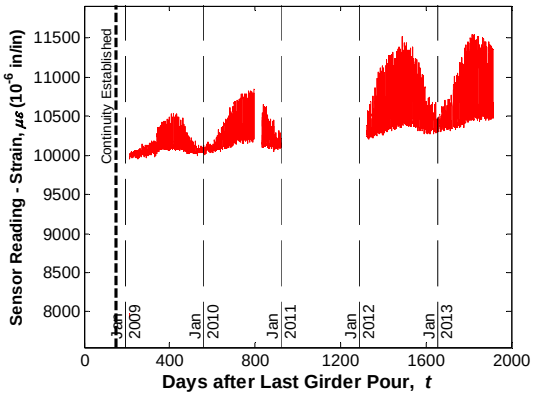

c) Sensor reading after temperature correction

Figure 60
Sensor No. 51, Location G3S23, Support Bottom (ES)

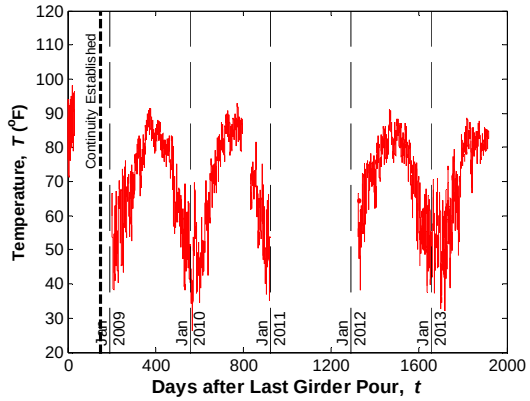

a) Temperature reading of the sensor

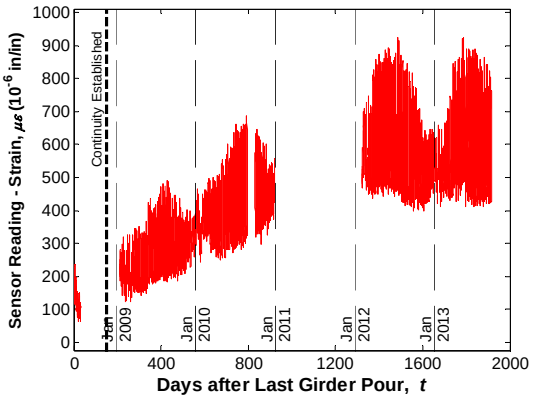

b) Sensor reading without temperature correction

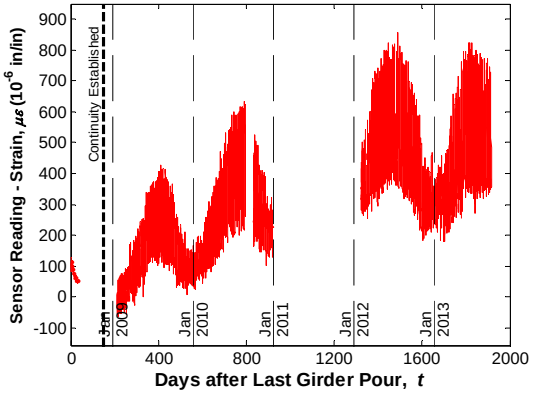

c) Sensor reading after temperature correction

Figure 61
Sensor No. 52, Location G3S24, Support Bottom (ES)

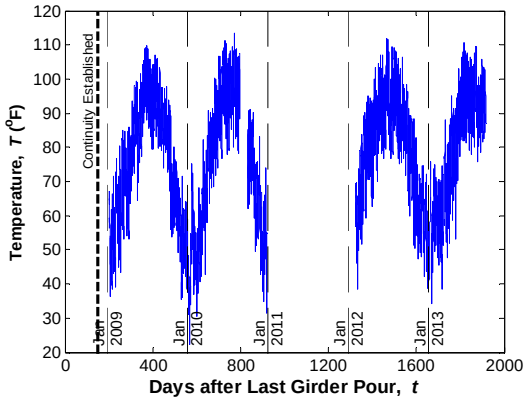

a) Temperature reading of the sensor

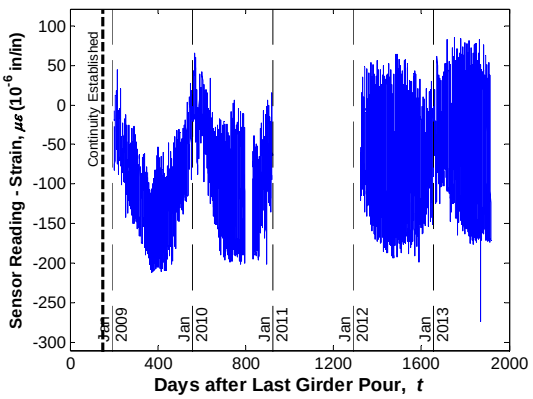

b) Sensor reading without temperature correction

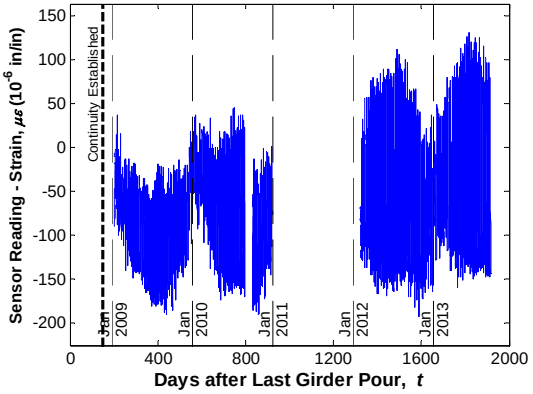

c) Sensor reading after temperature correction

Figure 62
Sensor No. 53, Location G3S24, Support Top (EC)

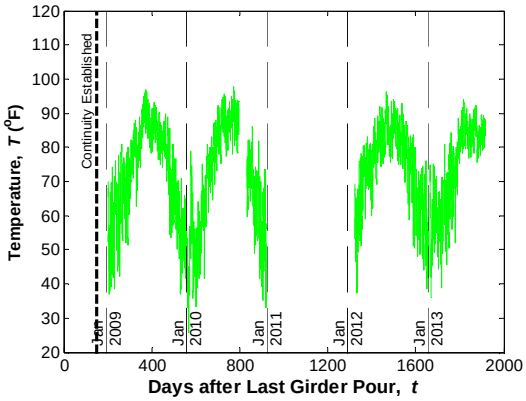

a) Temperature reading of the sensor

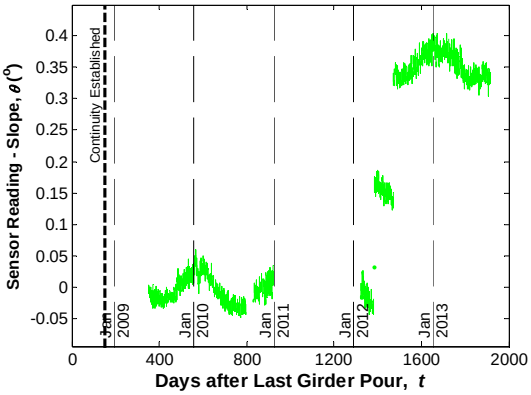

b) Sensor reading without temperature correction

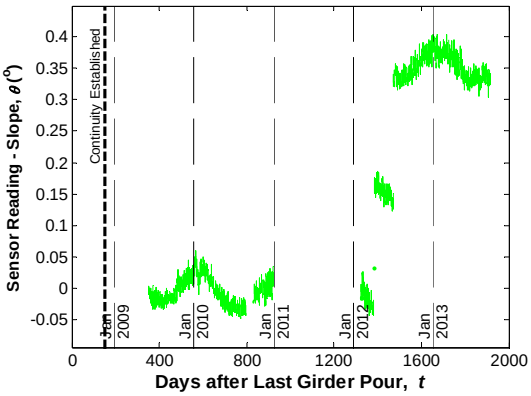

c) Sensor reading after temperature correction

Figure 63
Sensor No. 54, Location G5S24, Support (TM)

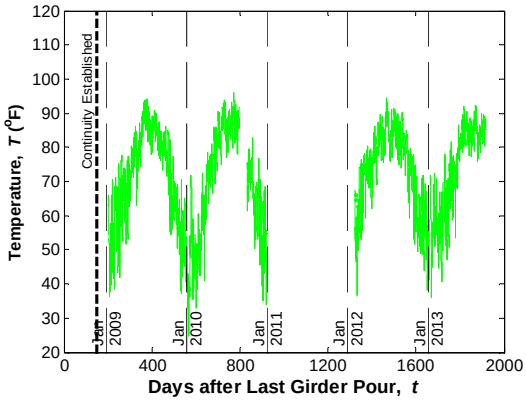

a) Temperature reading of the sensor

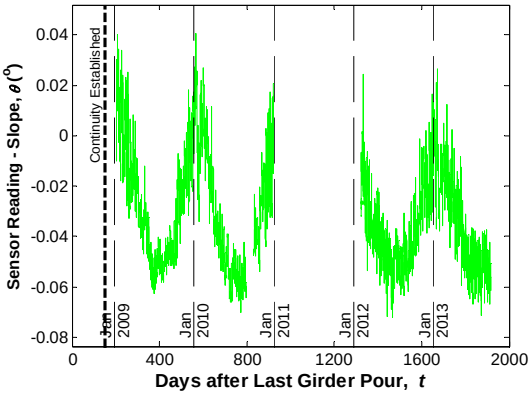

b) Sensor reading without temperature correction

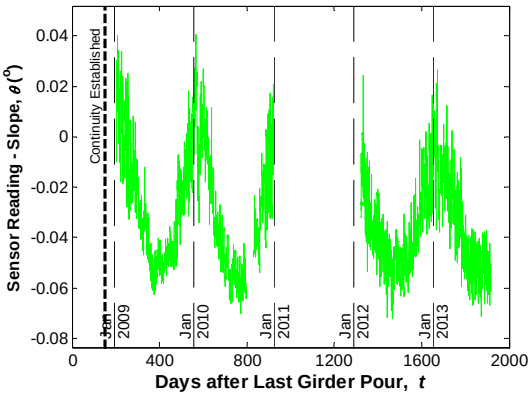

c) Sensor reading after temperature correction

Figure 64
Sensor No. 55, Location G3S24, Support (TM)

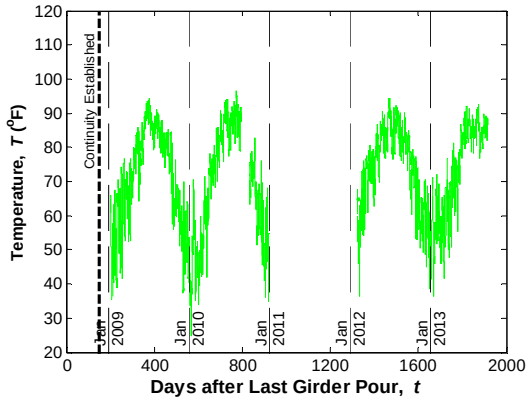

a) Temperature reading of the sensor

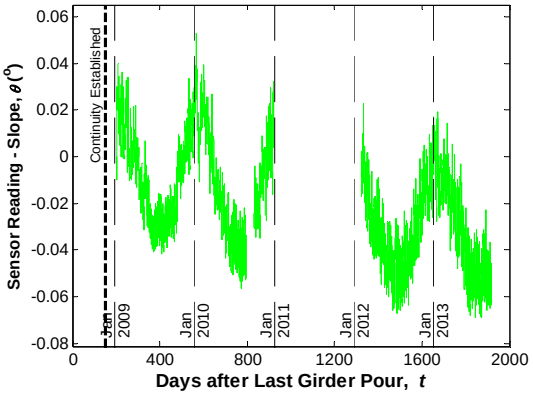

b) Sensor reading without temperature correction

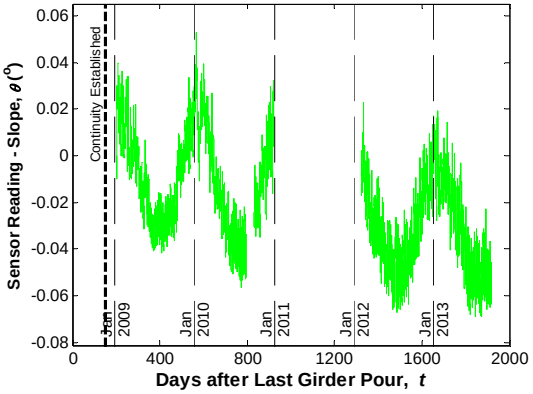

c) Sensor reading after temperature correction

Figure 65
Sensor No. 56, Location G3S23, Support (TM)

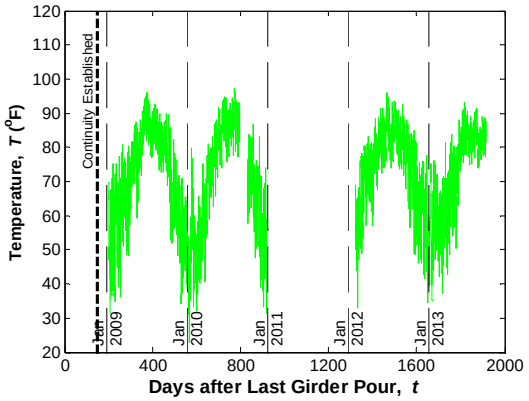

a) Temperature reading of the sensor

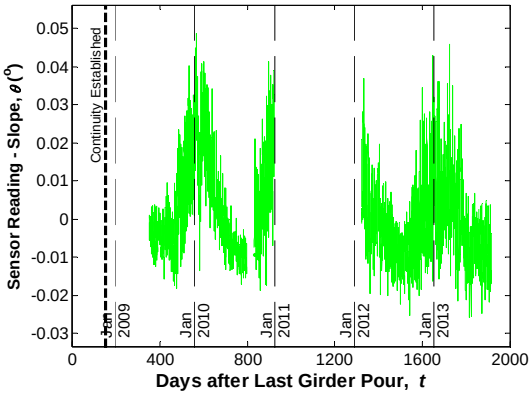

b) Sensor reading without temperature correction

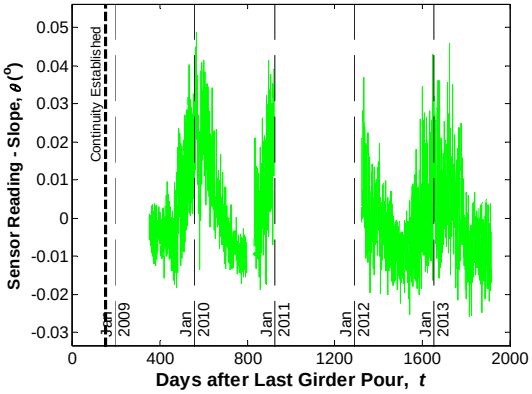

c) Sensor reading after temperature correction

Figure 66
Sensor No. 57, Location G5S23, Support (TM)

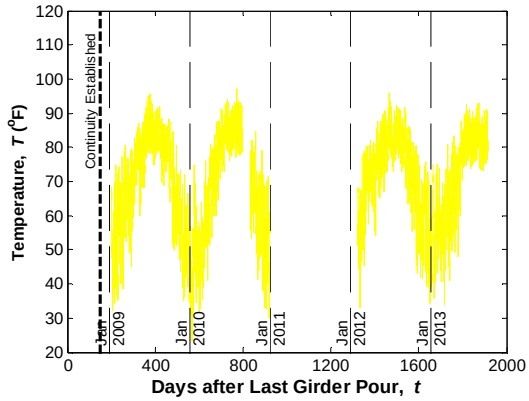

a) Temperature reading of the sensor

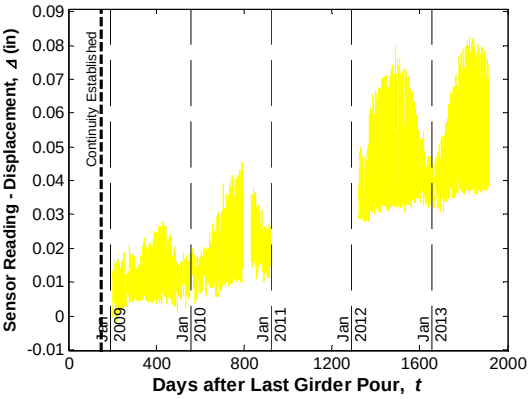

b) Sensor reading without temperature correction

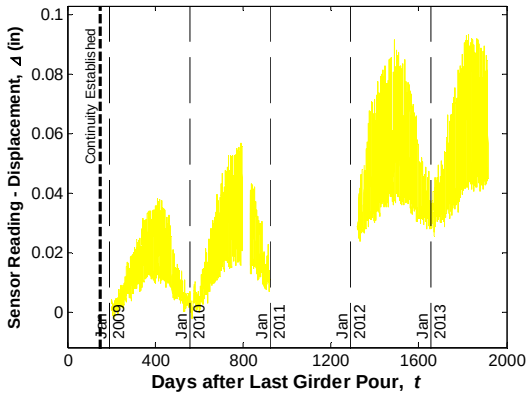

c) Sensor reading after temperature correction

Figure 67
Sensor No. 58, Location G3, End Connection (DM)

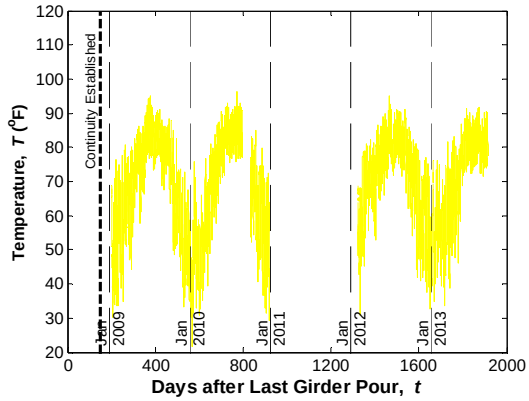

a) Temperature reading of the sensor

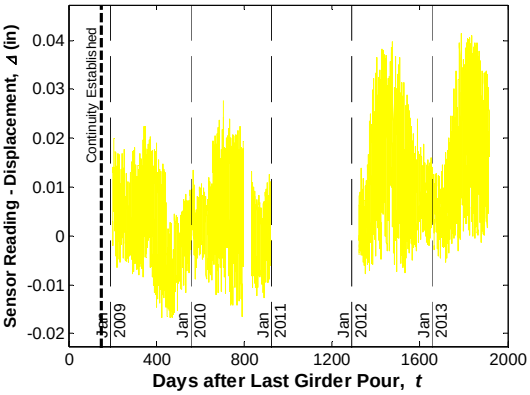

b) Sensor reading without temperature correction

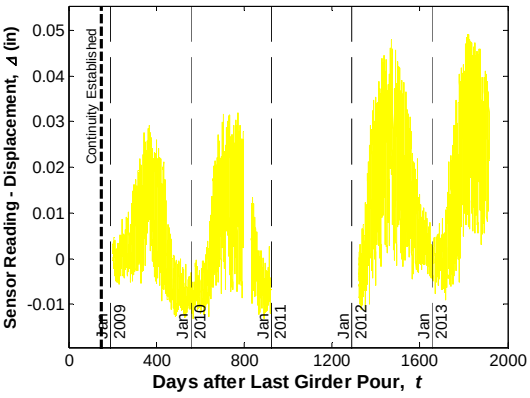

c) Sensor reading after temperature correction

Figure 68
Sensor No. 59, Location G5, End Connection (DM)

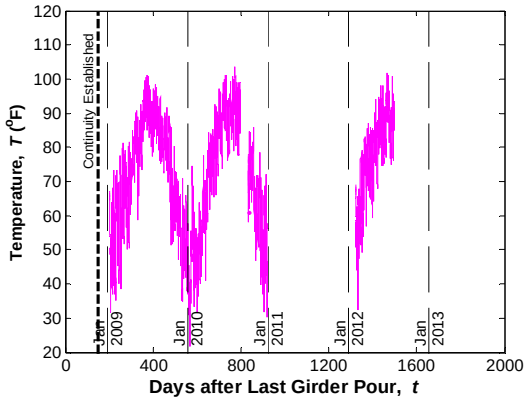

a) Temperature reading of the sensor

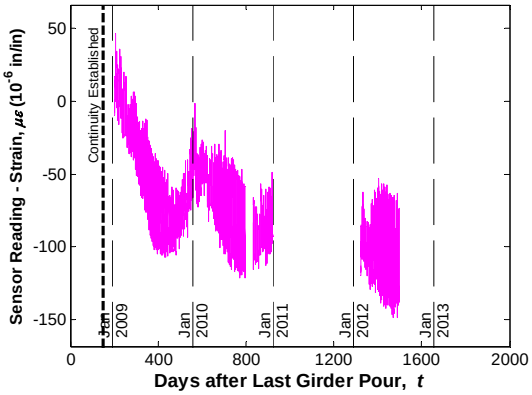

b) Sensor reading without temperature correction

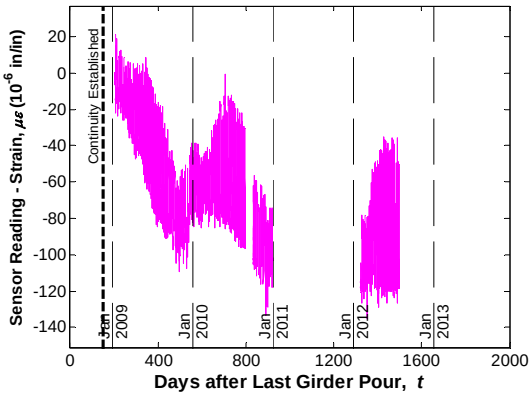

c) Sensor reading after temperature correction

Figure 69
Sensor No. 65, Location G5S24, Midspan Top (VW)

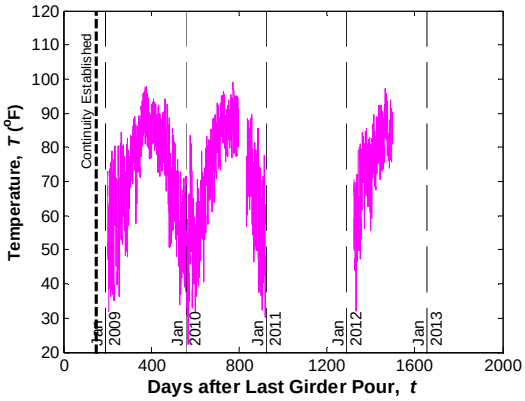

a) Temperature reading of the sensor

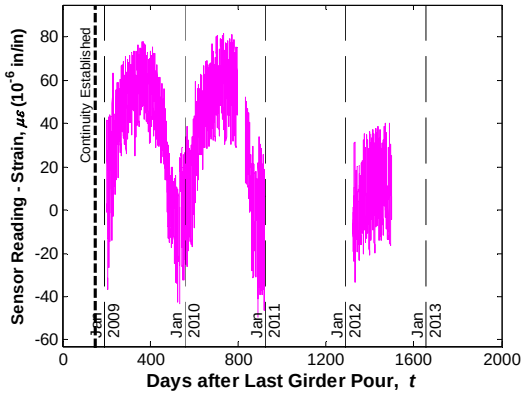

b) Sensor reading without temperature correction

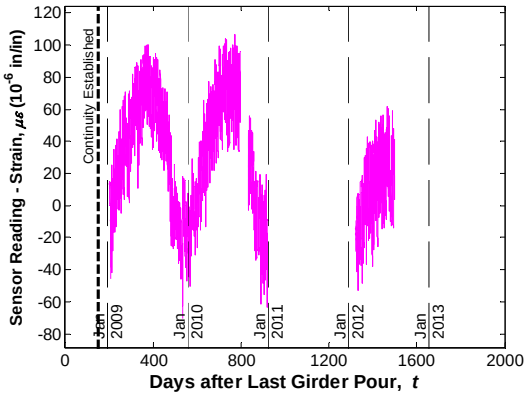

c) Sensor reading after temperature correction

Figure 70
Sensor No. 66, Location G5S24, Midspan Middle (VW)

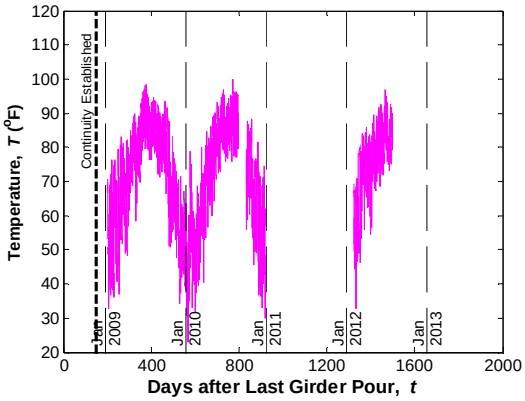

a) Temperature reading of the sensor

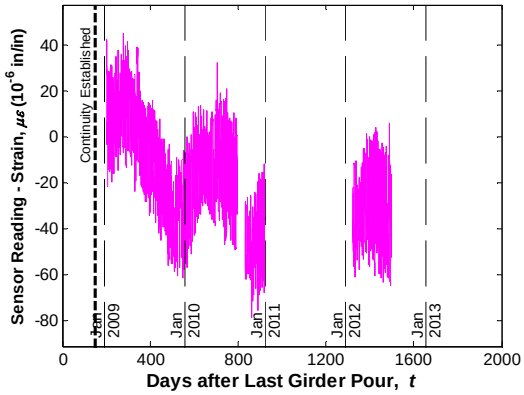

b) Sensor reading without temperature correction

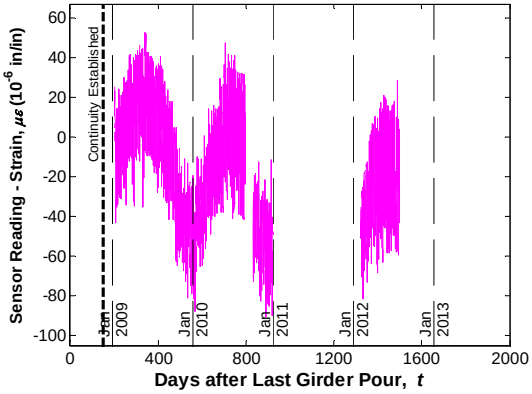

c) Sensor reading after temperature correction

Figure 71
Sensor No. 67, Location G5S24, Midspan Bottom (VW)

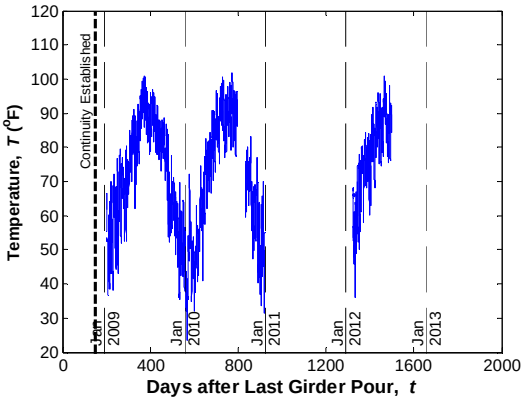

a) Temperature reading of the sensor

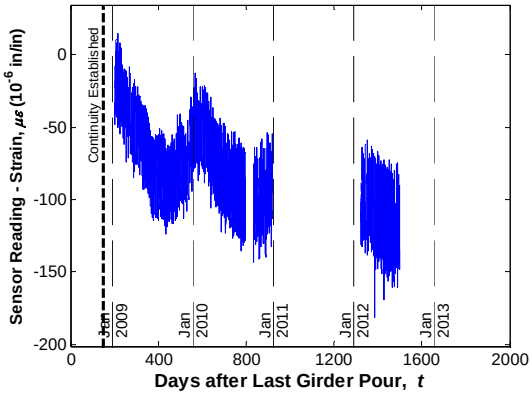

b) Sensor reading without temperature correction

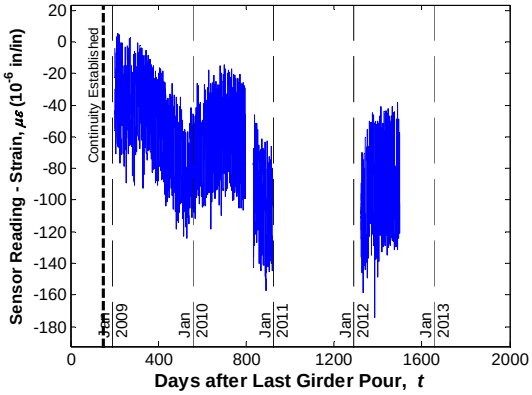

c) Sensor reading after temperature correction

Figure 72
Sensor No. 68, Location G5S24, Midspan Top (EC)

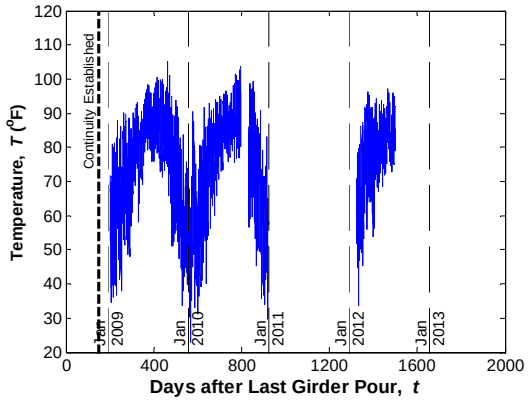

a) Temperature reading of the sensor

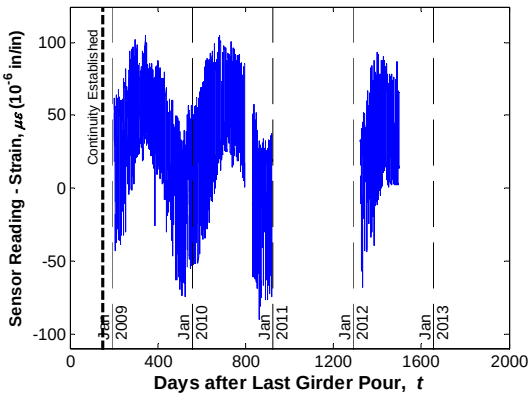

b) Sensor reading without temperature correction

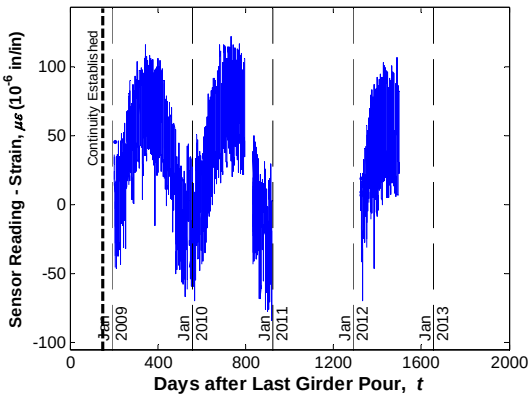

c) Sensor reading after temperature correction

Figure 73
Sensor No. 69, Location G5S24, Midspan Bottom (EC)

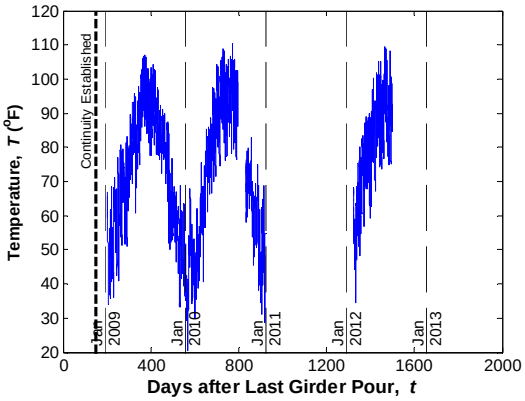

a) Temperature reading of the sensor

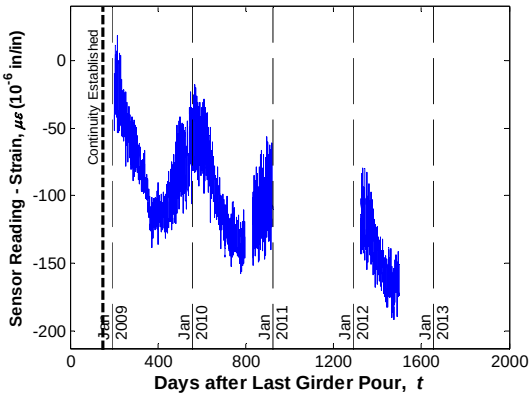

b) Sensor reading without temperature correction

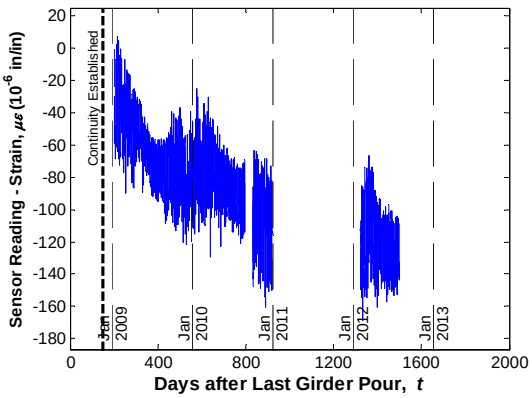

c) Sensor reading after temperature correction

Figure 74
Sensor No. 70, Location G5S24, Midspan Deck (EC)

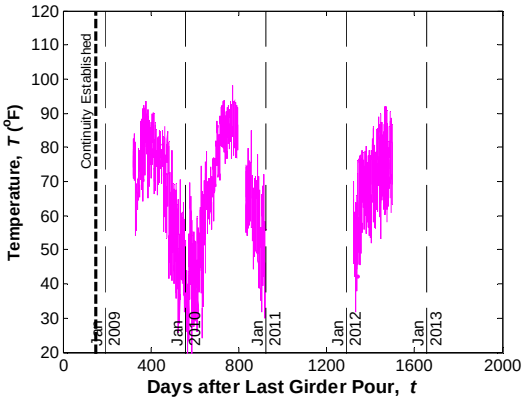

a) Temperature reading of the sensor

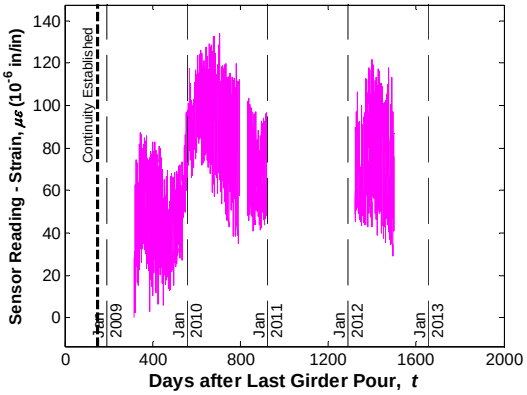

b) Sensor reading without temperature correction

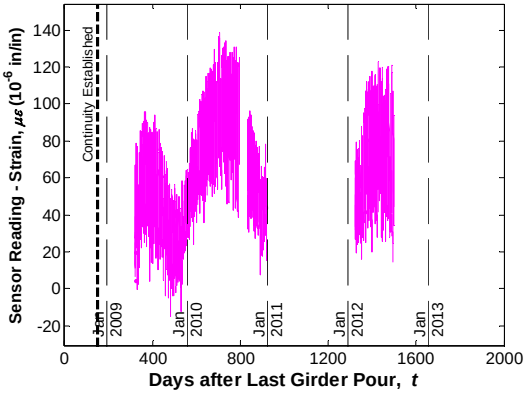

c) Sensor reading after temperature correction

Figure 75
Sensor No. 71, Location G2S24, Midspan Bottom (VW)

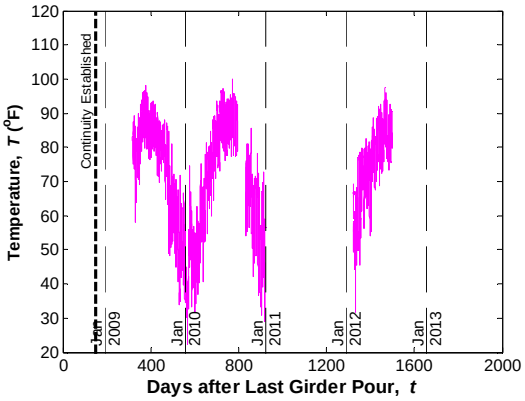

a) Temperature reading of the sensor

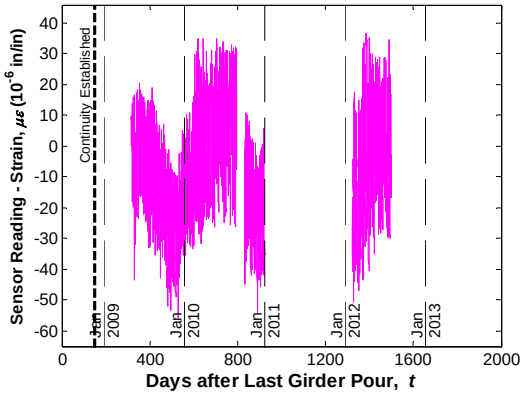

b) Sensor reading without temperature correction

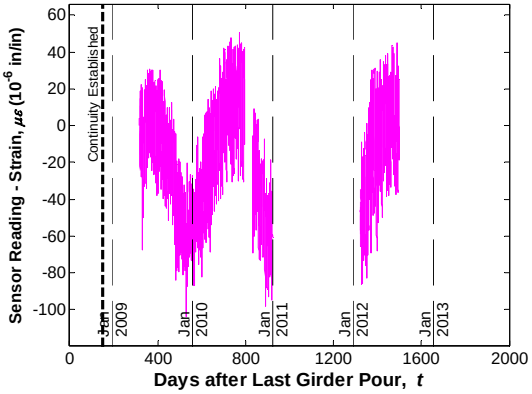

c) Sensor reading after temperature correction

Figure 76
Sensor No. 72, Location G1S24, Midspan Bottom (VW)

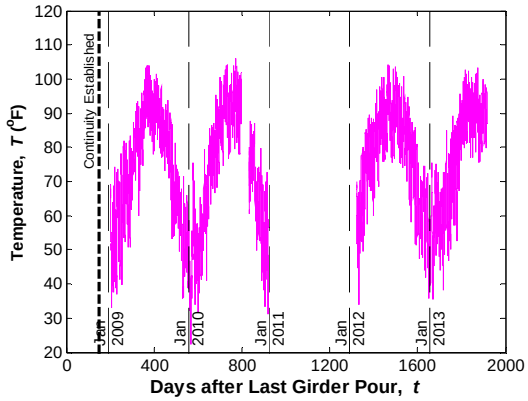

a) Temperature reading of the sensor

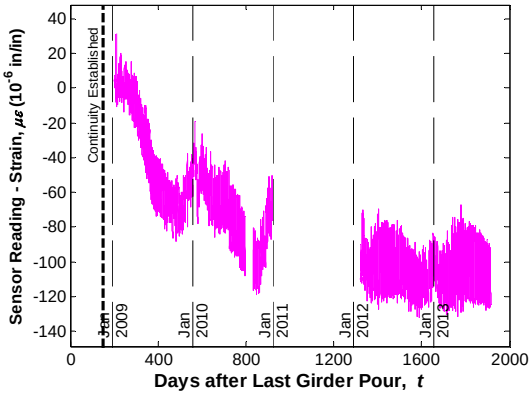

b) Sensor reading without temperature correction

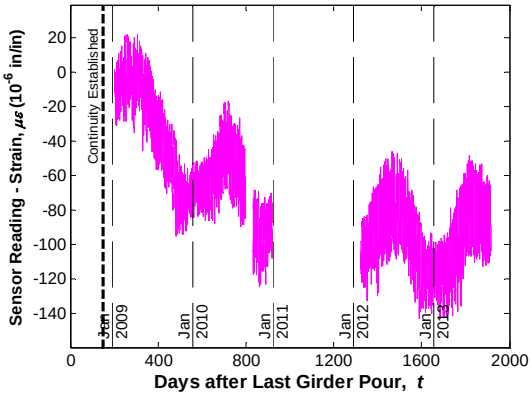

c) Sensor reading after temperature correction

Figure 77
Sensor No. 81, Location G3S24, Midspan Top (VW)

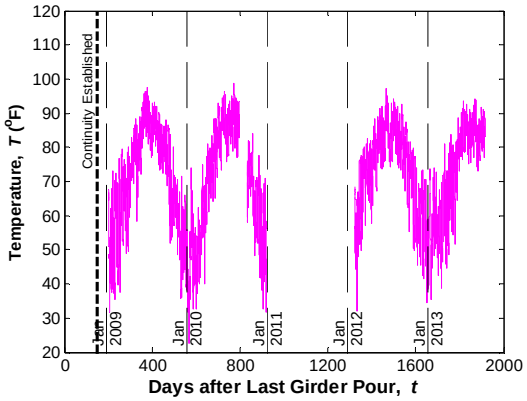

a) Temperature reading of the sensor

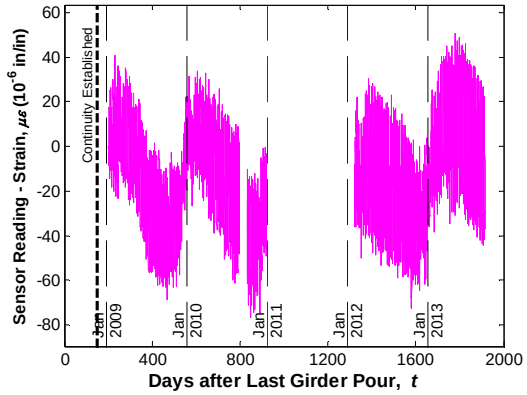

b) Sensor reading without temperature correction

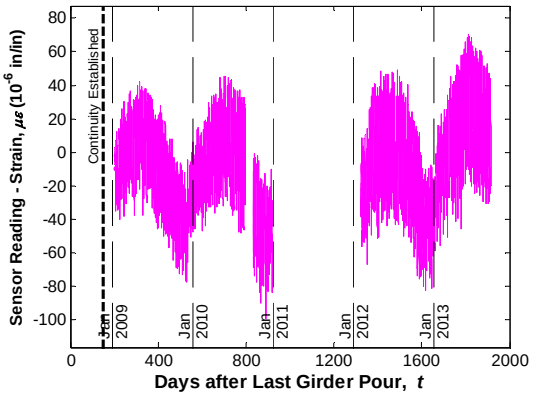

c) Sensor reading after temperature correction

Figure 78
Sensor No. 82, Location G3S24, Midspan Middle (VW)

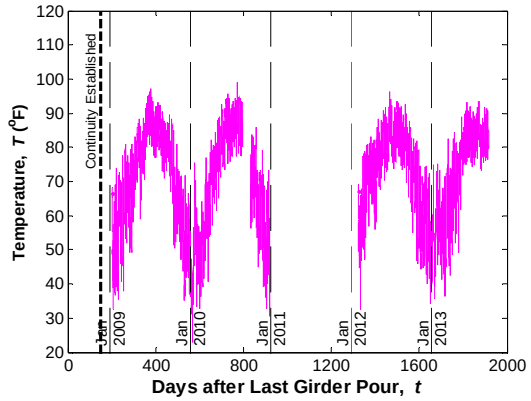

a) Temperature reading of the sensor

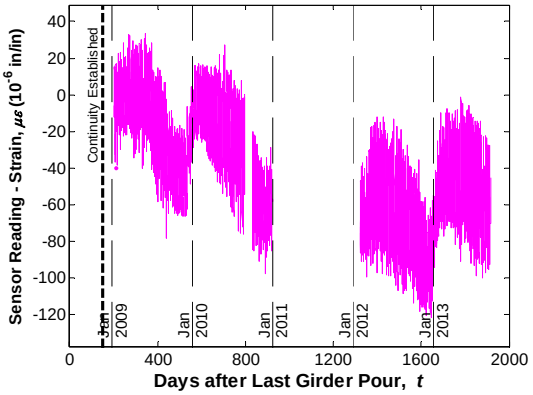

b) Sensor reading without temperature correction

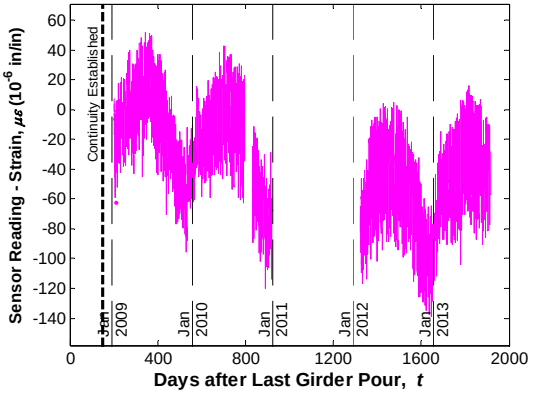

c) Sensor reading after temperature correction

Figure 79
Sensor No. 83, Location G3S24, Midspan Bottom (VW)

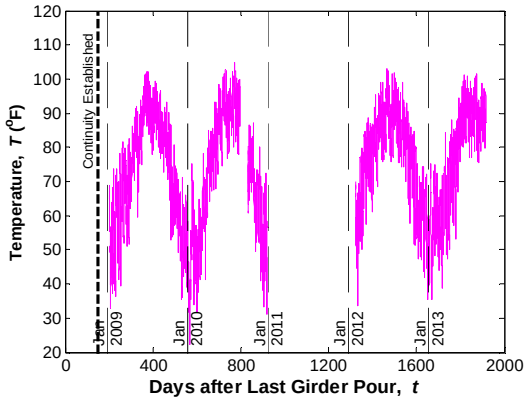

a) Temperature reading of the sensor

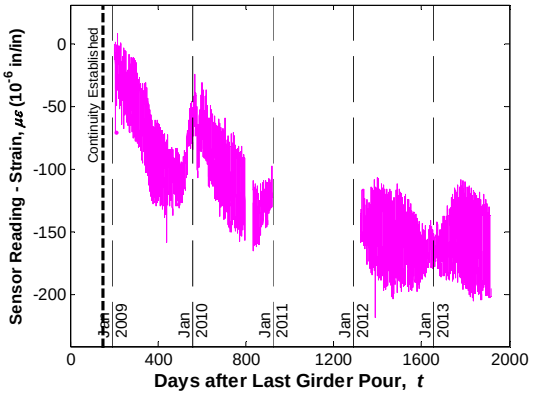

b) Sensor reading without temperature correction

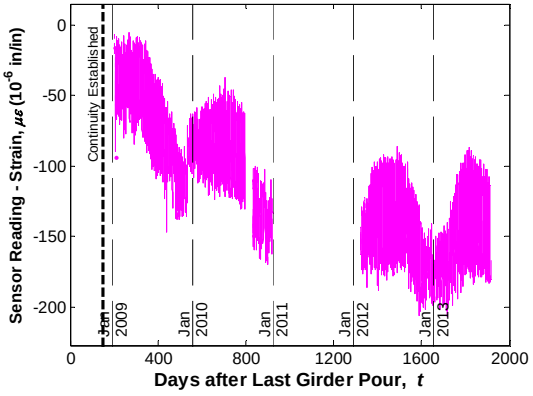

c) Sensor reading after temperature correction

Figure 80
Sensor No. 84, Location G4S24, Midspan Top (VW)

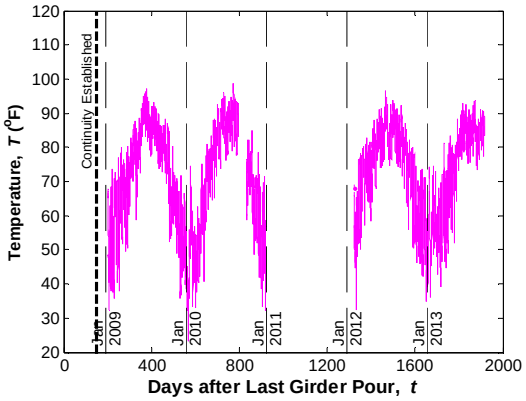

a) Temperature reading of the sensor

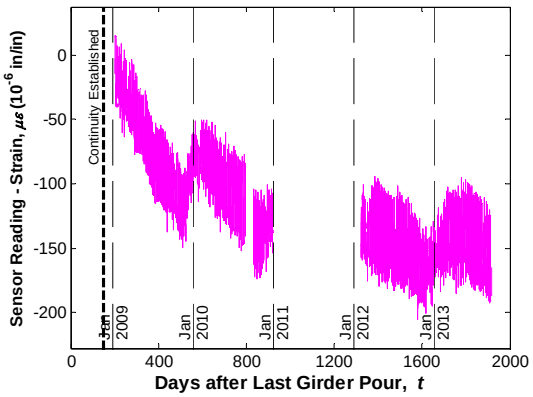

b) Sensor reading without temperature correction

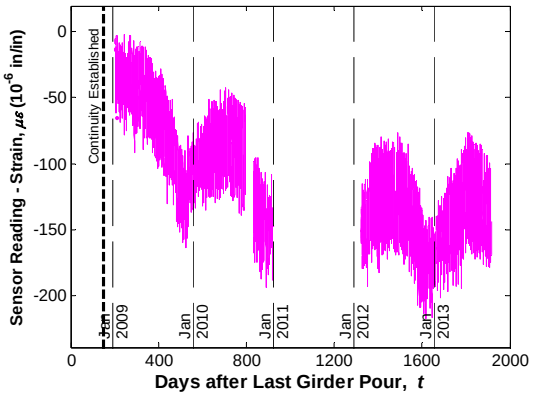

c) Sensor reading after temperature correction

Figure 81
Sensor No. 85, Location G4S24, Midspan Middle (VW)

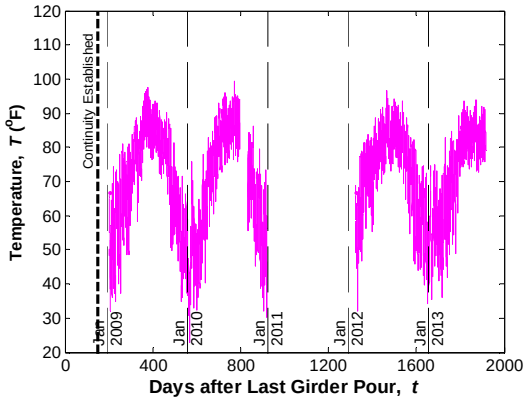

a) Temperature reading of the sensor

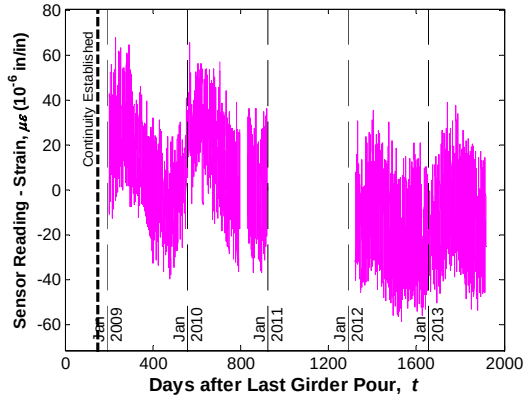

b) Sensor reading without temperature correction

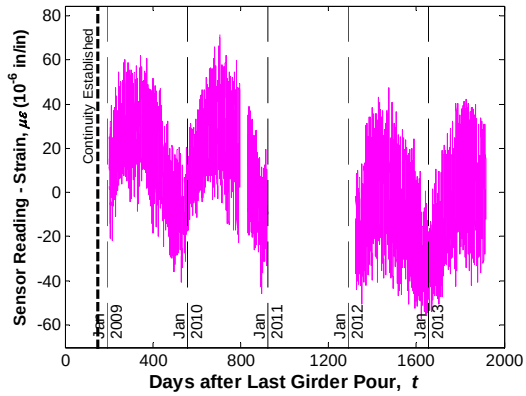

c) Sensor reading after temperature correction

Figure 82
Sensor No. 86, Location G4S24, Midspan Bottom (VW)

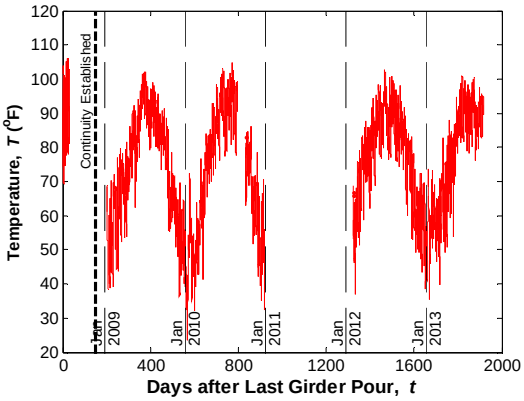

a) Temperature reading of the sensor

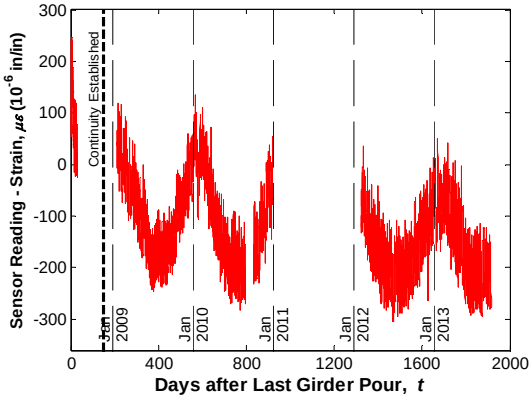

b) Sensor reading without temperature correction

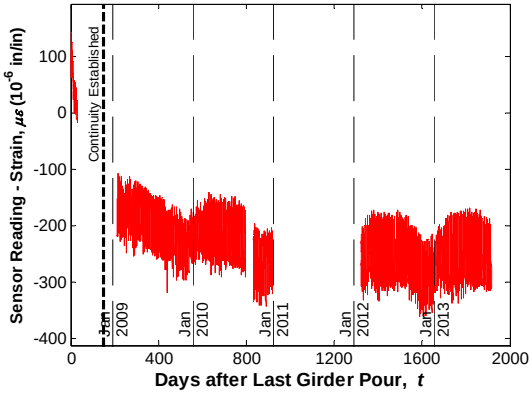

c) Sensor reading after temperature correction

Figure 83
Sensor No. 87, Location G3S24, Midspan Top (ES)

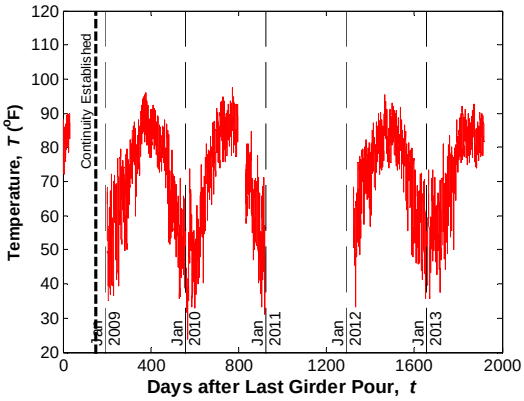

a) Temperature reading of the sensor

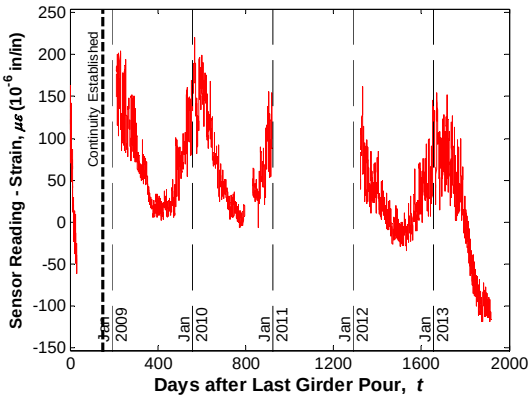

b) Sensor reading without temperature correction

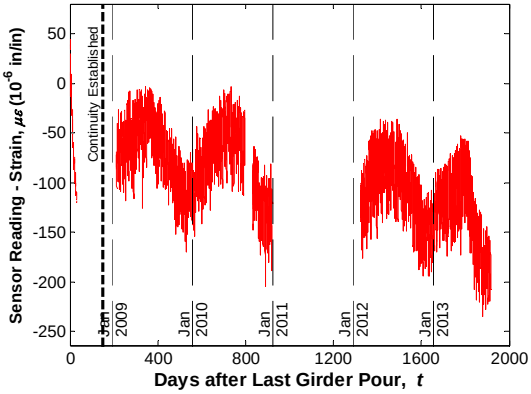

c) Sensor reading after temperature correction

Figure 84
Sensor No. 88, Location G3S24, Midspan Bottom (ES)

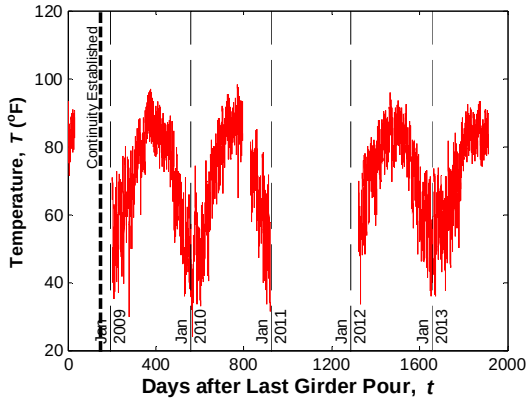

a) Temperature reading of the sensor

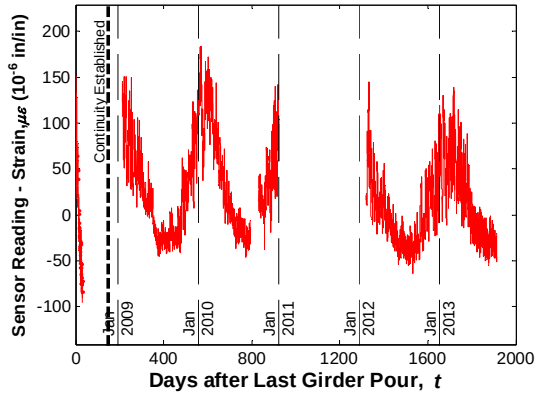

b) Sensor reading without temperature correction

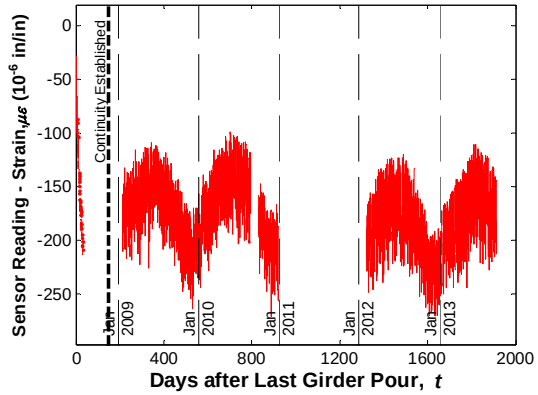

c) Sensor reading after temperature correction

Figure 85
Sensor No. 89, Location G4S24, Midspan
Bottom (ES)

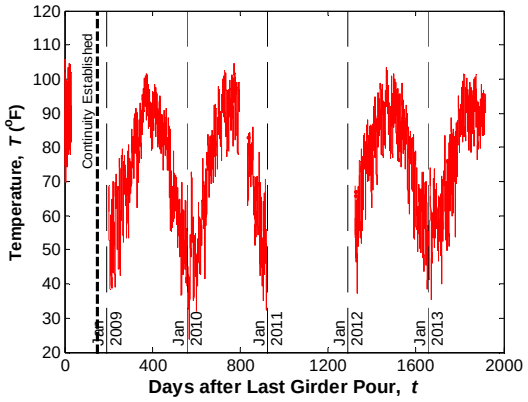

a) Temperature reading of the sensor

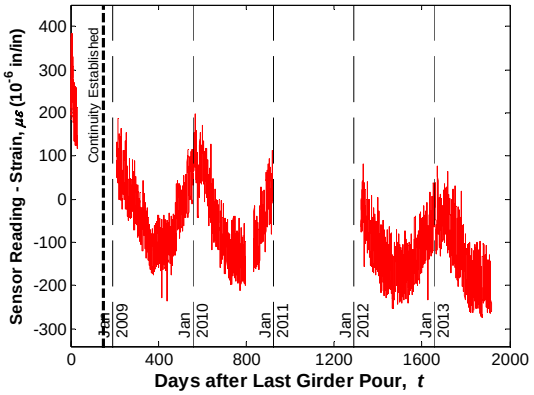

b) Sensor reading without temperature correction

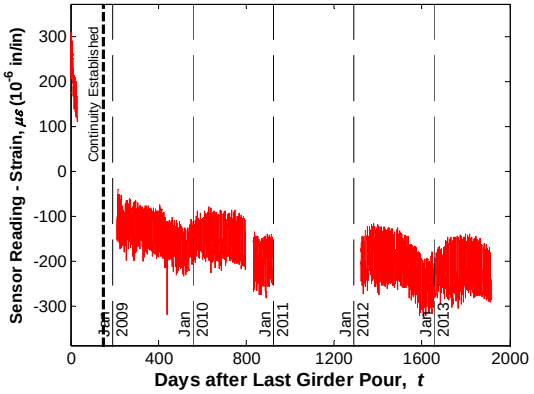

c) Sensor reading after temperature correction

Figure 86
Sensor No. 90, Location G4S24, Midspan
Top (ES)

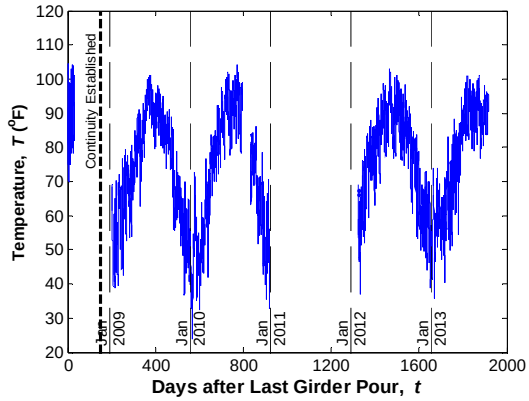

a) Temperature reading of the sensor

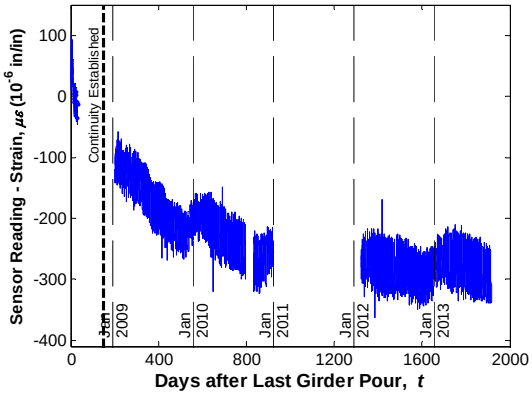

b) Sensor reading without temperature correction

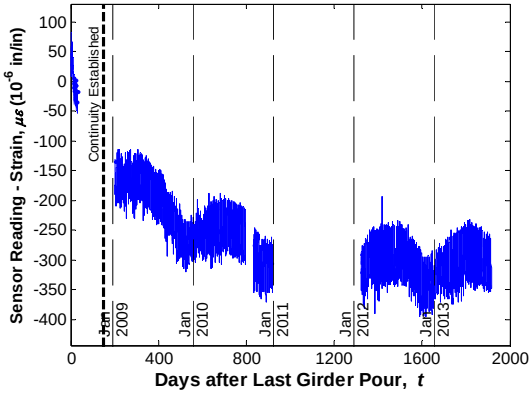

c) Sensor reading after temperature correction

Figure 87
Sensor No. 91, Location G4S24, Midspan Top (EC)

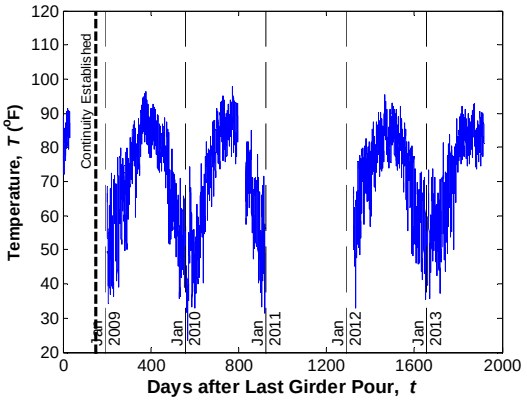

a) Temperature reading of the sensor

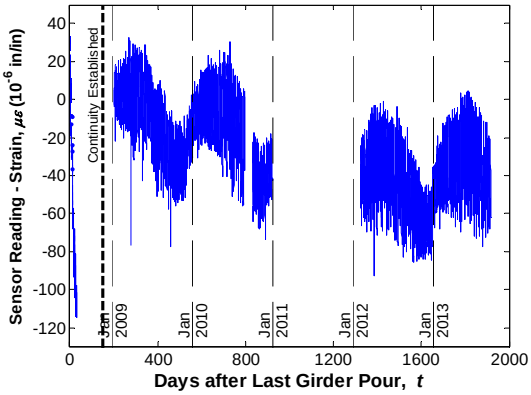

b) Sensor reading without temperature correction

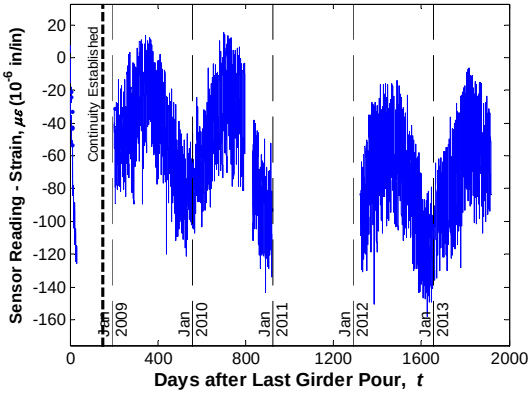

c) Sensor reading after temperature correction

Figure 88
Sensor No. 92, Location G4S24, Midspan Bottom (EC)

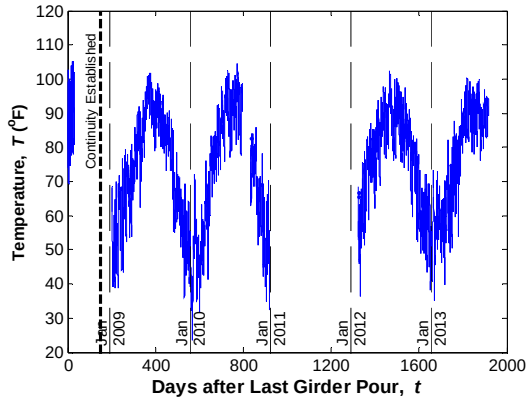

a) Temperature reading of the sensor

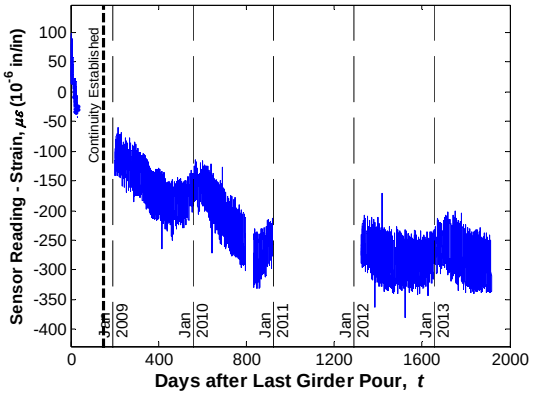

b) Sensor reading without temperature correction

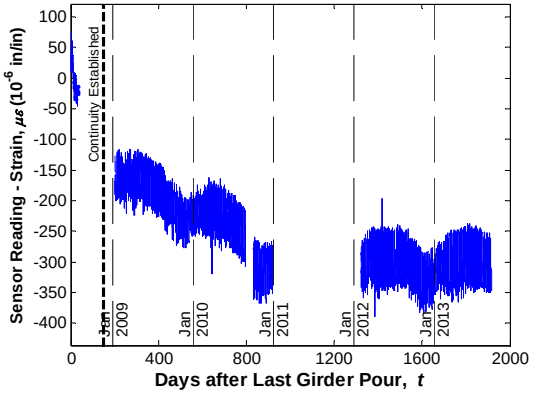

c) Sensor reading after temperature correction

Figure 89
Sensor No. 93, Location G3S24, Midspan Top (EC)

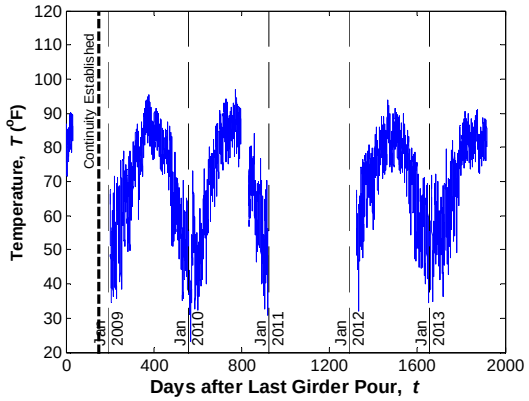

a) Temperature reading of the sensor

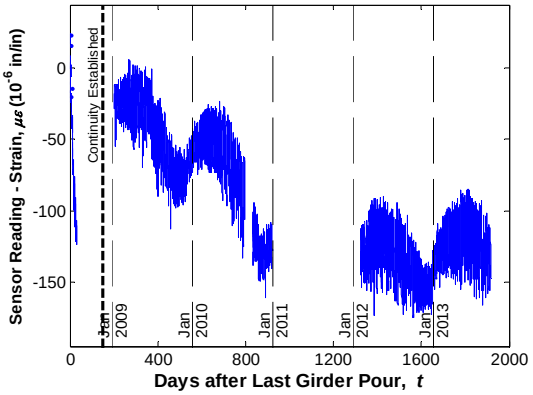

b) Sensor reading without temperature correction

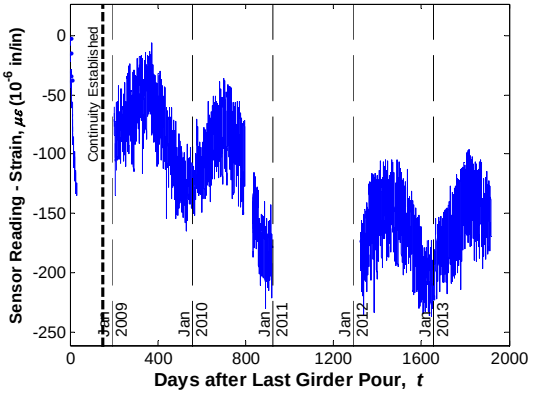

c) Sensor reading after temperature correction

Figure 90
Sensor No. 94, Location G3S24, Midspan Bottom (EC)

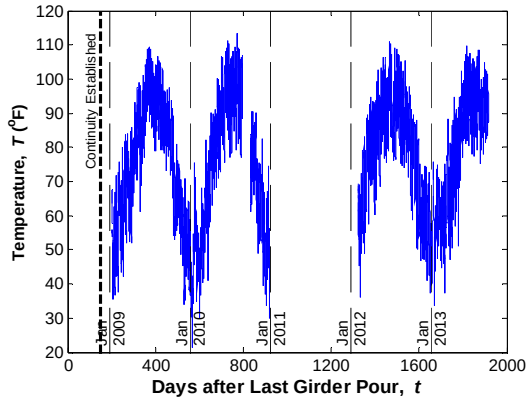

a) Temperature reading of the sensor

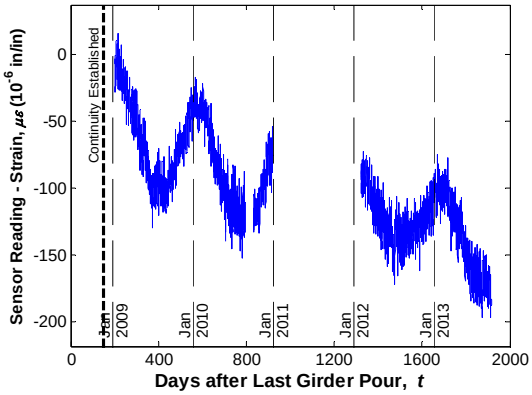

b) Sensor reading without temperature correction

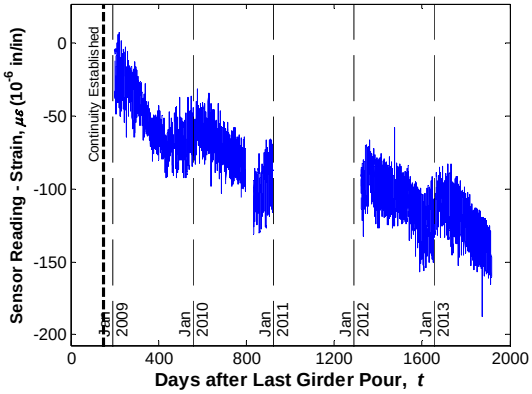

c) Sensor reading after temperature correction

Figure 91
Sensor No. 95, Location G3S24, Midspan Deck (EC)

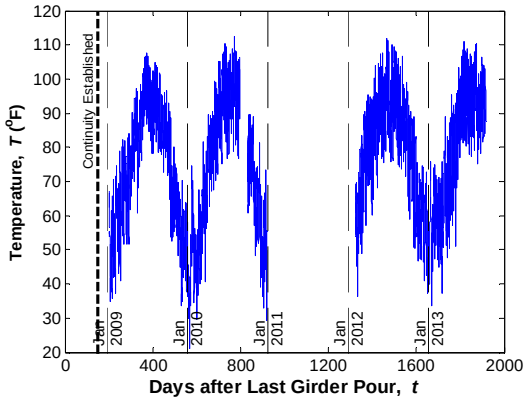

a) Temperature reading of the sensor

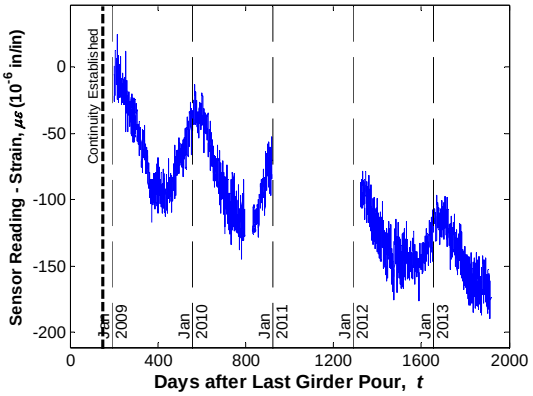

b) Sensor reading without temperature correction

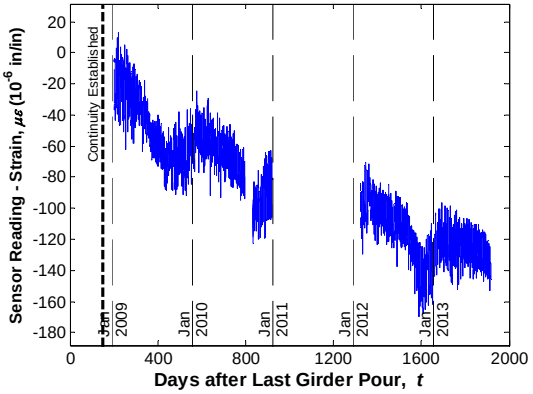

c) Sensor reading after temperature correction

Figure 92
Sensor No. 96, Location G4S24, Midspan Deck (EC)